Nonlinear modal analysis based on invariant manifolds - Application to rotating blade systems

Dongying Jiang

Dongying Jiang. Nonlinear modal analysis based on invariant manifolds - Application to rotating blade systems. Mechanics [physics.med-ph]. University of Michigan, 2004. English. NNT : . tel-00361013

NONLINEAR MODAL ANALYSIS BASED ON INVARIANT MANIFOLDS — APPLICATION TO ROTATING BLADE SYSTEMS

by

Dongying Jiang

A dissertation submitted in partial fulfillment
of the requirements for the degree of
Doctor of Philosophy
(Mechanical Engineering)
in The University of Michigan
2004

Doctoral Committee:

Professor Christophe Pierre, Co-Chair
Professor Steven W. Shaw, Co-Chair
Associate Professor Karl Grosh
Professor Armin Troesch

For Jiehua

ACKNOWLEDGEMENTS

I wish to express my sincere gratitude to my advisors and co-chairs of my doctoral committee, Professor Christophe Pierre and Professor Steven W. Shaw, for their generous support, expert guidance, and immense patience during the last five years. Without their support, this project could not have been completed. I also want to thank Professor Cesnik and Dr. Shin for providing me with the Finite Element Analysis code for the rotating blade model. I am also grateful to the other members of my doctoral committee, Professors Karl Grosh and Armin Troesch, for their valuable comments and suggestions. Finally, I want to thank Jiehua for her patience and motivational skills.

TABLE OF CONTENTS

CHAPTER

LIST OF FIGURES

LIST OF TABLES

Table

CHAPTER I

INTRODUCTION

1.1 Dissertation objectives

In the design-analysis cycle of complex structural systems such as rotorcraft, aircraft, and ground vehicles, it is necessary to understand their vibratory response thoroughly. If the vibration of interest is restricted to small neighborhoods of the static equilibrium positions, then the assumption of a linear system can be made. The corresponding analysis procedure is then greatly simplified, through the use of modern tools such as Finite Element Analysis and Modal Analysis. In contrast, when the amplitudes of oscillations are large, beyond the scale of linearization, or when a system behaves inherently nonlinearly with respect to its equilibrium configurations, then nonlinear equations of motion must be used in the model.

It is well known that nonlinear systems exhibit much richer and more complex behavior than their linear counterparts (i.e., bifurcations, internal resonances, sensitivity to initial conditions, etc.). Moreover, for a nonlinear system linear superposition is no longer valid, and the internal nonlinear coupling present between the linear normal modes of the system may necessitate the use of models with a relatively large number of degrees of freedom (DOF) in order to capture the system dynamics accurately. As a result, studies of nonlinear systems often sacrifice either time (through a large, expensive computer model) or accuracy (through the elimination of possibly significant mechanisms).

This research is aimed at the development and implementation of model reduction methods for certain classes of nonlinear structural systems, based on the invariant manifold approach initially developed by Shaw and Pierre [1–4], and further developed and implemented by Boivin [5, 6] and Pesheck [7]. The primary goal of this dissertation is to extend the nonlinear modal analysis methodology to large-scale structural systems (particularly those modeled with the finite element method) with various types of nonlinearities (e.g., polynomial and piecewise linear), including systems subject to external excitation and those with internal resonances. Another objective of this work is to apply the invariant manifold approach to an industrial structure with a complex, intrinsic nonlinearity. The nonlinear dynamics of an important class of engineering rotating structures are investigated, namely rotorcraft blades.

1.2 Background

In the area of nonlinear vibrations, much research work has been done for systems with a few DOFs, such as lumped-mass models [8–11], and models obtained via a Galerkin discretization of the governing partial differential equations (PDE) for continuous systems [12–15]. These low-order models are useful for understanding general behaviors. However, many of the methods developed are applicable only to relatively simple systems, and become unwieldy when used for systems with complex PDEs or large numbers of DOFs.

In order to obtain accurate reduced order models for nonlinear systems, “nonlinear modal analysis” has been proposed as an analogy to its linear counterpart. The concept of nonlinear normal modes (NNM) was first developed by Rosenberg [16] for conservative systems with symmetric nonlinearities. In his definition, NNMs are motions where (a) all masses have periodic (not necessarily harmonic) motions with the same period, (b) all masses pass through the static equilibrium positions at the same time, (c) and all masses achieve the maximum displacements at the same time. This is clearly an extension of the linear normal mode idea, but the relationships among all DOFs no longer need be simply linear. Since then, the existence [17, 18], stability [8, 10, 19–21], and construction [9, 22, 23] of NNMs have been topics of considerable investigation in this field. Detailed reviews were written by Vakakis *et al.* [24, 25], which summarize much of the research in this area to date. Here, we give a brief overview of the relevant literature, focusing on the methods of constructing NNMs, but the reader is referred to references [24, 25] for a complete bibliography.

For weakly nonlinear systems, perturbation methods can be used to determine the nonlinear normal mode shapes and associated natural frequencies. King and Vakakis [26] used an energy-based approach to compute NNMs for a class of one-dimensional, conservative, continuous systems. This approach has been extended to cases with internal resonances [27]. It has been shown that under some circumstances, NNMs cannot be constructed using physical coordinates and that a transformation to linear modal coordinates is necessary in order to define NNMs. Nayfeh and Nayfeh [28] constructed NNMs based on the method of multiple scales. They proposed a decomposition of the system state variables into complex quantities, hence simplifying the construction of NNMs [29].

Shaw and Pierre [1–4] introduced the definition of NNMs based on the concept of invariant manifolds. The invariant manifold is a hypersurface spanned by the linear modal coordinates in the phase space and is tangent to the corresponding linear mode at the equilibrium position. Here, the term “invariant” indicates that any motion initiated on the manifold will remain on it for all time. This new definition of NNMs is more general than the previous one, as it allows for a rigorous analysis of damped nonlinear systems, as well gyroscopic systems and those with non-symmetric nonlinearities. A framework for constructing NNMs was proposed by Boivin [5, 6] and Pesheck [7] for conservative systems and for non-conservative systems with linear proportional damping. According to the definition of invariant manifolds, a single pair of state variables in linear modal coordinates is chosen as *master* coordinates for an individual NNM, then all the remaining DOFs, the *slave* coordinates, are constrained to the *master* coordinates. Time-independent PDEs describing the geometry of the manifold are produced using this approach, but they are generally not solvable in closed form. Through a polynomial series expansion in the manifold coordinates, the constraint functions for the *slave* coordinates can be approximated numerically in a systematic fashion [7]. Once the NNM is obtained, motions on it are governed by the corresponding *master* coordinates and are described by two first-order ordinary differential equations, hence yielding a one-DOF reduced order model.

Unlike linear modes, the NNMs will interact during a general motion. Moreover, the invariant manifold approach based on a single mode expansion will break down in the presence of internal resonances between *master* and *slave* coordinates [7]. Hence, a multi-mode expansion methodology is required to study the true multi-mode motions of nonlinear systems. In the case of M modes involved in an internal resonance, the manifold is approximated with a polynomial series expansion in the $2M$ *master* coordinates. The results are determined in a somewhat complicated, but still systematic fashion [7]. As with the single mode case, this systematic approach enables the reduction of nonlinear systems with many DOFs to $2M$ first-order differential equations when motions in M modes are of interest.

Although the asymptotic series expansion approximation is a systematic and efficient approach to solve the PDEs that govern the manifold geometry, its application is limited to weakly nonlinear regions because (a) the polynomial expansion is only valid in a small amplitude range, (b) the domain in which the expansion is accurate cannot be determined *a priori*. A more general approach was developed by Pesheck *et al.* [7, 30], who applied a polar coordinate transformation to a single pair of state variables so that the constraint functions for *slave* coordinates are expressed in new *master* coordinates, namely amplitude a and phase ϕ. Fourier series were then used to expand functions in the ϕ coordinate, while orthogonal polynomials were used to expand functions in the a coordinate. Moreover, the amplitude domain was discretized into small segments, so that simple piecewise linear functions were utilized as expansion functions, with each such function corresponding to one segment. Using the Galerkin projection method [7, 30], invariant manifolds were constructed over strongly nonlinear regions in the a and ϕ coordinates, and motions on individual NNMs were reduced to two differential equations in the a and ϕ coordinates. This powerful method was applied successfully to a two-DOF lumped mass system with cubic nonlinear springs and to a 18-DOF rotating beam system with quadratic and cubic nonlinearities.

Finally, the concept of invariant manifolds has been used by others to derive the one-dimensional beam theories [31], to decouple the in-plane motions of a nonlinear isotropic plate from its transverse motions [32], and to obtain slow and fast invariant manifolds for a 2-DOF nonlinear oscillator [33]. Nayfeh *et al.* extended the complex invariant manifold approach [29] and utilized the method of multiple scales [34] to construct the NNMs of weakly nonlinear systems with internal resonances. Other authors have extended the formulation of Shaw and Pierre to construct the invariant manifold for nonlinear beam models [35, 36], to construct nonlinear normal modes for piecewise linear system [37], and to investigate the potential applications of the invariant manifold approach in the field of control [38, 39].

1.3 Dissertation outline

The remaining chapters of this dissertation are compiled from a collection of four manuscripts that have been or are destined to be published in refereed technical journals. Note that some repetition, in particular for background material, does occur. An outline of the subsequent chapters is as follows. In Chapter II, a numerical method for constructing nonlinear normal modes for piecewise linear autonomous systems is presented. These NNMs are obtained using a Galerkin-based solution of the invariant manifold's nonlinear partial differential equations. The accuracy of the constructed nonlinear modes is checked by comparing the motion on the invariant manifold to the exact solution, in both the time and frequency domains. It is found that this construction approach can accurately capture the NNMs over a wide range of amplitudes, including those with strong nonlinear effects. Several interesting dynamic characteristics of nonlinear modal motions are observed and compared to those of linear modes. A two-DOF example is used to illustrate the technique. The existence, stability and bifurcations of the NNMs for this example are investigated.

In Chapter III, a numerical method for constructing nonlinear normal modes for systems with internal resonances is presented, based on the invariant manifold approach. In order to parameterize the nonlinear normal modes, multiple pairs of system state variables involved in the internal resonance are kept as "seeds" for the construction of the multi-mode invariant manifold. All the remaining DOFs are constrained to these "seed" variables, resulting in a system of nonlinear partial differential equations governing the constraint relationships. The numerical solution procedure uses a combination of finite difference schemes and Galerkin-based expansion and projection methods. It is illustrated for two examples, both of which focus on the construction of two-mode models. The first example is based on the analysis of a simple three-DOF example system, and is used to demonstrate the approach. An invariant manifold that captures two nonlinear normal modes is constructed, resulting in a reduced order model that accurately captures the system dynamics. The methodology is then applied to a larger system, namely an 18-DOF rotating beam model that features a three-to-one internal resonance between the first two flapping modes. The accuracy of the nonlinear two-mode reduced order model is verified by time-domain simulations.

Chapter IV considers the use of numerically constructed invariant manifolds to determine the response of nonlinear vibratory systems that are subjected to periodic excitation. The approach is an extension of the nonlinear normal mode formulation previously developed for free oscillations, wherein an auxiliary system that models the excitation is used to augment the equations of motion. In this manner, the excitation is simply treated as an additional system state, yielding a system with an extra degree of freedom, whose response is known. A reduced order model for the forced system is then determined by the usual nonlinear normal mode procedure, and an efficient Galerkin-based solution method is used to numerically construct the attendant invariant manifolds. Each ‘forced’ manifold is essentially a modal manifold that varies periodically in time with a period equal to that of the excitation. The technique is illustrated by determining the frequency response for a simple two-DOF mass-spring system with cubic nonlinearities, and for a discretized beam model with 12 DOFs. The results show that this method provides very accurate responses over a range of frequencies near resonances.

Chapter V extends the invariant manifold approach to a model of an industrial structural system, namely a rotating active twist rotor (ATR) blade. The blade model is constructed using the finite element method with a two-field (Reissner-Hellinger type) mixed variational principle. The linearized blade model is first obtained with respect to the quasi-static equilibrium position. The nonlinear restoring force is then projected to the linear modal coordinates. Based on the invariant manifold approach, the nonlinear normal mode corresponding to the lowest bending linear mode (i.e., the first flapping mode) of the rotating blade is constructed numerically. A reduced-order model is obtained, which is shown to capture accurately the nonlinear dynamics on the invariant manifold. The nonlinear interactions of various physical blade motions, including lead-lag deflection, axial elongation, and torsion, with the first flapping bending motion of the blade are investigated by numerical simulations of time responses on the manifold.

Finally, in Chapter VI, conclusions are drawn and the contributions of this dissertation are summarized. Ideas for future work are also discussed.

CHAPTER II

LARGE-AMPLITUDE NONLINEAR NORMAL MODES OF PIECEWISE LINEAR SYSTEMS

2.1 Introduction

The concept of nonlinear normal modes was originated by Rosenberg [16, 40, 41], based on the analysis of discrete, symmetric systems with smooth nonlinearities. Since then, the existence [17, 18], stability [8, 10, 19–21], and construction [9, 22, 23, 38] of nonlinear normal modes have been among the topics of investigation in this field. More recently, an alternative definition for NNMs was introduced by Shaw and Pierre [1–3], based on invariant manifolds. With asymptotic expansions, the NNMs can be constructed symbolically [2, 3], but are accurate only in a neighborhood of the original equilibrium position. A more recent approach [42] extends the construction aspects of the invariant manifold approach to strongly nonlinear regions by using a Galerkin projection method to solve the invariant manifold equations. This makes the accurate construction of NNMs possible for a wide range of nonlinear dynamical systems.

Previous work on nonlinear normal modes dealt primarily with systems with smooth nonlinearities. However, many engineering systems involve components with contact, clearance, or different elastic materials. Such systems are often conveniently modeled by equations of motion with piecewise linear (PWL) terms. Due to their practical importance, the dynamic behavior of piecewise linear systems has been the subject of many investigations, which mainly focus on forced response under periodic excitation [43–45], including dynamic behaviors such as bifurcations and chaos [46–48].

The nonlinear modal behavior of PWL systems was first considered by Zuo and Curnier [49], based on autonomous, piecewise linear, multi-degree of freedom (DOF), gyroscopic and non-gyroscopic systems, which are the simplest models of cracked rotating shafts and cracked beams. However, the nonlinear modal motions were found by a direct approach and a more general construction method for NNMs was not pursued. Moreover, in reference [49] the switching hyperplane of the PWL systems considered passes through the origin, so that it is a special class of general PWL systems. Chen and Shaw [37] investigated a construction method of NNM for PWL systems based on asymptotic expansions. Since the switching hyperplane is not at the origin, the class of PWL systems in [37] is more general, but the asymptotic expansion can no longer be initiated at the static equilibrium position. The NNM is expanded in a series form in a neighborhood of an invariant disk, which makes it applicable near the switching hyperplane, but it is not valid at large amplitudes beyond the switching plane. Chati *et al.* [14] constructed the NNMs of a two-DOF PWL system using perturbation methods. The system they considered is a simplified model of the vibrations of a cantilever beam with a transverse edge crack. The NNMs obtained are only accurate for PWL systems with a small clearance spring located at the switching hyperplane, due to the approximations of perturbation methods. They also untilized the idea of *bilinear frequency* to compute the natural frequencies of nonlinear normal mode motions. The frequencies obtained with the bilinear formula are good approximations when the difference between the linear regions is small.

In this paper, we focus on a construction method of NNMs for the class of systems considered in reference [37]. The general dynamic behavior of the nonlinear modal motions is also discussed using the NNM results. Since asymptotic series expansions are not naturally suited for this type of nonlinearity, the Galerkin-based approach developed in reference [42] is extended to PWL systems and applied to a sample problem. The NNMs constructed in this manner are accurate over a large amplitude range. Also, no specific analysis is needed to account for the switching hyperplane, along which the system changes form, thereby making the approach much less cumbersome than the expansions used in reference [37]. Once the NNMs are constructed, the nonlinear modal dynamics for the individual NNMs can be determined.

The paper is organized as follows. The class of PWL systems studied is described in section 2.2. In section 2.3, the Galerkin-based approach for the construction of large-amplitude NNMs is briefly reviewed and adapted to PWL systems. A two-DOF example system is illustrated in section 2.4, which demonstrates the individual NNMs and their general dynamic behavior (including stability calculations). Finally, some conclusions are drawn.

2.2 Piecewise linear systems

Following the definition of Chen and Shaw [37], the dynamic system considered here is an unforced, undamped, autonomous N-DOF system of the form

$$\begin{cases} M\ddot{Z} + K_1 Z = 0 & \text{for } h^T Z \leq d \\ \\ M\ddot{Z} + K_2 Z = b & \text{for } h^T Z > d \end{cases} \tag{2.1}$$

where $d > 0$ is a real scalar constant, $Z,\ h,\ b\ \in\ \Re^N$, and $M,\ K_1,\ K_2$ are real symmetric positive definite $N \times N$ matrices. Obviously, this system has two distinct linear regions separated by a hyperplane, $\{Z \in \Re^N :\ h^T Z = d\}$. We denote the *first region* as $\{Z \in \Re^N :\ h^T Z < d\}$ and the *second region* as $\{Z \in \Re^N :\ h^T Z > d\}$. For small amplitudes, solutions remain in the first region and the response is simply linear and well understood. As the amplitude increases, the motions begin to pass through the switching hyperplane and enter the second region, in which case the response is nonlinear and no longer simple [46, 49].

System (2.1) represents a large variety of vibration systems with clearance or impact, which can be modeled by piecewise linear springs. However, there is only a single switching hyperplane in system (2.1). For PWL systems with more than one surface of discontinuity, the general behavior is much more complicated [50], and this is not considered here. Moreover, system (2.1) is conservative and non-gyroscopic.

In equation (2.1), linear modal analysis can be applied to the first region, $\{Z \in \Re^N : h^T Z < d\}$, containing the static equilibrium point. The eigenvector matrix, Q, can be found and normalized with respect to the mass matrix M. For simplicity, it is assumed that all the eigenfrequencies of the subsystem in the first region are distinct. After a linear modal transformation, $Z = Q\eta$, system (2.1) takes the standard form

$$\ddot{\eta} + \Lambda_1 \eta = f(\eta) \tag{2.2}$$

where $\eta \in \Re^N$ is the vector of modal coordinates, and the $N \times N$ diagonal matrix Λ_1 has entries that are the squares of the small-amplitude (first region) natural frequencies. The piecewise linear force vector, $f(\eta) \in \Re^N$, is given by

$$f(\eta) = H(h^T Q\eta - d)\left[(\Lambda_1 - Q^T K_2 Q)\eta + Q^T b\right] \tag{2.3}$$

where $H(\;.\;)$ is the heaviside function that stands for the switching hyperplane.

2.3 Nonlinear normal modes and the invariant manifold approach

Following the concept of invariant manifolds [1], a nonlinear normal mode is "*a family of motions which lies on a two-dimensional invariant manifold in the system phase space*".

Here, the term *invariant* indicates that any motion initiated on the manifold will remain on it for all time. In this formulation, a single pair of displacement-velocity coordinates is chosen as the *master* coordinates, which characterize the individual nonlinear modal motion that occurs on the manifold. The remaining DOFs are represented by *slave* coordinates, composed of displacement-velocity pairs for those DOFs, which are functionally dependent on the master coordinates. The dynamics of the master coordinates dictates the response of the slave coordinates through these relationships. The bulk of the work for determining NNMs lies in the determination of these constraint functions, which describe the geometry of the NNM invariant manifold in the system state space. In previous work, asymptotic series have been used to obtain approximate solutions of the manifolds, whereas here we employ a numerical solution that provides better accuracy over a much larger amplitude range.

In order to construct accurate nonlinear normal modes for this class of piecewise linear systems, the Galerkin-based approach [42] is utilized to solve for the invariant manifold. Considering system (2.2), for the k-th NNM the master coordinates are taken to be $(\eta_k,\ \dot{\eta}_k)$. These are transformed to amplitude and phase coordinates, $(a,\ \phi)$, as follows:

$$\begin{cases} \eta_k(t) = a(t)\ \cos\phi(t) \\ \\ \dot{\eta}_k(t) = -\omega_k a(t)\ \sin\phi(t) \end{cases} \tag{2.4}$$

where ω_k is the k-th natural frequency of the linear system in the first region. The master coordinates are defined as $(a,\ \phi)$, and have bounded domains for amplitude and phase, $a \in [0, a_{max}]$ and $\phi \in [0, 2\pi]$, respectively, which makes a Galerkin-based approach feasible [42]. On the invariant manifold, all of the slave coordinates are expressed as functions of the master coordinates as follows,

$$\begin{cases} \eta_i = P_i(a,\phi) \\ \\ \dot{\eta}_i = Q_i(a,\phi) \end{cases} \qquad i = 1, 2, ..., N, \;\; i \neq k. \tag{2.5}$$

These functions describe constraint relationships between the master and slave coordinates, thereby providing a functional form for the NNM invariant manifold. If the system is globally linear, $f(\eta)$ is zero in equation (2.2), and the constraint functions, P_i and Q_i, are also zero. For the piecewise linear system, the constraint functions are no longer zero when the master amplitude coordinate a is sufficiently large such that the system enters the second linear region. In other words, the constraint functions, P_i and Q_i, capture the geometry of the invariant manifold as the system passes between the first and second regions.

The invariant manifold equations are formulated as follows. A first-order, state-space formulation of the equations of motion (2.2) are used, into which equations (2.4) and (2.5) are substituted for the dynamic variables. The use of the chain rule on the constraint functions P_i and Q_i results in partial differential equations (PDE) which govern the P_i's and Q_i's. These are given by [42],

$$\begin{cases} Q_i = \frac{\partial P_i}{\partial a}\left(\frac{-f_k}{\omega_k}\right)\sin\phi + \frac{\partial P_i}{\partial \phi}\left(\omega_k - \frac{f_k \cos\phi}{a\omega_k}\right) \\ \\ -\omega_i^2 P_i + f_i = \frac{\partial Q_i}{\partial a}\left(\frac{-f_k}{\omega_k}\right)\sin\phi + \frac{\partial Q_i}{\partial \phi}\left(\omega_k - \frac{f_k \cos\phi}{a\omega_k}\right) \end{cases} \text{for } \; i = 1, 2, ..., N, \;\; i \neq k.$$

These are obviously valid when the force, $f \in \Re^N$, is smooth. However, one must be cautious when dealing with non-smooth nonlinearities, since these may result in constraint functions that are also non-smooth, in which case some of the terms in the PDEs, equation (2.3), may not exist. It is found that for piecewise linear systems, these governing

PDEs are also valid, since all the derivatives, $\partial P_i/\partial a$, $\partial P_i/\partial \phi$, $\partial Q_i/\partial a$, and $\partial Q_i/\partial \phi$, exist in each of the two regions. At the switching hyperplane, the geometry of the invariant manifold is continuous, since the force is continuous, but derivatives are not necessarily continuous. Therefore, global expansion functions for a Galerkin approach may not be well suited for the task, and a special discretization is used to construct the invariant manifold as described below.

In order to solve the PDEs, equation (2.3), a Galerkin projection is carried out over the chosen domain, $a \in [0, a_{max}]$ and $\phi \in [0, 2\pi]$. In the ϕ direction, the constraint equations P_i and Q_i are periodic, and thus Fourier series are the natural choice for the expansion. Furthermore, a half Fourier basis is sufficient for system (2.2), due to its conservative, non-gyroscopic nature [42]. Specifically, cosine functions are used for the position constraints P_i, and sine functions are used for the velocity constraints Q_i. Because of the nature of the manifold in the a direction, the domain $a \in [0, a_{max}]$ is divided into n equal segments, defined by

$$a \in [a_j,\ a_{j+1}], \qquad a_j = \frac{j\ a_{max}}{n}, \quad j = 0, 1, ..., n.$$

In each segment, piecewise linear functions are used as the expansion functions. Then, the unknown position and velocity constraint relations are expanded over each segment as follows,

$$\left\{ \begin{array}{l} P_i(a,\phi) = \sum_{l=1}^{2} \sum_{m=1}^{N_\phi} C_i^{l,m}\ T_{l,m}(a,\phi) \\ \\ Q_i(a,\phi) = \sum_{l=1}^{2} \sum_{m=1}^{N_\phi} D_i^{l,m}\ U_{l,m}(a,\phi) \end{array} \right. \qquad \text{for } \ i = 1, 2, ..., N, \ \ i \neq k \tag{2.6}$$

where the C's and D's are the unknown expansion coefficients, and $T_{l,m}$ and $U_{l,m}$ are tensor products of tent functions (defined below) in the a direction and trigonometric functions in ϕ. Hence, for a given segment,

$$T_{l,m} = A_l(a)\cos[(m-1)\phi], \qquad U_{l,m} = A_l(a)\sin(m\phi)$$

where

$$A_1(a) = \frac{a - a_j}{a_{j+1} - a_j}\ , \quad \text{and} \quad A_2(a) = \frac{a_{j+1} - a}{a_{j+1} - a_j}$$

are the tent functions employed in the segment $a \in [a_j, a_{j+1}]$.

The expansion functions given in equation (2.6) are substituted into the PDEs given in equation (2.3), and a Galerkin projection is carried out over the chosen segment, resulting in

$$\begin{aligned} 0 = \int_{a,\phi} T_{p,q} \Bigg[& -a \sum_{l,m} D_i^{l,m} U_{l,m} + \sum_{l,m} C_i^{l,m} \frac{\partial T_{l,m}}{\partial a} \frac{-f_k}{\omega_k} a \sin\phi + \\ & \sum_{l,m} C_i^{l,m} \frac{\partial T_{l,m}}{\partial \phi} (a\omega_k - \frac{f_k \cos\phi}{\omega_k}) \Bigg] \, da \, d\phi \end{aligned} \tag{2.7}$$

$$\begin{aligned} 0 = \int_{a,\phi} U_{p,q} \Bigg[& \omega_i^2 a \sum_{l,m} C_i^{l,m} T_{l,m} - a f_i + \sum_{l,m} D_i^{l,m} \frac{\partial U_{l,m}}{\partial a} \frac{-f_k}{\omega_k} a \sin\phi + \\ & \sum_{l,m} D_i^{l,m} \frac{\partial U_{l,m}}{\partial \phi} (a\omega_k - \frac{f_k \cos\phi}{\omega_k}) \Bigg] \, da \, d\phi \end{aligned} \tag{2.8}$$

for $i = 1...N,\ i \neq k,\ p = 1, 2$, and $q = 1...N_\phi$. This results in $2(N-1)2N_\phi$ nonlinear algebraic equations in the C's and D's. Note that such a system of equations must be solved for each a interval, resulting in a total of n such systems of equations that must be solved to obtain the entire manifold over the desired amplitude range.

In order to search numerically for these unknown coefficients, a local optimization algorithm (the Hybrid Powell method embedded in the commercial algorithm package *NAG*) is applied using an initial guess. Since the manifold geometry is continuous at the switching hyperplane, zero is a good initial guess for a segment crossing the switching plane. Results for subsequent amplitude intervals are obtained in a sequential manner, where the results for the C's and D's of a preceding segment are used as the initial values for the following segment. In this manner the procedure is self-starting and no complicated initial guessing algorithms are necessary. Note that each segment on which solutions are obtained is an annular strip in the state space. These strips are pieced together to form the invariant manifold. It is important to note that a system with N degrees of freedom will generally have N NNMs that are continuations of the modes of the linear system, and that each manifold is solved for individually. Bifurcations of the NNMs can lead to more NNMs than DOF [21], but these cases are not considered here.

The discretization in the a direction is analogous to the finite element method. In order to ensure boundary conforming conditions at the interface between neighboring segments, one ought to run the optimization algorithm once again after the local optimization results have been obtained for each of the individual segments. In other words, the results obtained from each segment are deemed as the initial guess for the optimization over the whole region. However, since the manifold geometry does not change rapidly, simple term-by-term averaging over the interface of contiguous segments has acceptable accuracy and is applied here.

Once the constraint functions (2.5) are obtained over the entire domain, the nonlinear modal dynamics on the invariant manifold can be reduced to a pair of first-order ordinary differential equations (ODEs) expressed in terms of the master coordinates a and ϕ [42], as follows:

$$\dot{a} = \frac{-f_k}{\omega_k}\sin\phi\,, \qquad \dot{\phi} = \omega_k - \frac{f_k}{a\omega_k}\cos\phi \tag{2.9}$$

where f_k depends on a and ϕ only, since the remaining dynamic states have been replaced by the constraint relations. Solutions of this relatively simple oscillator equation capture the dynamics of the full system restricted to the NNM manifold of interest. There will be

N such NNMs, each of which is obtained independently.

2.4 A two-DOF case study

An autonomous two-DOF piecewise linear system is studied here to illustrate the construction procedures described in sections 2 and 3. The system shown in Figure 2.1 is composed of two masses linked with linear springs, which is similar to the example system considered in references [37] and [14].

Let x_1 and x_2 represent the displacements of the first and second masses, m_1 and m_2, respectively, from their static equilibrium positions. The equations of motion are given by

$$\begin{cases} m_1\ddot{x}_1 + k_1x_1 - k_2(x_2 - x_1) = 0 \\ m_2\ddot{x}_2 + k_2(x_2 - x_1) = 0 \end{cases} \quad \text{if } \ x_2 < d_0$$

$$\begin{cases} m_1\ddot{x}_1 + k_1x_1 - k_2(x_2 - x_1) = 0 \\ m_2\ddot{x}_2 + k_2(x_2 - x_1) + k_3(x_2 - d_0) = 0 \end{cases} \quad \text{if } \ x_2 > d_0 \tag{2.10}$$

where k_1, k_2, and k_3 are the stiffnesses of the linear springs and d_0 is the distance from the static equilibrium position of m_2 to its contacting position with spring k_3. System (2.10) is obviously piecewise linear and of the form under consideration.

The system is nondimensionalized by introducing the following non-dimensional variables and parameters, $z_1 = x_1/d_0$, $z_2 = x_2/d_0$, $\tau = t/\sqrt{m_1/k_1}$, $\alpha = k_2/k_1$, $\beta = k_3/k_1$, and $\gamma = m_2/m_1$, yielding

$$\begin{bmatrix} 1 & 0 \\ 0 & \gamma \end{bmatrix} \begin{Bmatrix} \ddot{z}_1 \\ \ddot{z}_2 \end{Bmatrix} + \begin{bmatrix} 1+\alpha & -\alpha \\ -\alpha & \alpha \end{bmatrix} \begin{Bmatrix} z_1 \\ z_2 \end{Bmatrix} = \begin{Bmatrix} 0 \\ 0 \end{Bmatrix} \quad \text{if } \ z_2 < 1$$

$$\begin{bmatrix} 1 & 0 \\ 0 & \gamma \end{bmatrix} \begin{Bmatrix} \ddot{z}_1 \\ \ddot{z}_2 \end{Bmatrix} + \begin{bmatrix} 1+\alpha & -\alpha \\ -\alpha & \alpha+\beta \end{bmatrix} \begin{Bmatrix} z_1 \\ z_2 \end{Bmatrix} = \begin{Bmatrix} 0 \\ \beta \end{Bmatrix} \quad \text{if } \ z_2 > 1 \tag{2.11}$$

where the double derivative $\ddot{(\,)}$ now denotes $d^2(\,)/d\tau^2$.

Compared to the form of equation (2.1) in section 2, the mass matrix M, and the stiffness matrices K_1 and K_2 are

$$M = \begin{bmatrix} 1 & 0 \\ 0 & \gamma \end{bmatrix}, \quad K_1 = \begin{bmatrix} 1+\alpha & -\alpha \\ -\alpha & \alpha \end{bmatrix}, \quad K_2 = \begin{bmatrix} 1+\alpha & -\alpha \\ -\alpha & \alpha+\beta \end{bmatrix}$$

The displacement vector is $Z = [z_1 \;\; z_2]^T$, and the constant offset vector is $b = [0 \;\; \beta]^T$. The switching plane is defined by $\{Z : \; h^T Z = d\}$, where $h = [0 \;\; 1]^T$ and $d = 1$.

Linear modal analysis can be performed on the sub-system $M\ddot{Z} + K_1 Z = 0$ in equation (2.11), where $Z = 0$ is the static equilibrium position. For the generalized eigenvalue problem $K_1 q = \omega^2 M q$, the two real positive eigenvalues are found to be

$$\omega_{1,2}^2 = \frac{1}{2\gamma}\left[(\alpha + \alpha\gamma + \gamma) \mp \sqrt{(\alpha + \alpha\gamma + \gamma)^2 - 4\alpha\gamma}\,\right] \tag{2.12}$$

and the eigenvector matrix is given by $\tilde{Q} = [q_1 \;\; q_2]$, where q_1 and q_2 are the eigenvectors corresponding to the non-dimensional natural frequencies ω_1 and ω_2. After applying the modal transformation $Z = \tilde{Q}\eta$ and some manipulations, equation (2.11) is expressed in the standard form of equation (2.2), and is thus ready for the construction of its NNMs.

2.4.1 Case one

The non-dimensional stiffness ratios are taken to be $\alpha = \beta = 1.5$ and the mass ratio is $\gamma = 1.0$. The non-dimensional linear natural frequencies in equation (2.12) are $\omega_1 = 0.6472$ and $\omega_2 = 1.8924$, and the corresponding eigenvector matrix is given by

$$\tilde{Q} = \begin{bmatrix} 0.3419 & 0.6581 \\ 0.4743 & -0.4743 \end{bmatrix}$$

which has not been normalized with respect to the mass matrix.

The invariant manifold

The constraint equations that describe the two NNMs can be constructed following the procedure described in section 3. For the first NNM, η_1 and $\dot{\eta}_1$ are chosen as master coordinates, where $\eta_1 = a\ cos\phi$ and $\dot{\eta}_1 = -a\omega_1\ sin\phi$. The constraint equations $\eta_2 = P_2(a, \phi)$ and $\dot{\eta}_2 = Q_2(a, \phi)$ are numerically constructed over the domain $a \in [0, a_{max}]$, $\phi \in [0, 2\pi]$. In order to show the first NNM over a large amplitude region, the parameter a_{max} is set equal to 40.5, and the domain $[0, a_{max}]$ is divided into 81 equally sized segments. In order to ensure good numerical convergence, the number of harmonic terms is taken to be $N_\phi = 64$. For the second NNM, the master coordinates are $(\eta_2, \dot{\eta}_2)$, and the constraint equations are $\eta_1 = P_1(a, \phi)$ and $\dot{\eta}_1 = Q_1(a, \phi)$. The parameters set in the numerical solution algorithm are: $a_{max} = 60$, with 120 segments in the a direction, and $N_\phi = 32$.

The position constraints $P_2(a, \phi)$ and $P_1(a, \phi)$ for the two NNMs are shown in Figure 2.2. The geometry is flat and zero for small values of a, but is no longer planar after a crosses the switching hyperplane. For the first nonlinear mode, the switching plane is at $a \approx 2.11$, corresponding to a displacement of m_2 of $z_2 = 1.0$. As the maximum amplitude a_{max} is reached, the displacement z_2 is about 19. Hence, the Galerkin approach is applicable into amplitude regions of strong nonlinearity, where asymptotic analyses [37] are not applicable. For the second NNM, the switching amplitude is also at $a \approx 2.11$, and the maximum displacement z_2 is about 28 when a_{max} is reached.

It should be noted here that the switching position, $a \approx 2.11$, is represented by a circular line inside one of the strip segments used in the solution procedure. Therefore, the precise manifold geometry near the transition plane is not caught by this coarse discretization in a direction. However, it also shows that the Galerkin approach is robust, in the sense that it is not necessary to know the switching condition in advance. For the reader with an interest in further details about the manifold characteristics near this transition, two approaches can be taken. First, one could carry out an asymptotic analysis based on the Poincaré map at the transition plane, as done in reference [37]. Or, one can refine the manifold discretization near the switching hyperplane into smaller strip segments. The first approach is complicated, but theoretically interesting. On the other hand, a small mesh in the a direction is feasible and relatively simple to implement, and was carried out here. The refined region for the first NNM is shown in Figure 2.3, where the region $a \in [2.1082, 2.5]$ is evenly divided into 100 segments with $N_\phi = 64$. As described below, the Galerkin approach correctly captures the details of the switching plane with this refined mesh.

In order to better understand the nature of the invariant manifold, the manifold geometry is also shown in the original physical coordinate system $(z_i,\ \dot{z}_i)$. Figure 2.4 displays results based on the coarse segment discretization. The mesh shows the overall geometry of the manifold and the continuous solid curve depicts a representative motion on the manifold for a given initial value. Since the example system, equation (2.11), is conservative, all motions on the individual NNM manifolds must be periodic. Thus, the search for periodic solutions is essentially that of determining a set of initial conditions which ensure periodic response. These initial conditions, which characterize individual NNMs, can be found with numerical time integration and the search can be accelerated by the evaluation of the Jacobian matrix [49, 51]. This approach is an alternative method for determining NNM invariant manifolds for this class of problems.

It is interesting to note that the geometry of the first NNM shown in Figure 2.4(a) has a kink near the negative z_1 axis. This phenomenon can be explained by the time histories shown in Figure 2.5. As can be seen, in each period of the first NNM response shown, there exists a time interval over which the velocity $\dot{z}_1$ is nearly zero, the displacement z_1 is almost constant, the velocity $\dot{z}_2$ changes its sign, and the displacement z_2 changes quite rapidly. This behavior, which is reminiscent of sticking due to dry friction, leads to the kink in the manifold geometry.

Figure 2.5 displays a set of time responses on the individual NNM manifolds, obtained using two different approaches. The first category of responses is obtained from the time integration of the reduced equations of motion in the master coordinates a and ϕ, which describe the dynamics on the manifold, equation (2.9). Initial conditions $a(0) > 0$ and $\phi(0) = 0$ are used, and since the motion on the manifold is periodic, its amplitude is equal to $a(0)$. Then, the modal responses $\eta_i(t)$ and $\dot{\eta}_i(t)$ are obtained from $a(t)$ and $\phi(t)$ based on the master coordinate definition, equation (2.4), and the slave coordinate constraint functions, equation (2.5). Finally, the displacements $z_i(t)$ and velocities $\dot{z}_i(t)$ are reassembled via the linear modal transformation. The second category of responses consists of the periodic responses simulated from the equations of motion of the original system, equation (2.11). The initial conditions for periodic motions are obtained using a numerical direct search method. One can observe in Figure 2.5 that the simulations restricted to the Galerkin-based manifold match very closely those of the original system with the same energy level.

Another check of the Galerkin-based invariant manifold can be performed, and some insight into the NNM dynamics can be gained by considering the response in the frequency domain, as shown in Figure 2.6. The frequency f_0 of periodic motions on the manifold is defined as the fundamental frequency associated with the basic period τ_0, $f_0 = 2\pi/\tau_0$. In Figure 2.6, the frequency f_0 increases rapidly after the amplitude a crosses the transition hyperplane. Then f_0 tends to a limiting value as a increases. This limit is not equal to any linear modal frequency of sub-systems in equation (2.1), but is close to the *bilinear frequency* defined in reference [14] for PWL systems with zero gap, where the transition hyperplane is at the equilibrium position. In the present system, the gap becomes irrelevant at large amplitudes, and the results approach those of Chati and Rand [14]. In Figure 2.6, note the excellent agreement between response frequencies obtained from the simulation of the system dynamics and that of the dynamics restricted to the manifold.

The comparisons carried out in both the time and frequency domains clearly demonstrate that the Galerkin-based invariant manifolds accurately represent individual NNMs over a large range of amplitudes, and that the dynamics of the individual NNMs can be accurately reduced to a single DOF, given by equation (2.9).

Some interesting features of the dynamic behavior of the NNMs of the system can be observed by examining numerical responses for various initial energy levels in the phase plane and in the configuration space. Figure 2.7 depicts phase plane diagrams, closed curves correspond to periodic responses whose amplitude depends on the initial energy level. These loops are symmetric with respect to the displacement axis (due to the conservative nature of the system), but not with respect to the velocity axis (due to the asymmetry of the restoring force). In the configuration space, shown in Figure 2.8, the trajectories of solutions are represented by curves, but not by straight lines as in the linear case[1]. Moreover, the displacements z_1 and z_2 do not vanish simultaneously[2], but they reach their maximum and minimum positions at the same time. Also, note that when the amplitude is increased, a completely new modal curve is followed, which is not simply an extension of a curve from a lower amplitude. These deviations from linear system dynamics arise from the nonsymmetric, nonlinear nature of the example system considered here, and were also reported in reference [49].

---

[1] These are not tight loops, as can be shown from the symmetry of the manifold geometry, Figure 2.4, or the Poincaré section in Figures 2.11 and 2.12.

[2] This is apparent in Figure 2.8 for the second NNM, and is also true for the first NNM, upon close examination.

Stability of nonlinear normal modes

It is well known that nonlinear systems can exhibit a wide range of behaviors, including instabilities with bifurcations, chaos, etc. In order to investigate the bifurcation characteristics of the NNMs of the example system, the stability of the periodic motions on the NNM manifolds is examined as the amplitude a increases. Two methods, *characteristic multipliers* and *Poincaré map*, are employed to explore the stability of the NNMs and some additional features of the response.

The equation of motion of the two-DOF example system, equation (2.11), are expressed in standard state space form,

$$\dot{Y} = F(Y) \tag{2.13}$$

where $Y = [z_1 \ \dot{z}_1 \ z_2 \ \dot{z}_2]^T$ and the right hand side is given by

$$F(Y) = \begin{bmatrix} 0 & 0 & 1 & 0 \\ 0 & 0 & 0 & 1 \\ -(1+\alpha) & \alpha & 0 & 0 \\ \frac{\alpha}{\gamma} & -\frac{\alpha}{\gamma} - \frac{\beta}{\gamma} H(z_2 - 1) & 0 & 0 \end{bmatrix} Y + \begin{Bmatrix} 0 \\ 0 \\ 0 \\ \frac{\beta}{\gamma} \end{Bmatrix} H(z_2 - 1).$$

The characteristic multipliers can be determined from the *monodromy matrix* M, defined by $M(a) = \Phi(\tau_0)$, where τ_0 is the period of the motion, a is the amplitude of the periodic motion, and the matrix $\Phi(\tau_0)$ is determined from the matrix initial value problem,

$$\dot{\Phi}(\tau) = F_Y(Y_p)\Phi, \quad \Phi(0) = I \tag{2.14}$$

where Y_p is the periodic solution with amplitude a, and the period τ_0 is obtained while numerically searching for periodic solutions[3]. The matrix $F_Y(Y_p)$ is the Jacobian matrix of the right hand side of the state equation (2.13), which can be calculated at each time

---

[3] Note that the period τ_0 depends on the amplitude a.

step during a numerical integration. The stability of the periodic solution can be checked by the eigenvalues, $\mu(a)$, of the monodromy matrix $M(a)$. For a given periodic response of this conservative system, a necessary condition for stability is that all these eigenvalues lie on or inside the unit circle in the complex plane [51].

The monodromy matrix is typically used for systems with smooth restoring forces. In this example system, the force $F(Y)$ is piecewise smooth on either side of transition hyperplane. Since the solution intersects the surface of discontinuity without tangency and the initial time does not correspond to a crossing of the surface of discontinuity, the monodromy matrix can still be constructed from equation (2.14) [52]. For simplicity, an explicit forward Euler method is applied here to approximate the resulting matrix, so that it is not necessary to know the switching time in advance. The accuracy of the monodromy matrix is controlled by the time step in the numerical integration.

The movement of the eigenvalues of the monodromy matrix, $\mu(a)$, in the complex plane as the amplitude is varied is schematized in Figure 2.9 for both NNMs. The multipliers for both NNMs stay on the unit circle for small amplitudes. As a increases, a pair of complex conjugate multipliers move on the circle towards -1. At a critical value, $a = 6.52$ for the first mode, and $a = 4.04$ for the second mode, this pair merges at -1 and then one of those multipliers escapes the unit circle, yielding unstable behaviour. For the second mode, the motion on the manifold remains unstable above the critical amplitude. For the first mode, the pair of separated multipliers on the negative real axis merge again at -1 as the amplitude increases further, and stability is recovered for $a \geq 8.62$.

The results from the characteristic multipliers indicate that the system loses stability when the multipliers satisfy $\mu(a_c) = -1$, where a_c is the critical amplitude. This corresponds to a *flip bifurcation*, or a *subharmonic bifurcation* [51], or a *period doubling bifurcation*. This period doubling is illustrated in Figure 2.10 by computing the FFT of the response at two amplitudes close to, and on either side of, the bifurcation point. This *flip bifurcation* was also found in the piecewise linear system studied by Zuo and Curnier [49], where the instability was parameterized by a stiffness parameter, similar to the stiffness ratio β in equation (2.11).

In order to explore the dynamics in the unstable region, a Poincaré map is now employed [53]. Since there is only a single transition hyperplane in the system, it provides a natural Poincaré section [37], defined by the two components[4]

$$\Sigma = \{Y \in \Re^4 : \ z_2 = 1, \text{ and } \dot{z}_2 > 0\}$$

$$\Sigma^* = \{Y \in \Re^4 : \ z_2 = 1, \text{ and } \dot{z}_2 < 0\} \tag{2.15}$$

where Y is the vector of state variables in equation (2.13). The dynamics in both subregions are linear and analytical solutions can be locally obtained. Given the initial conditions of the exact solution for each nonlinear mode, the Poincaré mapping can thus be constructed numerically [37].

From a cross sectional view of the Poincaré map, the motion on the first NNM is stable until the critical amplitude, $a_c = 6.52$, is reached, and is represented by the pair of points in Figure 2.11(a). As the amplitude increases beyond the critical value, the motions become quasi-periodic, represented by the loops in Figure 2.11(b, c), and then chaotic, as shown in Figure 2.11(d). This sequence indicates that the period doubling at the critical point is subcritical. Also, the period doubling implies that the post-bifurcation responses will not exist in a NNM manifold, since period doubling cannot occur in a planar, autonomous system. Therefore, all post-critical responses associated with flip bifurcations must include both NNMs, as they are defined here. At the second critical amplitude, the periodic motion

---

[4] The Poincaré section should be defined such that periodic motions pierce it only once during one period. In the present case, either section Σ or section Σ^* is sufficient for this purpose, but solutions for both sections are shown to evidence the symmetry of the periodic responses.

regains stability, as shown in Figure 2.11(e). For the second mode, the periodic response remains unstable after the initial bifurcation at $a_c = 4.04$, as shown in Figure 2.12(b). Here the bifurcation appears to be supercritical, and another period doubling occurs, resulting in the transition from two to four points. At larger amplitudes the response becomes quasiperiodic, as shown in Figure 2.12(c).

2.4.2 Case two

Here the non-dimensional parameters in equation (2.11) are set as follows: stiffness ratios $\alpha = 1.5$ and $\beta = 3.0$, and mass ratio $\gamma = 1.0$. Compared to the first case, the stiffness of the clearance spring k_3 has been doubled. Therefore, the nonlinearity is larger than in the first case, and should result in more pronounced distortions of the NNM invariant manifolds. Since the linear modal parameters in equation (2.12) are independent of the parameter β, they are the same as in the first case.

The two NNM manifolds are constructed numerically following the same procedures as the first case: (1) For the first NNM, the maximum amplitude is $a_{max} = 15$, which is evenly divided into 30 segments, and $N_\phi = 64$ harmonic terms are used; (2) For the second NNM, the maximum amplitude is $a_{max} = 60$ with 120 segments, and $N_\phi = 32$ harmonic terms. The switching hyperplane is located at the amplitude $a \approx 2.11$ for both modes.

The NNM manifolds are shown in Figure 2.13 in the coordinate system $(z_i, \dot{z}_i)$. For the second NNM, the manifold looks similar to that for the first case. However, the kink in the first NNM is so pronounced in this case that the manifold is no longer single valued beyond a certain amplitude. This results from the stronger nonlinearity.

The time history of the motion on the first NNM is shown in Figure 2.14. Time integrations of the system equations of motion and of the dynamics restricted to the Galerkin-based manifold are compared. In all cases the periodic motions match very precisely. In the kink region of the manifold, the motion of mass m_1 has a slight oscillation superposed to the overall motion, instead of the near-stick phenomenon observed in the first case. This results in the multiple valued region, or loop, shown in the invariant manifold in Figure 2.13.

The accuracy of the NNMs is further verified in the frequency domain, as shown in Figure 2.15. The frequency-amplitude relationship is similar to that in the first case. Comparison of the Galerkin-based manifold simulation results and solutions from simulations of the system equations of motion demonstrate the excellent accuracy of the numerically computed NNMs.

The stability and large amplitude dynamics of these NNMs were also checked using characteristic multipliers and Poincaré maps. Similar results for the NNM bifurcations are found, as follows: (1) For the first NNM, the manifold is stable until a critical amplitude a_c=3.82, where a pair of complex conjugate characteristic multipliers merge at -1; solutions on the manifold remain unstable as the amplitude increases up to another critical amplitude, $a_c = 5.62$, where the multipliers merge again at -1, and solutions on the manifold regain stability. (2) For the second NNM, solutions on the manifold are unstable above the critical amplitude of $a_c = 2.30$. Sample Poincaré sections are shown in Figure 2.16 to illustrate the bifurcation of the first NNM.

2.5 Conclusions

From this study of NNMs for piecewise linear autonomous systems, and the example system studied in detail, the following conclusions are drawn. (i) The Galerkin-based method, originally developed for dynamic systems with smooth nonlinearities, can be extended to piecewise linear systems and used to accurately construct NNM invariant manifolds. The transformation of the master coordinates to polar form and the discretization in the amplitude make the Galerkin-based approach applicable in strongly nonlinear regions, as well as in the transition region between linear and nonlinear motions. (ii) The dynamic response on individual NNM manifolds can be reduced to a single-DOF system described in terms of the master coordinates. The dynamic response of all slave coordinates can be recovered from the simulation results of the master coordinates using the constraint relations. (iii) Although numerical results were obtained for a two-DOF system, the Galerkin-based approach can be easily applied to multi-DOF piecewise linear systems, so long as the single switching hyperplane condition is satisfied. (iv) For response amplitudes beyond the transition hyperplane, the dynamic behavior of piecewise linear systems can be quite complicated. This includes nontrivial aspects of the periodic response, such as loops in the manifolds, as well as instabilities leading to a variety of system responses. (v) The stability and post-critical dynamics of the nonlinear normal modes were investigated using characteristic multipliers and Poincaré maps. Flip bifurcations were found to occur for both modes, as well as transitions to quasiperiodic responses. For the first nonlinear mode, the NNM motions regained stability beyond a second bifurcation amplitude.

2.6 Figures

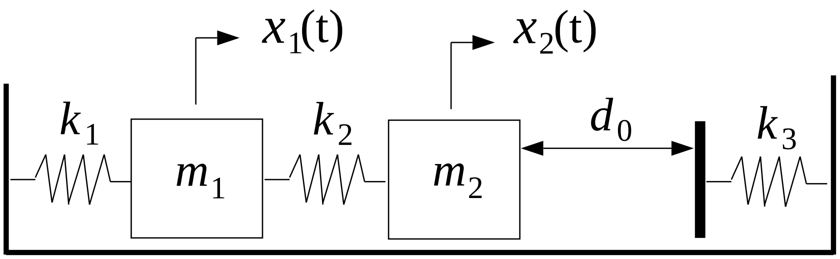

Figure 2.1: A two-degree of freedom piecewise linear system.

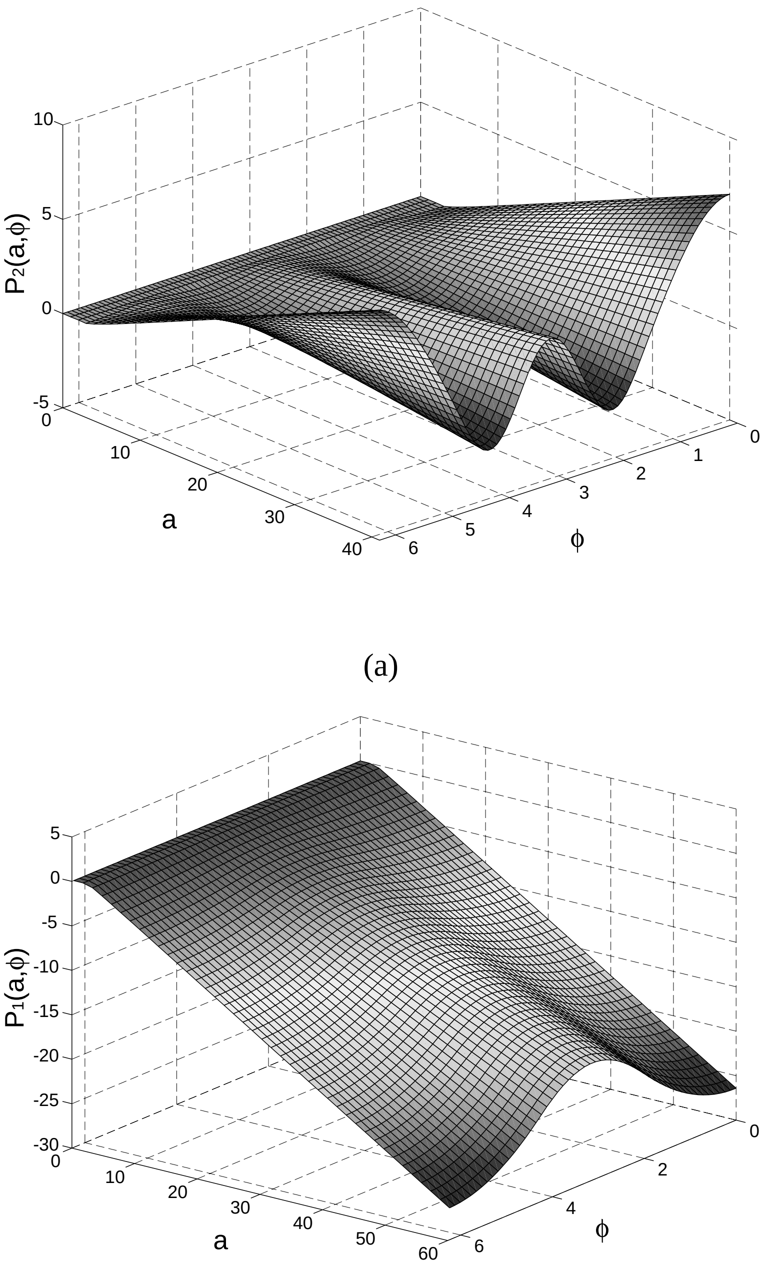

(a)

(b)

Figure 2.2: The i-th nonlinear mode invariant manifold for the position constraint, $\eta_i = P_i(a, \phi)$: (a) first mode (b) second mode, as a function of the amplitude a and phase ϕ.

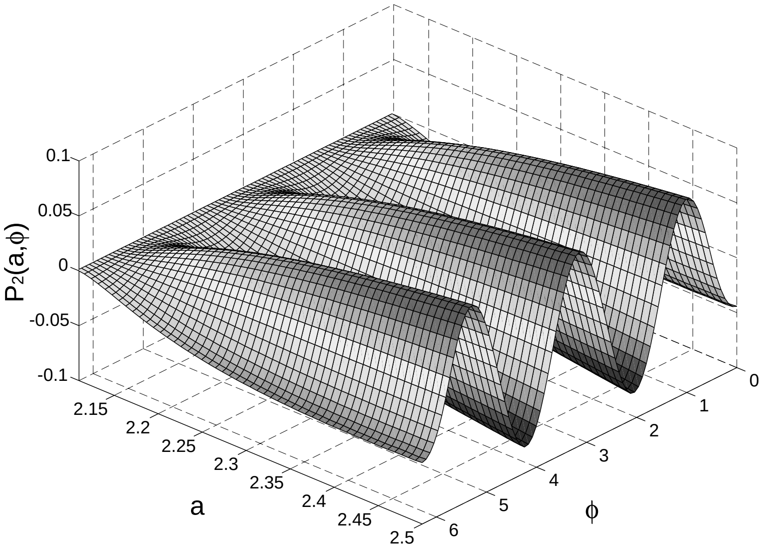

Figure 2.3: The refined first nonlinear mode invariant manifold for the position constraint, $\eta_2 = P_2(a, \phi)$, as a function of the amplitude a and phase ϕ.

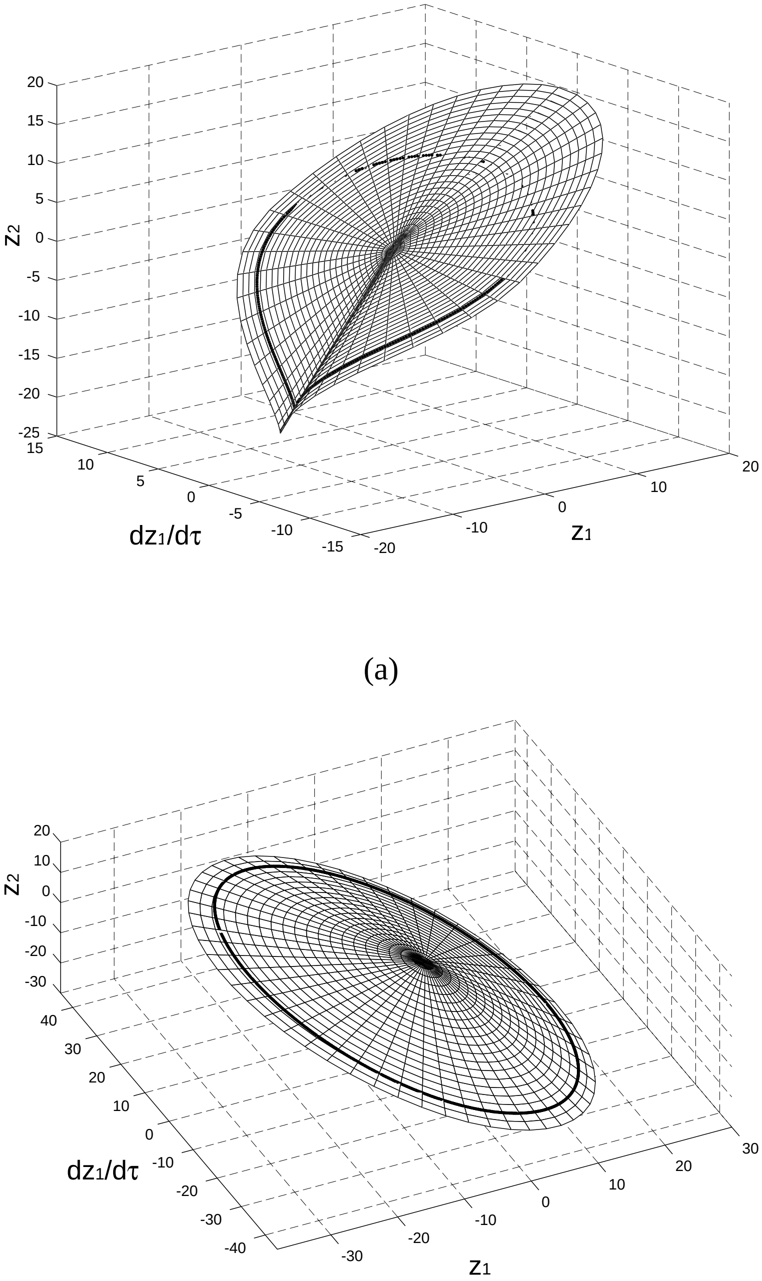

(a)

(b)

Figure 2.4: The nonlinear mode invariant manifold for the position constraint, $z_2(z_1, \dot{z}_1)$: (a) first mode (b) second mode, as a function of the non-dimensional displacement and velocity $(z_1,\ \dot{z}_1)$. A representative motion on the manifold is shown (——).

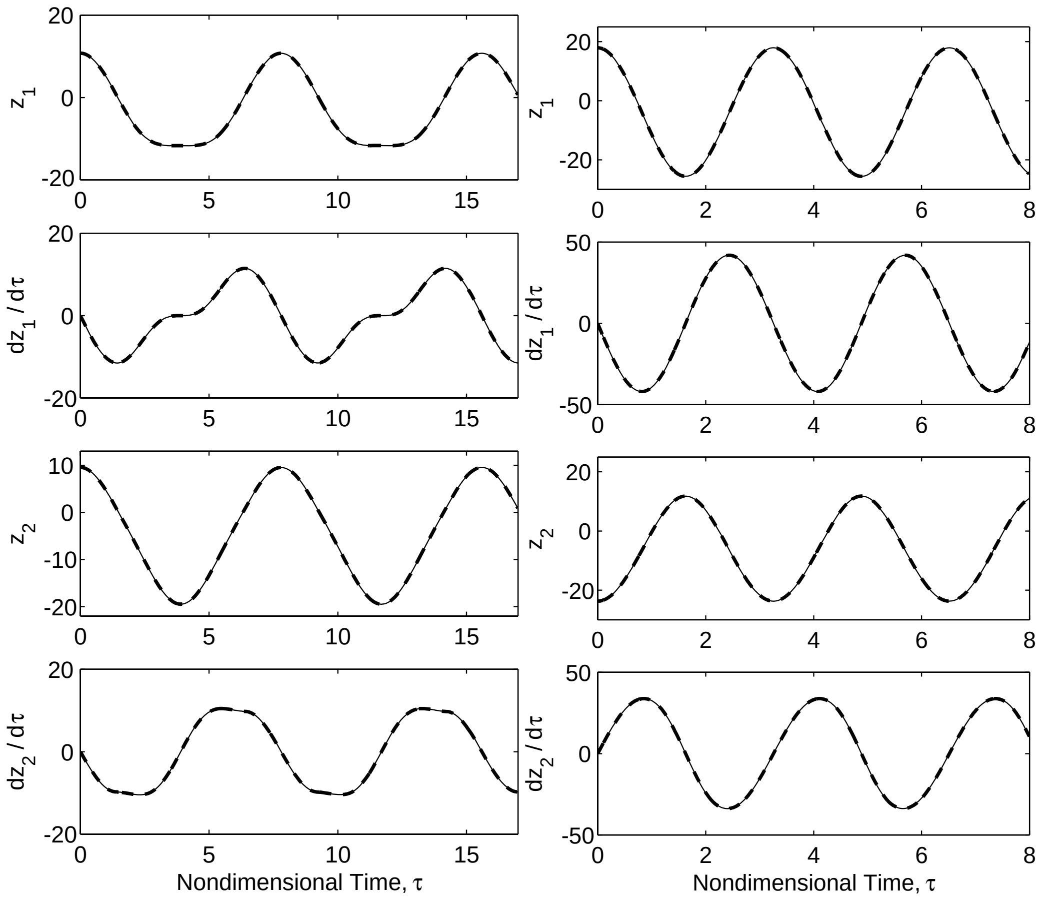

(a) (b)

Figure 2.5: Time histories of the motion on the invariant manifold: ——, solution from direct integration of the system equations of motion; - - -, time simulation of the dynamics restricted to the Galerkin-based manifold. (a) First NNM, amplitude $a = 24$; (b) Second NNM, amplitude $a = 35$.

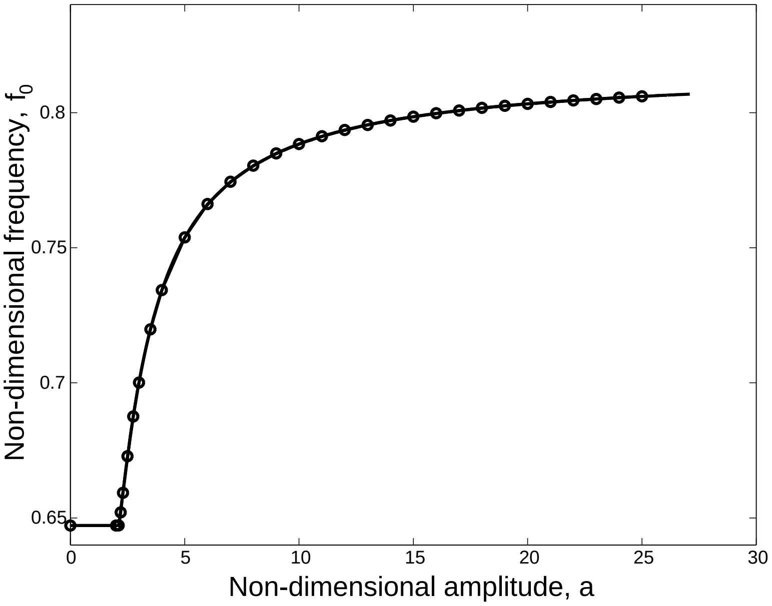

(a)

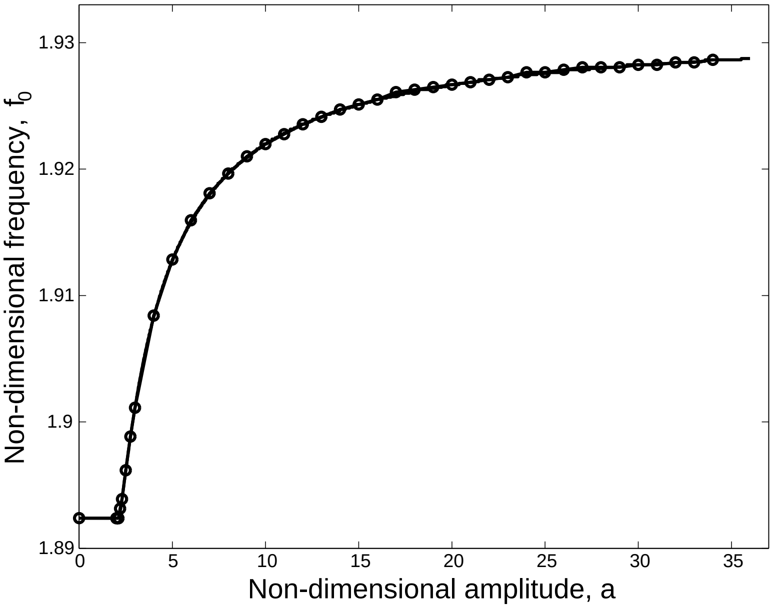

(b)

Figure 2.6: Response frequency for the nonlinear normal mode: ——, solution from direct integration of the system equations of motion; ‘ o ’ , time simulation of the dynamics restricted to the Galerkin-based manifold. (a) first mode; (b) second mode.

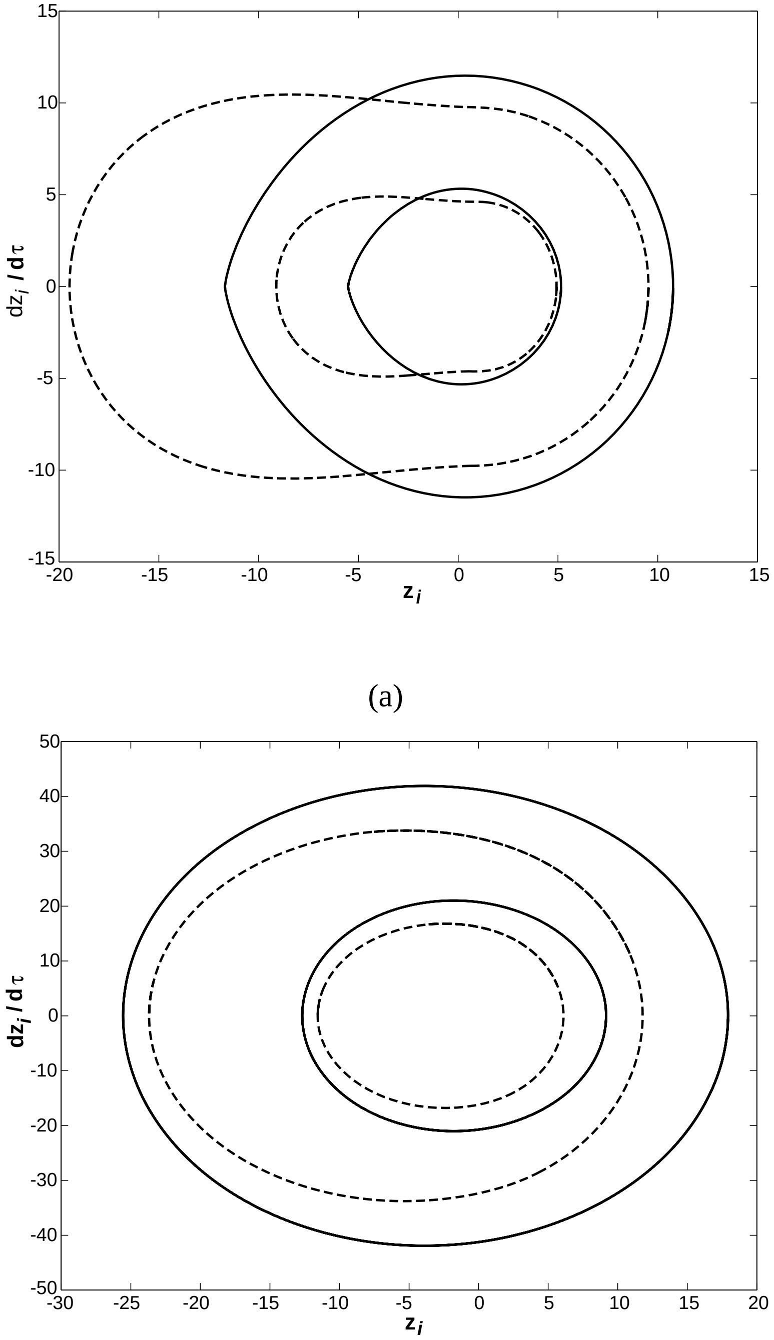

(a)

(b)

Figure 2.7: Phase portraits of the periodic motion on the invariant manifold: ——, mass one; - - -, mass two. (a) first mode, amplitude $a = 12,\ 24$; (b) second mode, amplitude $a = 17.5,\ 35$.

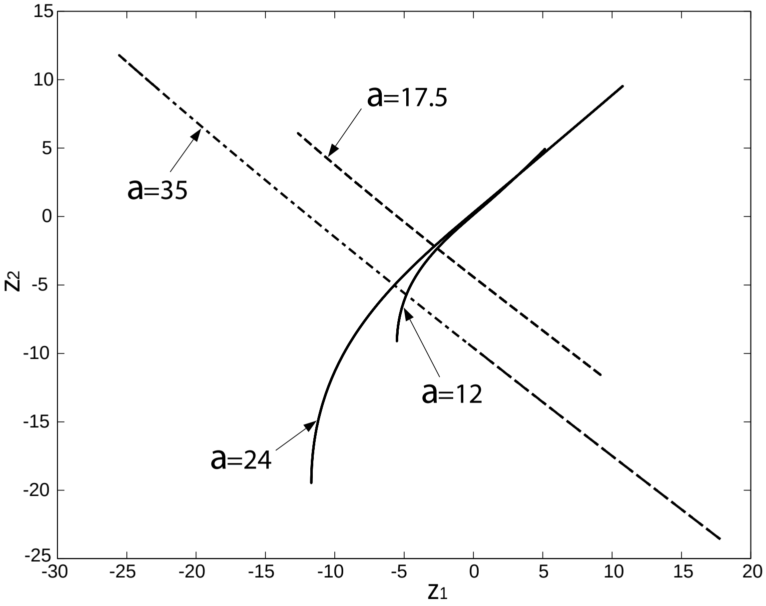

Figure 2.8: Periodic trajectories in the (z_1, z_2) configuration space: ——, first NNM, amplitude $a = 12,\ 24$; - - -, second NNM, amplitude $a = 17.5,\ 35$.

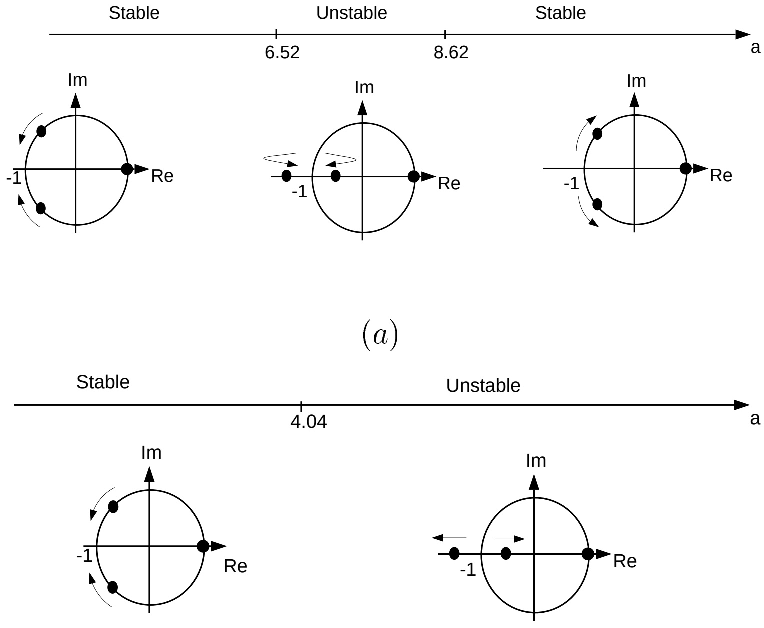

(a)

(b)

Figure 2.9: Eigenvalues of the monodromy matrix in the complex plane as the NNM amplitude a is increased: (a) first mode; (b) second mode.

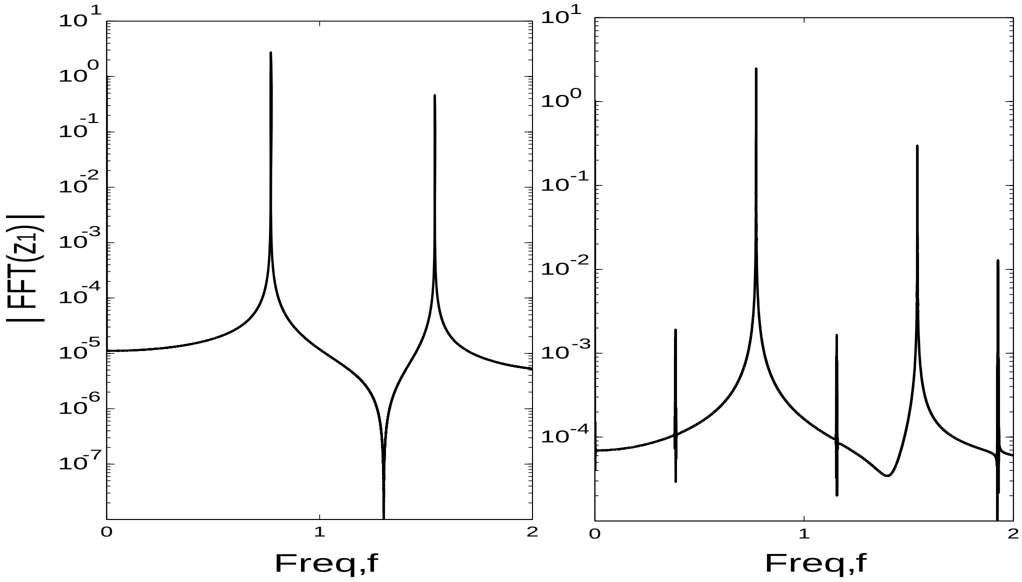

(a) (b)

Figure 2.10: FFT of the time response z_1 on the first NNM: (a) amplitude $a = 6.52$; (b) $a = 6.53$.

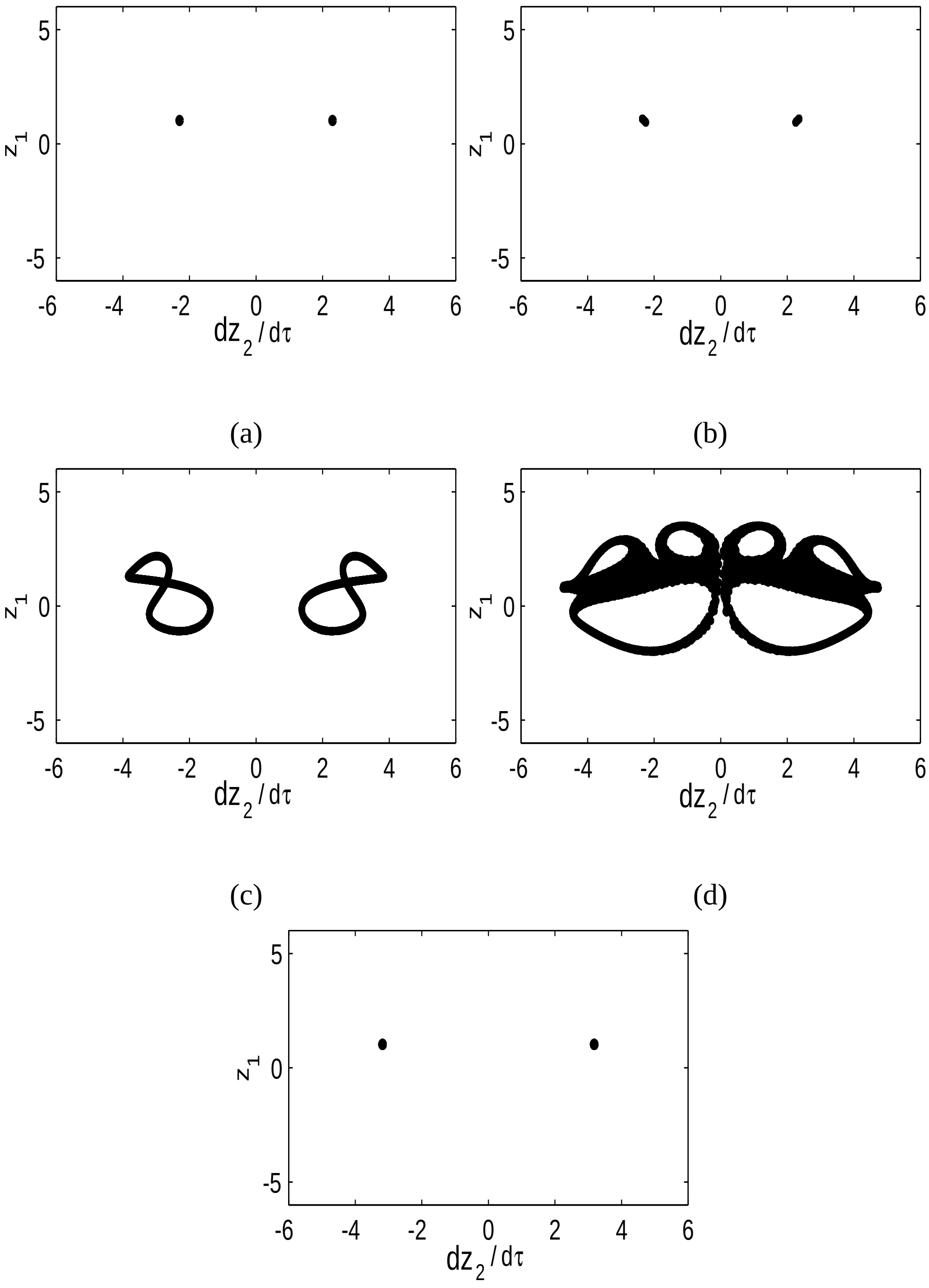

(a) (b)

(c) (d)

(e)

Figure 2.11: Poincaré section of the motion initiated on the first NNM versus amplitude a: (a) $a = 6.52$; (b) $a = 6.53$; (c) $a = 7.5$; (d) $a = 8.61$; (e) $a = 8.62$.

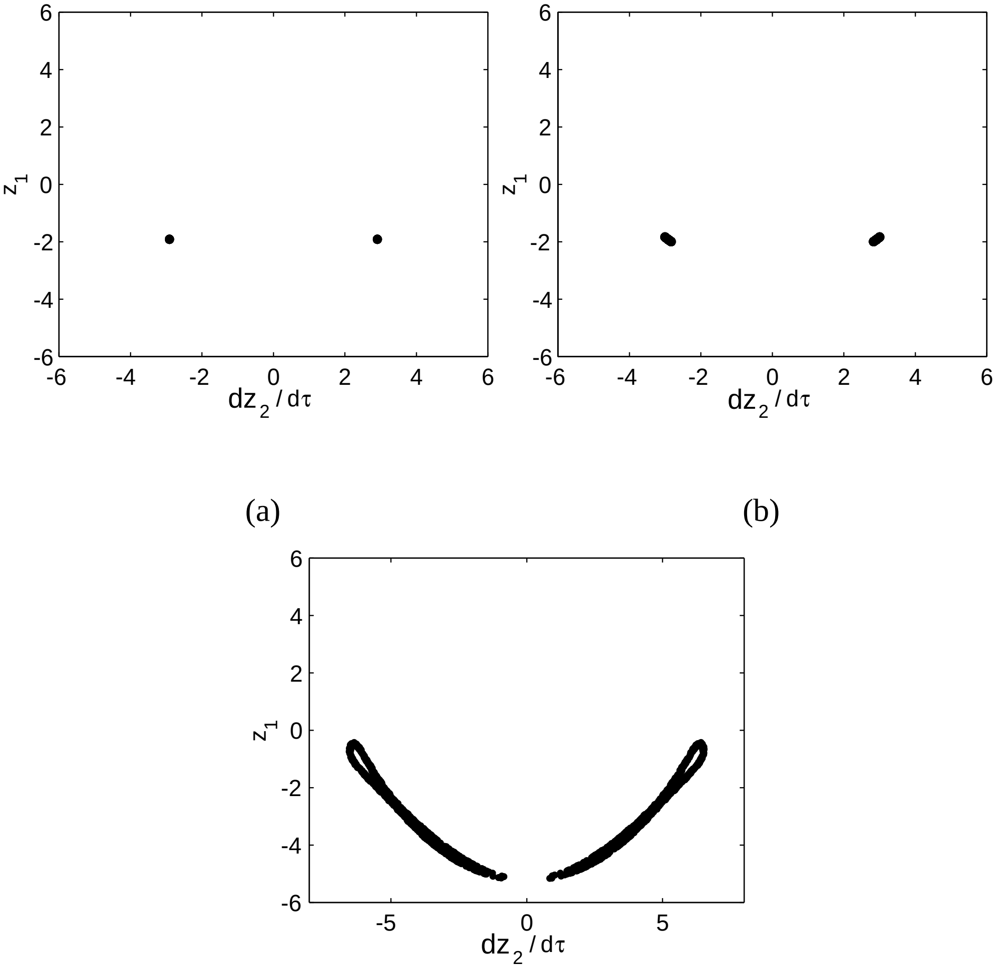

(a) (b)

(c)

Figure 2.12: Poincaré section of the motion initiated on the second NNM versus amplitude a: (a) $a = 4.04$; (b) $a = 4.05$; (c) $a = 6.0$.

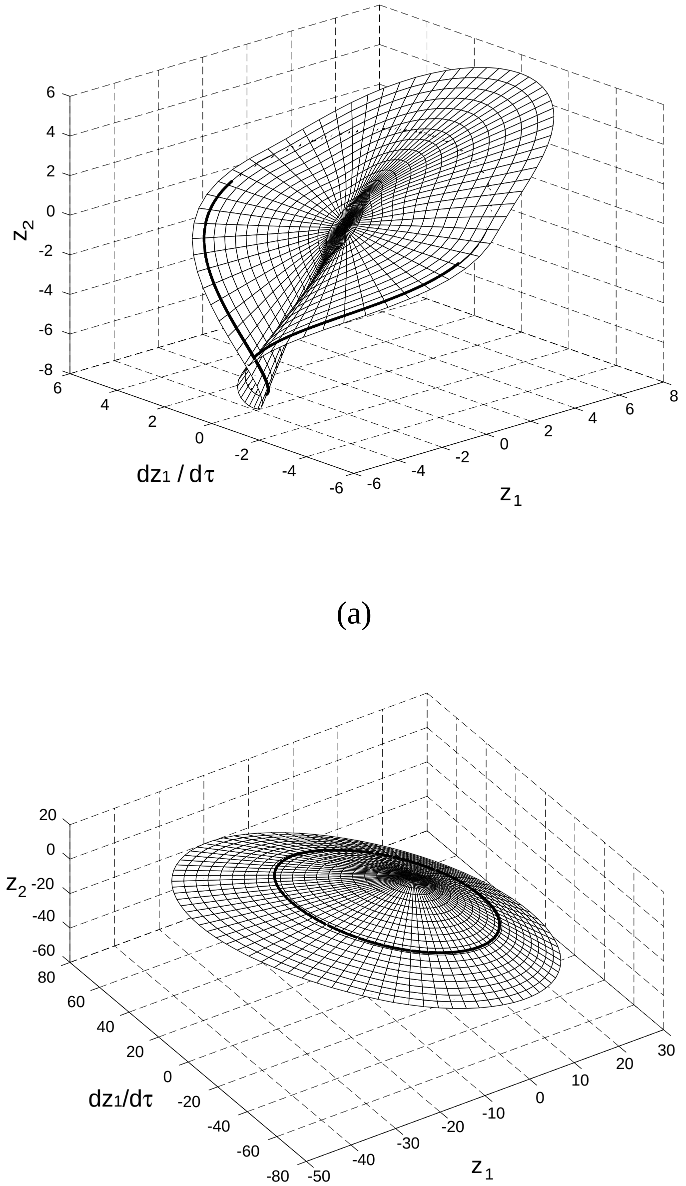

(a)

(b)

Figure 2.13: The NNM invariant manifold for the position constraint, $z_2(z_1, \dot{z}_1)$: (a) first mode (b) second mode, as a function of the non-dimensional displacement and velocity ($z_1,\ \dot{z}_1$). A representative motion on the manifold is shown (——).

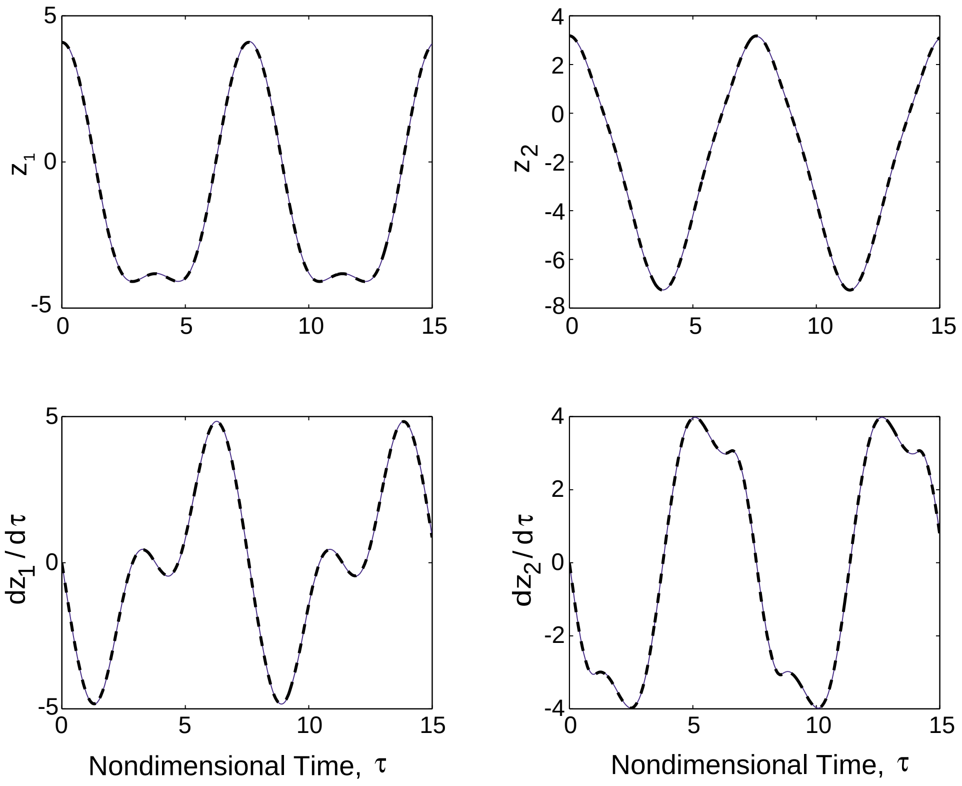

Figure 2.14: Time histories of the motion on the first NNM invariant manifold at amplitude $a = 8.5$: ——, solution from direct integration of the system equations of motion; - - -, time simulation of the dynamics restricted to the Galerkin-based manifold.

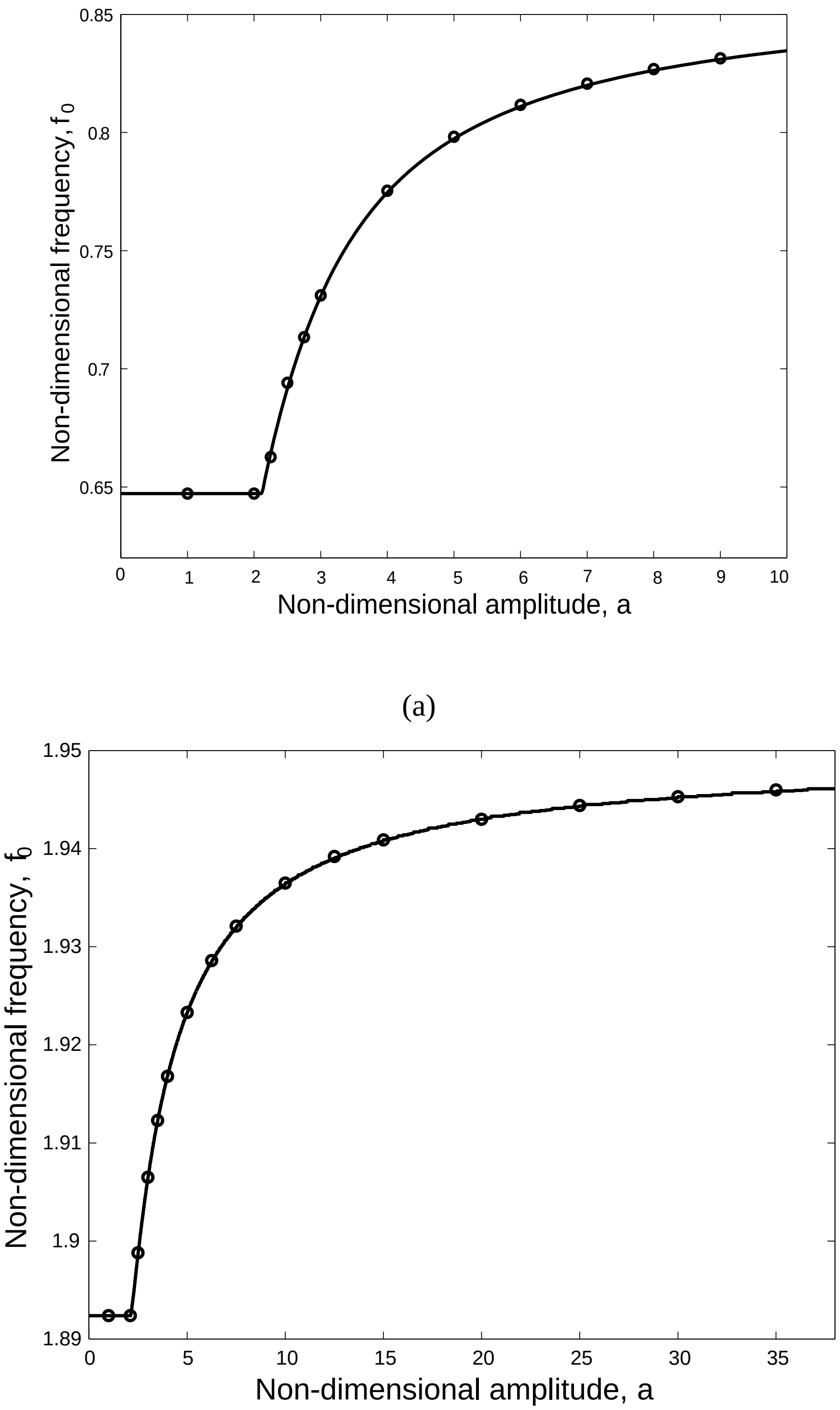

(a)

(b)

Figure 2.15: Response frequency for the nonlinear normal mode: ——, solution from direct integration of the system equations of motion; ‘ o ’ , time simulation of the dynamics restricted to the Galerkin-based manifold. (a) first mode; (b) second mode.

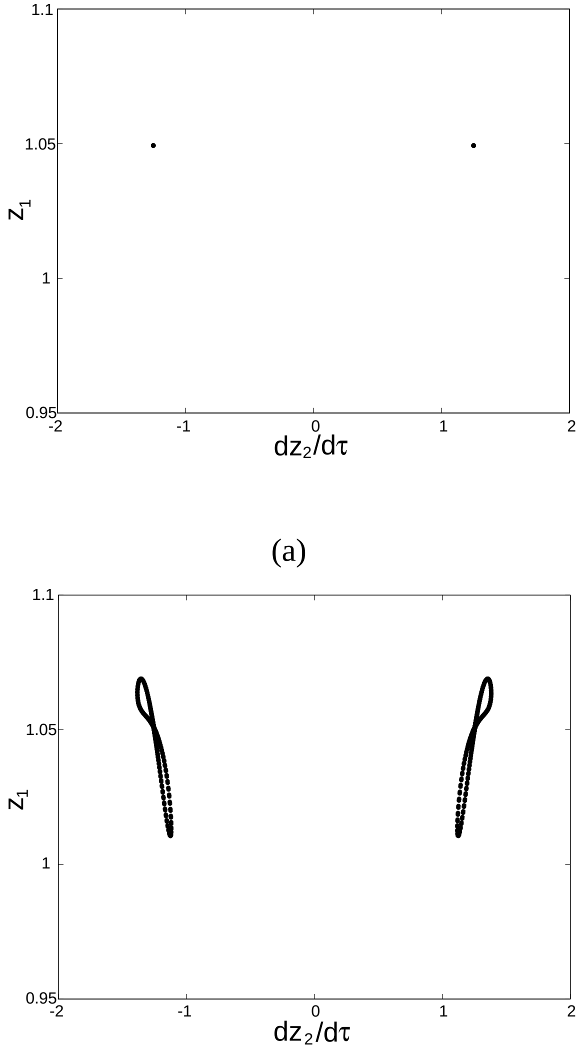

(a)

(b)

Figure 2.16: Poincaré sections of the motion initiated on the first NNM versus amplitude a: (a) $a = 3.82$; (b) $a = 3.83$.

CHAPTER III

THE CONSTRUCTION OF NONLINEAR NORMAL MODES FOR SYSTEMS WITH INTERNAL RESONANCE

3.1 Introduction

In order to obtain accurate reduced order models for nonlinear systems, “nonlinear modal analysis” has been proposed as an analogy to its linear counterpart. Initiated by Rosenberg [16], the concept of nonlinear normal modes (NNM) has been generalized by Shaw and Pierre [2, 3] through the introduction of invariant manifolds. A NNM invariant manifold is a two-dimensional surface in the system phase space that is tangent to the corresponding linear modal eigenspace at the equilibrium point. In order to parameterize these manifolds for vibratory systems, a single pair of state variables in linear modal coordinates (typically a modal displacement-velocity pair, or a modal amplitude and phase) are chosen as *master* coordinates for an individual NNM. Then, all the remaining degrees of freedom (DOF), the so-called *slave* coordinates, are constrained to these *master* coordinates in a particular manner, dictated by the equations of motion. The nonlinear partial differential equations (PDEs) describing the geometry of the manifold are produced using an approach that follows center manifold construction. Based on this methodology, a numerical framework for constructing NNMs, namely a Galerkin projection method [42], has been proposed and effectively applied to a variety of nonlinear systems, including systems with non-smooth restoring forces [54], as well as systems with non-proportional damping forces, non-symmetric nonlinearities, and gyroscopic terms [55]. Once the NNM invariant manifold is obtained, motions on it are governed by the dynamics of the corresponding *master* coordinates, which are described by two first-order ordinary differential equations. Note that these equations of motion are valid only for initial conditions on the invariant manifold.

Unlike linear modes, NNMs will interact during a general motion that is initiated by general initial conditions. Moreover, an invariant manifold approach that is based on a single mode reduction will break down in the presence of internal resonances between the *master* and any *slave* coordinates [56]. Hence, a nonlinear normal multi-mode methodology is required if one is interested in the multi-mode responses of nonlinear systems. Previous studies of NNMs with internal resonances were primarily based on perturbation methods [27, 34] or polynomial series expansions with the invariant manifold approach [29, 56]. These are applicable only in the weakly nonlinear regime. In order to obtain accurate reduced-order models for nonlinear systems with internal resonances in strongly nonlinear amplitude regimes, a new method for constructing invariant manifolds is proposed in this paper, as follows.

For an n-DOF nonlinear system with M modes involved in an internal resonance (or, more generally, with M modes to be retained for any reason), the multi-mode invariant manifold can be defined and obtained numerically in terms of $2M$ master coordinates (M displacement-velocity pairs or M amplitudes and phases). The procedure is outlined as follows. First, a transformation to polar coordinates is applied, as in the single-mode expansion case proposed by Pesheck *et al.* [42], to each pair of master coordinates. Then, the constraint functions for the slave coordinates are expressed in terms of these master coordinates, which are M amplitudes $\bar{a}$ and M phases $\bar{\phi}$. Since the master coordinates are represented by more than one amplitude-phase pair, the computation of the manifolds is much more complicated than in the single-mode case. To address this problem, a computational approach is proposed, which combines Galerkin projections in the phase coordinates and finite difference discretizations in the amplitude coordinates. Using this methodology, a $2M$-dimensional invariant manifold can, in principle, be constructed for the system, and motions on this manifold are governed by a set of $2M$ first-order differential equations in the master coordinates.

The multi-NNM approach is applied herein to a simple three-DOF system, as well as to a rotating blade model in which transverse motions are nonlinearly coupled with axial extensions of the blade. For the latter system, an 18-DOF discretized model derived from linear modal analysis is examined, which features an internal resonance between the first and second flapping modes. Using the multi-NNM procedure, the internally resonant four-dimensional invariant manifold is constructed and the resonant dynamics are shown to be accurately captured by the two-DOF (four state) reduced-order model.

The paper is organized as follows. The class of nonlinear systems under consideration and the formulation of the multi-mode invariant manifold equations are described in section 3.2. In section 3.3, the solution procedure for the invariant manifold is demonstrated on a 3-DOF example system. In section 3.4, the methodology is applied to an 18-DOF rotating beam system featuring an internal resonance between the first two flapping modes. Finally, some conclusions are drawn in section 3.5.

3.2 Multi-mode invariant manifolds

The vibratory system considered is an n-DOF autonomous nonlinear system, which can be obtained directly from Newton's laws, Lagrange's equations, finite element methods (FEM), or through any assumed-mode method. In order to simplify the construction procedure for the invariant manifolds, systems without damping or gyroscopic terms are considered (the method can be generalized to include these effects, but it is much more computationally intensive). For these systems, one can transform to linear modal coordinates, and the original nonlinear system can be expressed in the following standard form:

$$\ddot{\eta}_i + \omega_i^2 \eta_i = f_i(\eta_j), \qquad i, j = 1 \text{ to } n \tag{3.1}$$

where the η_i's are the linear modal coordinates, the ω_i's are the corresponding linear modal frequencies, and $f_i(\eta_j)$ is the i-th nonlinear force, which generally depends on all the linear modal coordinates, expressed in terms of the linear modal coordinates. It should be noted that the nonlinear forces, the $f_i(\eta_j)$'s, are assumed to be independent of the linear modal velocities, $\dot{\eta}_j$. With this assumption, the computational cost for the construction of the invariant manifolds can be significantly reduced.

In order to obtain accurate reduced-order models for nonlinear systems with internal resonances, multi-mode invariant manifolds must be constructed [56]. Here, an invariant manifold is defined as a multi-dimensional surface spanned by all the linear modal displacements and velocities involved in the internal resonance, such that any motion initiated on the manifold will remain on it for all times. Following this definition, the invariant manifold can be constructed in the following manner.

Let us assume that there are a total of M modes involved in an internal resonance for the nonlinear system defined in equation (3.1). These modes are described by a set of indices, denoted as S_M. According to the definition of invariant manifolds, each pair of state variables involved in the internal resonance, $(\eta_k, \dot{\eta}_k)$ $k \in S_M$, are chosen as *master* coordinates. Then all the remaining DOFs, namely the *slave* coordinates, are constrained such that they are dependent on the $2M$ *master* coordinates. A straightforward expression for the slave constraint functions is

$$\begin{cases} \eta_i = X_i(\eta_k, \dot{\eta}_k) \\ \dot{\eta}_i = Y_i(\eta_k, \dot{\eta}_k) \end{cases}, \quad \text{for } i \notin S_M, \;\; k \in S_M \tag{3.2}$$

This form has been utilized by Pesheck *et al.* [56] to carry out an asymptotic procedure for the construction of the invariant manifolds. In this approach, the constraint relationships, equation (3.2), are approximated by polynomial expansions in the master coordinates. Using this method, the domain of validity of the resulting solution is limited to some neighborhood of the system's equilibrium position. In addition, this approach does not allow one to systematically control the accuracy of the approximate solution. Hence, a new form for the master coordinates and the slave constraints is used here in order to overcome some of the inherent deficiencies of the polynomial expansion method.

For each pair of master coordinates, $(\eta_k, \dot{\eta}_k)\;\; k \in S_M$, a polar coordinate transformation is applied,

$$\begin{cases} \eta_k = a_k \cos(\phi_k) \\ \dot{\eta}_k = -a_k \omega_k \sin(\phi_k) \end{cases}, \quad \text{for } k \in S_M \tag{3.3}$$

where ω_k is the k-th linear modal frequency, and (a_k, ϕ_k) are the master coordinates in amplitude-phase form. Then, all the slave coordinates are expressed as functions of these amplitude-phase master coordinates,

$$\begin{cases} \eta_i = P_i(a_k, \phi_k) \\ \dot{\eta}_i = Q_i(a_k, \phi_k) \end{cases}, \quad \text{for } i \notin S_M, \;\; k \in S_M \tag{3.4}$$

where the slave coordinates are restricted to the domain defined by the M pairs of amplitude-phase variables. This domain is easily bounded, since the phase coordinate is periodic and the positive amplitude region can be dictated to a range of interest during the construction of the invariant manifold, as described below.

With the above polar form for the master coordinates and the slave constraint relationships, the partial differential equations governing the invariant manifold can be obtained as follows. For each pair of slave coordinates, $(\eta_i, \dot{\eta}_i)$, we have

$$\left\{\begin{array}{l} Q_i = \dot{P}_i = \sum_{k\in S_M}\left(\frac{\partial P_i}{\partial a_k}\dot{a}_k + \frac{\partial P_i}{\partial \phi_k}\dot{\phi}_k\right) \\ \\ \dot{Q}_i = \sum_{k\in S_M}\left(\frac{\partial Q_i}{\partial a_k}\dot{a}_k + \frac{\partial Q_i}{\partial \phi_k}\dot{\phi}_k\right) = -\omega_i^2 P_i + f_i \end{array}\right. , \quad \text{for } i \notin S_M$$

where ω_i and f_i are the i-th linear modal frequency and the nonlinear force defined in equation (3.1), respectively. In order to eliminate the explicit time dependence, $\dot{a}_k$ and $\dot{\phi}_k$ in equation (3.2) are replaced using the governing equation of motion for each pair of master coordinates, which are:

$$\left\{\begin{array}{l} \dot{a}_k = \frac{-f_k(\eta_j)}{\omega_k}\text{sin}\phi_k \\ \\ \dot{\phi}_k = \omega_k - \frac{f_k(\eta_j)}{\omega_k a_k}\text{cos}\phi_k \end{array}\right. , \quad \text{for } k \in S_M, \; j = 1 \text{ to } n \tag{3.5}$$

Substituting equation (3.5) into equation (3.2), the governing PDEs for the invariant manifold are found to be

$$\left\{\begin{array}{l} Q_i = \sum_{k\in S_M}\left[\frac{\partial P_i}{\partial a_k}\left(\frac{-f_k}{\omega_k}\text{sin}\phi_k\right) + \frac{\partial P_i}{\partial \phi_k}\left(\omega_k - \frac{f_k}{\omega_k a_k}\text{cos}\phi_k\right)\right] \\ \\ \sum_{k\in S_M}\left[\frac{\partial Q_i}{\partial a_k}\left(\frac{-f_k}{\omega_k}\text{sin}\phi_k\right) + \frac{\partial Q_i}{\partial \phi_k}\left(\omega_k - \frac{f_k}{\omega_k a_k}\text{cos}\phi_k\right)\right] = -\omega_i^2 P_i + f_i \end{array}\right. ,$$

$$\text{for } i \notin S_M \tag{3.6}$$

In equation (3.6), there are a total $(n - M)$ pairs of equations governing the invariant manifold, in terms of the constraint equations. These equations are nonlinear and have to be solved in some approximate manner; here this is done numerically. Once they are solved, the results for all of the slave constraints, P_i and Q_i for $i \notin S_M$, can be substituted into the M pairs of ordinary differential equations governing the dynamics of the master coordinates, equation (3.5). As a result, the response of the original system restricted to the invariant manifold is captured by this $2M$-DOF reduced-order model. The procedure for obtaining the numerical solution for the invariant manifolds is described in the context of a simple example, and then applied to a more substantial problem.

3.3 A three-DOF example system

Figure 3.1 depicts a three-DOF mass-spring system with two cubic nonlinear springs of coefficients γ_1 and γ_2, attached to masses M_1 and M_3, respectively. The system parameters are tuned so that the second linear modal frequency is approximately three times the first one, that is, $\omega_2 \approx 3\omega_1$. Consequently, a three-to-one internal resonance occurs between the first and second linear modes.

Using linear modal coordinates, the system can be transformed to the standard form shown in equation (3.1),

$$\ddot{\eta}_i + \omega_i^2 \eta_i = f_i(\eta_j) \quad \text{for } i, j = 1, 2, 3 \tag{3.7}$$

where the modal coordinates η_i are defined by the linear modal transformation:

$$\left\{ \begin{array}{c} x_1 \\ x_2 \\ x_3 \end{array} \right\} = \left[\begin{array}{ccc} 0.5870 & -0.5147 & 0.6249 \\ 0.6039 & -0.2357 & -0.7614 \\ 0.5392 & 0.8243 & 0.1725 \end{array} \right] \left\{ \begin{array}{c} \eta_1 \\ \eta_2 \\ \eta_3 \end{array} \right\}$$

The linear modal frequencies are $\omega_1 = 0.5972$ rad/s, $\omega_2 = 1.792$ rad/s, and $\omega_3 =$

3.405 rad/s, and the nonlinear forces are

$$\begin{cases} f_1 = 0.587\,(-0.587\,\eta_1 + 0.5147\,\eta_2 - 0.6249\,\eta_3)^3 \\ \qquad\quad - 0.8088\,(0.5392\,\eta_1 + 0.8243\,\eta_2 + 0.1725\,\eta_3)^3 \\ \\ f_2 = -0.5147\,(-0.587\,\eta_1 + 0.5147\,\eta_2 - 0.6249\,\eta_3)^3 \\ \qquad\quad - 1.2365\,(0.5392\,\eta_1 + 0.8243\,\eta_2 + 0.1725\,\eta_3)^3 \\ \\ f_3 = 0.6249\,(-0.587\,\eta_1 + 0.5147\,\eta_2 - 0.6249\,\eta_3)^3 \\ \qquad\quad - 0.2588\,(0.5392\,\eta_1 + 0.8243\,\eta_2 + 0.1725\,\eta_3)^3 \end{cases} \tag{3.8}$$

In the presence of an internal resonance between the first two modes, the master coordinates are chosen as the state variable pairs $(\eta_1, \dot{\eta}_1)$ and $(\eta_2, \dot{\eta}_2)$. The corresponding master coordinate index set is $S_M = \{1, 2\}$. The polar coordinate transformation is applied to these state variable pairs according to the definition in equation (3.3). As a result, the transformed master coordinates are expressed in terms of the amplitude-phase pairs, (a_1, ϕ_1) and (a_2, ϕ_2).

As defined in equation (3.4), the constraint relationships for the slave coordinates are

$$\begin{cases} \eta_3 = P_3(a_1, a_2, \phi_1, \phi_2) \\ \dot{\eta}_3 = Q_3(a_1, a_2, \phi_1, \phi_2) \end{cases}$$

The governing PDEs for the invariant manifold are given in equation (3.6) and are rewritten here as

$$\begin{aligned} Q_3 = {} & \frac{\partial P_3}{\partial a_1}\left(\frac{-f_1 \sin\phi_1}{\omega_1}\right) + \frac{\partial P_3}{\partial \phi_1}\left(\omega_1 - \frac{f_1 \cos\phi_1}{\omega_1 a_1}\right) \\ & + \frac{\partial P_3}{\partial a_2}\left(\frac{-f_2 \sin\phi_2}{\omega_2}\right) + \frac{\partial P_3}{\partial \phi_2}\left(\omega_2 - \frac{f_2 \cos\phi_2}{\omega_2 a_2}\right), \end{aligned} \tag{3.9}$$

$$\begin{aligned} & \frac{\partial Q_3}{\partial a_1}\left(\frac{-f_1 \sin\phi 1}{\omega_1}\right) + \frac{\partial Q_3}{\partial \phi_1}\left(\omega_1 - \frac{f_1 \cos\phi_1}{\omega_1 a_1}\right) \\ & + \frac{\partial Q_3}{\partial a_2}\left(\frac{-f_2 \sin\phi 2}{\omega_2}\right) + \frac{\partial Q_3}{\partial \phi_2}\left(\omega_2 - \frac{f_2 \cos\phi_2}{\omega_2 a_2}\right) = -\omega_3^2 P_3 + f_3\,. \end{aligned} \tag{3.10}$$

Equations (3.9) and (3.10) are defined in the four-dimensional space spanned by the amplitude-phase pairs (a_1, ϕ_1) and (a_2, ϕ_2). A numerical solution scheme is given here to approximate the unknown constraint relationships, $P_3(a_1, a_2, \phi_1, \phi_2)$ and $Q_3(a_1, a_2, \phi_1, \phi_2)$, which define the geometry of the four-dimensional invariant manifold. In the two-dimensional phase region, defined by

$$\{\ (\phi_1, \phi_2) \mid \phi_1 \in [0, 2\pi],\ \phi_2 \in [0, 2\pi]\ \}\ ,$$

the constraint relationships, P_3 and Q_3, are periodic in both ϕ_1 and ϕ_2. Hence, they can be efficiently approximated by two-dimensional Fourier series. In the two-dimensional amplitude domain, defined by

$$\{\ (a_1, a_2) \mid 0 < a_1 < a_{1max},\ 0 < a_2 < a_{2max}\ \}\ ,$$

where the upper limits a_{1max} and a_{2max} are set during the numerical construction procedure, finite difference discretization methods can be used to approximate the unknown constraint equations by a sequence of overlapping polynomials that interpolate P_3 and Q_3 at a set of grid points. It should be noticed that the region of two lines, $\{\ (a_1, a_2) \mid a_1 = 0 \text{ or } a_2 = 0\ \}$, is excluded from the two-dimensional amplitude domain in the finite difference scheme, since this region is not defined in the governing partial differential equations for the invariant manifold. With the combination of finite difference methods and two-dimensional Fourier series expansions, the unknown constraint equations, P_3 and Q_3, can be approximated at each grid point as

$$P_3(a_1^i, a_2^j, \phi_1, \phi_2) \approx \sum_{l=1}^{N_{\phi_1}} \sum_{m=1}^{N_{\phi_2}} C_{lm}^{(i,j)} F_l(\phi_1) F_m(\phi_2) \tag{3.11}$$

$$Q_3(a_1^i, a_2^j, \phi_1, \phi_2) \approx \sum_{l=1}^{N_{\phi_1}} \sum_{m=1}^{N_{\phi_2}} D_{lm}^{(i,j)} F_l(\phi_1) F_m(\phi_2) \tag{3.12}$$

where (a_1^i, a_2^j) is the grid point determined by the finite difference scheme in the amplitude region; indices i and j denote the location of the grid point along the a_1 and a_2 directions, respectively; the Fourier terms, $F_l(\phi_1)$ and $F_m(\phi_2)$, are defined as:

$$F_l(\phi) = \begin{cases} \cos\frac{l-1}{2}\phi, & l \text{ is odd} \\ \sin\frac{l}{2}\phi, & l \text{ is even;} \end{cases} \tag{3.13}$$

and N_{ϕ_1} and N_{ϕ_2} are the number of terms of the Fourier expansions in ϕ_1 and ϕ_2, respectively. As can be seen in equations (3.11–3.13), the total number of the unknown quantities are determined by N_{ϕ_1} and N_{ϕ_2}, as well as the number of grid points. Once the unknown coefficients, the C's and D's in expressions (3.11) and (3.12), have been obtained at all grid points, the invariant manifold is completely determined in this approximate manner.

Given the expression of P_3 and Q_3 at each grid point, the derivatives of the local interpolant are used to approximate the derivatives of P_3 and Q_3 with respect to a_1 or a_2. Simple two-point backward interpolation gives

$$\begin{aligned} \frac{\partial P_3}{\partial a_1}(a_1^i, a_2^j, \phi_1, \phi_2) &\approx \frac{1}{h_1}\Big[P_3(a_1^i, a_2^j, \phi_1, \phi_2) \\ &\qquad - P_3(a_1^{i-1}, a_2^j, \phi_1, \phi_2)\Big] + O(h_1) \\ \frac{\partial P_3}{\partial a_2}(a_1^i, a_2^j, \phi_1, \phi_2) &\approx \frac{1}{h_2}\Big[P_3(a_1^i, a_2^j, \phi_1, \phi_2) \\ &\qquad - P_3(a_1^i, a_2^{j-1}, \phi_1, \phi_2)\Big] + O(h_2) \end{aligned} \tag{3.14}$$

where $h_1 = a_1^i - a_1^{i-1}$, $h_2 = a_2^j - a_2^{j-1}$ are the distances between adjacent grid points along the a_1 and a_2 directions, respectively. The function $O(\cdot)$ denotes that the errors in these approximations are orders-of-magnitude h_1 and h_2, respectively. If more grid points are used in the approximation for a given amplitude range, higher accuracy is obtained. The approximation of the derivatives, $\partial Q_3/\partial a_1$ and $\partial Q_3/\partial a_2$, is determined using a similar scheme. Along the ϕ_1 or ϕ_2 directions, the derivatives of the unknown functions P_3 and Q_3 can be easily obtained using the two-dimensional Fourier series expansions given in expressions (3.11) and (3.12).

The computational time associated with the construction of the invariant manifold depends on the number of unknown coefficients, which depends on the number of grid points selected for the amplitude variables and the number of harmonics employed in the Fourier series. For this example system, the total number of unknown coefficients, C's and D's, can be reduced to one-fourth its original number by exploiting the inherent relationship between Q_3 and P_3, along with the symmetric nature of the nonlinear forces, which are cubic and depend only on the displacement variables. The details of these simplifications are now described.

For a given set of values for the C's, the expression of the velocity constraint, Q_3, can be explicitly determined from the following relationship:

$$\begin{aligned} Q_3(a_1^i, a_2^j, \phi_1, \phi_2; C) \approx\ & \frac{\partial P_3}{\partial a_1}(a_1^i, a_2^j, \phi_1, \phi_2; C) \\ \times & \left[- f_1(a_1^i, a_2^j, \phi_1, \phi_2; C) \frac{\sin\phi_1}{\omega_1} \right] + \frac{\partial P_3}{\partial \phi_1}(a_1^i, a_2^j, \phi_1, \phi_2; C) \\ \times & \left[\omega_1 - f_1(a_1^i, a_2^j, \phi_1, \phi_2; C) \frac{\cos\phi_1}{\omega_1 a_1} \right] + \frac{\partial P_3}{\partial a_2}(a_1^i, a_2^j, \phi_1, \phi_2; C) \\ \times & \left[- f_2(a_1^i, a_2^j, \phi_1, \phi_2; C) \frac{\sin\phi_2}{\omega_2} \right] + \frac{\partial P_3}{\partial \phi_2}(a_1^i, a_2^j, \phi_1, \phi_2; C) \\ \times & \left[\omega_2 - f_2(a_1^i, a_2^j, \phi_1, \phi_2; C) \frac{\cos\phi_2}{\omega_2 a_2} \right], \end{aligned} \tag{3.15}$$

which is the algebraic form of equation (3.9). Note that the nonlinear forces, f_1 and f_2, in equation (3.15) are only dependent on the C's, since all the nonlinear forces are defined in terms of the displacement field only, equation (3.8). Otherwise, the relationship for Q_3 would be implicit. The velocity constraint, Q_3, would then have to be expanded as given in expression (3.12). The unknown coefficients, D's, would need to be solved for simultaneously with the C's, in an iterative manner.

From expression (3.15), the velocity constraint Q_3 at each grid point (a_1^i, a_2^j) is evaluated numerically at the following set of phase angles,

$$Q_3(a_1^i, a_2^j, \bar{\phi}_1^I, \bar{\phi}_2^J) \quad \text{where} \begin{cases} \bar{\phi}_1^I = I\pi/N_{\phi_1} \\ \bar{\phi}_2^J = J\pi/N_{\phi_2}, \end{cases}$$
$$\text{for } I = 1 \ldots 2N_{\phi_1}, \quad J = 1 \ldots 2N_{\phi_2} \;.$$

Then, a two-dimensional Fast Fourier Transform (FFT) can be applied to these $2N_{\phi_1} \times 2N_{\phi_2}$ discrete grid point values in order to obtain the two-dimensional Fourier coefficients corresponding to function Q_3:

$$Q_3(a_1^i, a_2^j, \phi_1, \phi_2) = \sum_{m=\frac{-N_{\phi_1}}{2}}^{\frac{N_{\phi_1}}{2}} \sum_{n=\frac{-N_{\phi_2}}{2}}^{\frac{N_{\phi_2}}{2}} \tilde{D}_{mn}^{(i,j)} e^{\sqrt{-1}m\phi_1} e^{\sqrt{-1}n\phi_2} \tag{3.16}$$

where the $\tilde{D}$'s are the complex version of the D coefficients, as defined in equation (3.12), and N_{ϕ_1}, N_{ϕ_2} are set to be even. Note that $2N_{\phi_1} \times 2N_{\phi_2}$ grid points in phase domain are used to evaluate the $N_{\phi_1} \times N_{\phi_2}$ complex Fourier coefficients in equation (3.16), in order to reduce aliasing errors in the Fourier transform. Once the Fourier coefficients are obtained, the first order derivatives, $\partial Q_3/\partial\phi_1$ and $\partial Q_3/\partial\phi_2$, in equation (3.10) can be efficiently calculated by the two-dimensional Inverse Fast Fourier Transform (IFFT). The derivatives of Q_3 with respect to a_1 or a_2 can also be obtained by the backward finite difference scheme defined in equation (3.14). By this method, the total number of unknown coefficients in equation (3.11) and (3.12) can be cut in half. Specifically, only the C coefficients need to be obtained.

For this example system, the nonlinear forces in equation (3.8) are only cubic. As a result, half of the Fourier series in equation (3.11) can be eliminated. In particular, in the two-dimensional Fourier series expansion of the constraint function P_3, only the trigonometric basis functions whose combination orders are odd need to be included. With respect to each individual basis function, $F_l(\phi_1)F_m(\phi_2)$, in equation (3.11), the subscripts of the corresponding C coefficient can be used as a guide to determine whether or not the associated basis function shall be retained. If int$[l/2]+$ int$[m/2]$ is odd, the corresponding basis function is retained in the expansion, otherwise it is removed (where the operator int$[a]$ denotes the maximum integer which is not larger than a). As a result, the total number unknown coefficients in equation (3.11) is halved again.

At this stage, the constraint function P_3 at a grid point is approximated by the reduced two-dimensional Fourier series and can be expressed in the following simplified form:

$$P_3(a_1^i, a_2^j, \phi_1, \phi_2) \approx \sum_{\alpha=1}^{N_\alpha} C_\alpha^{(i,j)} T_\alpha(\phi_1, \phi_2) \tag{3.17}$$

where (a_1^i, a_2^j) is a grid point in the amplitude domain of interest, N_α is the total number of expansion functions, $T_\alpha(\phi_1, \phi_2)$ is a simplified notation for the individual basis functions defined in equation (3.11), with odd harmonic combination order, and $C_\alpha^{(i,j)}$ is the corresponding unknown coefficient. Given an initial guess for the C_α's at all grid points in the amplitude domain, the complex Fourier coefficients, $\tilde{D}$'s, for the velocity constraint Q_3 are obtained from equations (3.15) and (3.16). Then, the value of Q_3 and the corresponding partial derivatives are substituted into equation (3.10) along with the value of P_3. The corresponding residual function, R_3, is defined at each grid point (a_1^i, a_2^j) as follows.

$$\begin{aligned} R_3(a_1^i, a_2^j, \phi_1, \phi_2; C_\alpha) = {} & \frac{\partial Q_3}{\partial a_1}(a_1^i, a_2^j, \phi_1, \phi_2; C_\alpha) \\ & \times \left[- f_1(a_1^i, a_2^j, \phi_1, \phi_2; C_\alpha)\frac{\sin\phi_1}{\omega_1}\right] + \frac{\partial Q_3}{\partial \phi_1}(a_1^i, a_2^j, \phi_1, \phi_2; C_\alpha) \\ & \times \left[\omega_1 - f_1(a_1^i, a_2^j, \phi_1, \phi_2; C_\alpha)\frac{\cos\phi_1}{\omega_1 a_1}\right] + \frac{\partial Q_3}{\partial a_2}(a_1^i, a_2^j, \phi_1, \phi_2; C_\alpha) \\ & \times \left[- f_2(a_1^i, a_2^j, \phi_1, \phi_2; C_\alpha)\frac{\sin\phi_2}{\omega_2}\right] + \frac{\partial Q_3}{\partial \phi_2}(a_1^i, a_2^j, \phi_1, \phi_2; C_\alpha) \\ & \times \left[\omega_2 - f_2(a_1^i, a_2^j, \phi_1, \phi_2; C_\alpha)\frac{\cos\phi_2}{\omega_2 a_2}\right] \\ & + \omega_3^2 P_3(a_1^i, a_2^j, \phi_1, \phi_2; C_\alpha) - f_3(a_1^i, a_2^j, \phi_1, \phi_2; C_\alpha) \end{aligned} \tag{3.18}$$

In order to minimize the residual function R_3, a “weighted residuals” Galerkin method is used, in which the projection of the residual function onto the basis function is required to vanish:

$$\int_0^{2\pi}\int_0^{2\pi}\left[T_\alpha(\phi_1,\phi_2)\times R_3(a_1^i,a_2^j,\phi_1,\phi_2;C_\alpha)\right]d\phi_1\,d\phi_2=0, \tag{3.19}$$
$$\text{for } \alpha=1\dots N_\alpha, \quad \text{at } \forall\,(a_1^i,a_2^j),$$

where T_α is the basis function in equation (3.17). Equation (3.19) yields a set of nonlinear algebraic equations in the unknown coefficients C_α. These are solved using a nonlinear solver found in the subroutine package NAG, which is based on Powell's hybrid method [57]. The user must, (i) provide an initial guess for the unknown coefficients in equation (3.17), and (ii) evaluate the "weighted residuals", the left hand side of equation (3.19), by numerical integration.

The resulting four-dimensional invariant manifold cannot be visualized in three-dimensional space. However, we can show specific cross sections of the manifold. In figure 3.2, the slave constraint relationship P_3 is depicted at the phase angles $(\phi_1,\phi_2)=(0,0)$. The two-dimensional amplitude domain (a_1,a_2), in which the invariant manifold is numerically constructed, is arbitrary set as $a_1\in[0.01,0.35]$ and $a_2\in[0.01,0.35]$. Through convergence study, an 11-by-11 grid finite difference scheme is chosen to discretize this domain. The mesh size, h_1 and h_2, is equal to 0.034 in both the a_1 and a_2 directions. In figure 3.2, the invariant manifold looks smooth with this mesh scheme, which indicates this 11-by-11 discretization is sufficient to capture its geometry in the amplitude domain.

The domain defined by (ϕ_1,ϕ_2), where $\phi_1\in[0,2\pi]$ and $\phi_2\in[0,2\pi]$, is a two-dimensional torus. The invariant manifold at any grid point (a_1^i,a_2^j) can be visualized in this torus domain. In figure 3.3(a), the phase angle ϕ_1 is defined by the angle from vector $\overrightarrow{Or_0}$ to vector $\overrightarrow{Or}$. At phase angle ϕ_1, a cross section of the invariant manifold along the plane rOz is shown in figure 3.3(b). In this cross section, the shape of the invariant manifold is shown by the vector $\overrightarrow{\rho}$, which indicates the magnitude of the manifold at phase angle ϕ_2. For comparison, the nominal torus domain is also shown here as a circle with a dashed line, on which the magnitude of the invariant manifold is zero. For the solution shown in figure 3.2, the number of terms for the two-dimensional Fourier series in expression (3.11) is set as $N_{\phi_1} = N_{\phi_2} = 12$ for each grid point. Since the nonlinear forces are cubic for this example system, the total number of basis functions in the two-dimensional phase space is reduced to $N_\alpha = 72$ in expression (3.17). As a result, the total number of unknown coefficients, the C_α's in expression (3.17) for all of the 11×11 grid points in the two-dimensional amplitude domain, is equal to $8,712$ for the construction of the constraint relationship P_3. For each unknown coefficient C_α, zero is used as the initial guess value to start the Powell's hybrid method.

Once the constraint relationship, P_3, is obtained for this internal resonance case, system motions on the invariant manifold can be captured by the reduced-order model, which involves the master coordinates only. As shown in equation (3.5), numerical time simulations can be carried out for these four first-order differential equations for given initial conditions, $a_1(0)$, $\phi_1(0)$, $a_2(0)$, and $\phi_2(0)$. In figure 3.4, time simulations for the master coordinates are shown using the reduced-order model with two DOFs and the original three-DOF model restricted to the invariant manifold. Based on the reduced-order model, equation (3.5), the responses of the amplitude-phase pairs are simulated. Then, the responses of the modal coordinates are obtained using the definition of the polar coordinate transformation. For comparison, the time responses for the master coordinates can also be acquired by the direct time simulation of the original system, equation (3.7), since the initial conditions for the slave coordinates $\eta_3(0)$ and $\dot{\eta}_3(0)$ can be obtained using the slave constraint function P_3 and Q_3. According to the definition of the invariant manifold, any motion initiated on the manifold will remain on it for all the time, indicating that the simulation obtained from the original model should match the response from the reduced-order model if the invariant manifold has been constructed accurately enough to capture the actual geometry. In figure 3.4, the two categories of time responses are undistinguishable, indicating that the manifold geometry is accurate.

With the reduced-order model, time responses for the slave coordinates $(\eta_3, \dot{\eta}_3)$ can be obtained from the constraint relationships P_3 and Q_3. In figure 3.5(a) and (b), these responses are compared to simulations based on the original system model. An excellent match between these two results is observed, which is further evidence to the accuracy of the invariant manifold. The time response of any physical coordinate, i.e., the displacement or velocity of any mass in figure 3.1, can be determined from the simulation of the reduced-order model, since the responses of all modal coordinates, both masters and slaves, are calculated. The displacement and velocity of mass M_3, $X_3(t)$ and $\dot{X}_3(t)$, are shown in figure 3.5(c) and (d). Again, excellent agreement is found between the results for the reduced-order and original system models.

3.4 The rotating beam system

Here the methodology is applied to a vibratory system of more practical interest, and with more degrees of freedom. A uniform rotating Euler-Bernoulli beam, shown in figure 3.6, is considered. This system has been studied by Pesheck *et al.* [56], who approximated the invariant manifold in the case of an internal resonance using asymptotic methods. Apiwattanalunggarn *et al.* [58] also studied the same system and obtained the single-mode nonlinear invariant manifold for large amplitude motions. This rotating beam system can be considered as a highly simplified model of a helicopter rotor blade, in which the following effects are neglected: lead-lag motion, torsional motion, aerodynamic loading, and the weight of the blade. Even with this over-simplified model, it has been shown that typical discretization procedures for this system suffer from very slow modal convergence, since a comparatively large number of axial modes must be included in order to capture accurately the transverse bending motion [56, 58]. Due to the nonlinear axial/bending coupling effects, the resulting discrete models are computationally cumbersome, even for direct time simulations. Hence, a practical model order reduction technique would be very useful for the analysis of such systems.

A detailed derivation of the PDE's governing the transverse bending, $w(x,t)$, and the axial elongation, $u(x,t)$, of this beam can be found in reference [56]. The derivation procedure is briefly described here. The potential energy, U, and kinetic energy, T, may be expressed as follows.

$$\begin{aligned} T &= \frac{1}{2}\int_0^L m(\dot{u}^2+\dot{w}^2)+m\Omega^2(h+x+u)^2dx \qquad (3.20) \\ U &= \frac{1}{2}\int_0^L EI(w_{,xx})^2+EA(u_{,x}+\frac{1}{2}(w_{,x})^2)^2dx \qquad (3.21) \end{aligned}$$

where $w(x,t)$ and $u(x,t)$ are the transverse and axial displacement respectively, $()_{,x}$ denotes a partial derivative with respect to the spatial variable x, and $\dot{()}$ represents a time derivative. It should be noted that the standard linear curvature assumption is made in the energy expressions in order to evidence the slow modal convergence even with the simplest model [56]. Hamilton's principle is used to develop the weak formulation for the equation of motion.

$$\begin{aligned} \int_{t_1}^{t_2}\int_0^L \Big\{ &[-m\ddot{w}-EIw_{,xxxx}]\delta w-[EA(u_{,x}+\frac{1}{2}(w_{,x})^2)w_{,x}]\delta w_{,x} \\ &+[-m\ddot{u}+m\Omega^2(x+h+u)+EAu_{,xx}]\delta u \\ &-[EA\frac{1}{2}(w_{,x})^2]\delta u_{,x}\Big\}dxdt=0 \qquad (3.22) \end{aligned}$$

where $\delta()$ denotes the variation of a quantity.

In order to obtain the discretized version of the equations of motion in the standard form (3.1), the linearized partial differential equations of the nonlinear rotating beam system are given here.

$$m\ddot{u}_d - m\Omega^2 u_d - EAu_{d,xx} = 0 \tag{3.23}$$

$$m\ddot{w} + EIw,_{xxxx} - EA(u_{s,x}w,_{xx} + u_{s,xx}w,_x) = 0 \tag{3.24}$$

where u_d is the dynamic component of the axial elongation, $u(x,t)$, defined as

$$u_d(x,t) = u(x,t) - u_s(x) \tag{3.25}$$

The static part, $u_s(x)$, is the static elongation of the beam due to rotation when the transverse deflection is zero. Linear mode shapes corresponding to equation (3.23) and (3.24) can be obtained using a Rayleigh-Ritz procedure. Once these modes are determined, the solutions to the nonlinear system (3.22) are sought in the form of an expansion as

$$u_d(x,t) = \sum_{i=1}^{N_\eta} \eta_i(t)\bar{U}_i(x) \qquad , w(x,t) = \sum_{i=1}^{N_\xi} \xi_i(t)\bar{W}_i(x) \tag{3.26}$$

where $\bar{U}_i$ and $\bar{W}_i$ are the linear modes corresponding to equations (3.23) and (3.24), and the integers N_η and N_ξ denote the number of axial and transverse linear modes used, respectively.

These expansions are substituted into the weak formulation, equation (3.22), and the discretized nonlinear equations of motion are obtained as follows:

$$\ddot{\eta}_i + \omega_{\eta,i}^2 \eta_i = f_{\eta,i}(\xi_j) \quad \text{for } i = 1 \text{ to } N_\eta,\ \ j = 1 \text{ to } N_\xi \tag{3.27}$$

$$\ddot{\xi}_i + \omega_{\xi,i}^2 \xi_i = f_{\xi,i}(\xi_j, \eta_k) \ \text{ for } i,j = 1 \text{ to } N_\xi,\ \ k = 1 \text{ to } N_\eta \tag{3.28}$$

where $\omega_{\eta,i}$ and $\omega_{\xi,i}$ are the linear modal frequencies associated with the i-th modes in the axial and transverse directions, respectively. These equations of motion are nonlinearly coupled because the quadratic nonlinear forces corresponding to the axial motion, $f_{\eta,i}$, depend on the transverse motion ξ_j, while the quadratic and cubic nonlinear forces in the transverse direction, $f_{\xi,i}$, are dependent on both axial and transverse motions, ξ_j and η_k.

The convergence of this model has been thoroughly investigated in reference [56]. It has been found that at least an 18-DOF model, with $N_\eta = N_\xi = 9$, must be used to accurately capture the periodic response in the vicinity of the first nonlinear mode for an energy level corresponding to a transverse deflection amplitude of about 0.1m at the beam tip, for a 9.0m beam. This 18-DOF discretized model is used here as the *reference model*. Based on this model, the invariant manifold is constructed. Consequently, a reduced-order model can be obtained for the representation of the dynamics on the invariant manifold.

As in the case studied in reference [56], the parameters of the uniform rotating beam are set as follows: $L = 9\,\mathrm{m}$, $m = 10\,\mathrm{kg/m}$, $EI = 3.99 \times 10^5\,\mathrm{N} \cdot \mathrm{m}^2$, $EA = 2.23 \times 10^8\,\mathrm{N}$, $\Omega = 23.85\,\mathrm{rad/s}$, and $h = 0.5\,\mathrm{m}$. Under these conditions, a three-to-one internal resonance occurs between the first two transverse modes, $\omega_{\xi,2} \approx 3\,\omega_{\xi,1}$. The master coordinates are chosen as the state variable pairs, $(\xi_1, \dot{\xi}_1)$ and $(\xi_2, \dot{\xi}_2)$. Polar coordinate transformations, defined in equation (3.3), are applied to these two pairs of state variables, resulting in two amplitude-phase pairs as the transformed master coordinates, (a_1, ϕ_1) and (a_2, ϕ_2). All the remaining DOF's, including 7 transverse deflection modes and 9 axial modes, form the slave coordinates, which are constrained as follows,

$$\begin{cases} \xi_i = P_i(a_1, a_2, \phi_1, \phi_2), \;\; \dot{\xi}_i = Q_i(a_1, a_2, \phi_1, \phi_2), \;\; i = 3 \ldots 9, \\ \eta_i = P_{i+9}(a_1, a_2, \phi_1, \phi_2), \;\; \dot{\eta}_i = Q_{i+9}(a_1, a_2, \phi_1, \phi_2), \;\; i = 1 \ldots 9. \end{cases} \tag{3.29}$$

Thus, there are a total of 16 pairs of constraint relationships, equation (3.29), that need to be solved. The governing PDE's for these constraint functions are given in equation (3.6).

The invariant manifold is solved for numerically in the following four-dimensional domain:

$$\begin{aligned}\Big\{\ (a_1, a_2, \phi_1, \phi_2) \quad | \quad & a_1 \in [0.01, 0.75],\ a_2 \in [0.01, 0.4], \\ & \phi_1 \in [0, 2\pi],\ \phi_2 \in [0, 2\pi]\ \Big\},\end{aligned}$$

where the amplitude range is carefully chosen so that the nonlinear effect in the system is sufficiently strong and the invariant manifold obtained from the asymptotic expansion method in reference [56] is incorrect in this domain.

In the solution procedure, the constraint relationships for the velocities, Q_i's, in equation (3.29) are not solved for, due to the fact that the velocity constraint is the time derivative of the corresponding displacement constraint. The details of the reduction have been given in section 3.3, equations (3.15) and (3.16), for the construction of the invariant manifold of the 3-DOF example system. Hence, only the displacement constraint relationships, P_i's, need to be solved.

For the two-dimensional phase domain, (ϕ_1, ϕ_2), the two-dimensional Fourier series, defined in equation (3.11), is utilized for the expansion functions for the displacement constraints. Because both quadratic and cubic nonlinear terms exist in this system, so that the expansion cannot be further simplified. For the two-dimensional amplitude domain, (a_1, a_2), the finite difference discretization scheme, which was used in the 3-DOF example system, cannot be utilized here due to limitations in computational capacity. The numerical difficulty is clearly shown by the following case: Lets us divide the two-dimensional amplitude domain into 8-by-8 grid points, and set the number of terms in the Fourier expansion as $N_{\phi_1} = N_{\phi_2} = 8$ at each grid point. Then, the total number of unknown coefficients is 4,096 for each displacement constraint relationship, P_i. With 16 slave constraints in equation (3.29), the final number of unknowns is 65,536. It is inefficient to solve for the invariant manifold with such a large number of unknowns.

A strategy to overcome this numerical difficulty is to discretize the two-dimensional amplitude domain into small elements, and then utilize low-order polynomials as expansion functions in the discretized elements. For this example system, the amplitude domain, $\{(a_1, a_2) \mid a_1 \in [0.01, 0.75],\ a_2 \in [0.01, 0.4]\}$, is evenly divided into 7-by-7 equal-sized patches. The width of each patch is 0.1057 along the a_1 direction, and 0.05571 along the a_2 direction. The displacement constraint relationships, P_i's, in equation (3.29) are then expanded in each discretized four-dimensional element,

$$\begin{aligned}\Big\{\ (a_1, a_2, \phi_1, \phi_2) \quad \Big| \quad & a_1 \in [a_1^{low}, a_1^{up}],\ a_2 \in [a_2^{low}, a_2^{up}], \\ & \phi_1 \in [0, 2\pi],\ \phi_2 \in [0, 2\pi]\ \Big\},\end{aligned} \tag{3.30}$$

as

$$\begin{aligned}& P_i(a_1, a_2, \phi_1, \phi_2) \approx \sum_{j=1}^{2}\sum_{k=1}^{2}\sum_{l=1}^{N_{\phi_1}}\sum_{m=1}^{N_{\phi_2}} C_{i,jklm} T_j(a_1) T_k(a_2) F_l(\phi_1) F_m(\phi_2), \\ & \text{for } \ i = 3 \ldots 18,\end{aligned} \tag{3.31}$$

where $T_j(a_1)$ are the piecewise linear functions defined in the amplitude segment, $a_1 \in [a_1^{low}, a_1^{up}]$, as follows,

$$T_1(a_1) = \frac{a_1 - a_1^{low}}{a_1^{up} - a_1^{low}}, \quad T_2(a_1) = \frac{a_1^{up} - a_1}{a_1^{up} - a_1^{low}}. \tag{3.32}$$

The definition of the piecewise linear functions, $T_k(a_2)$, is the same as for $T_j(a_1)$, while the lower and upper limits of the amplitude segment are set as $a_2 \in [a_2^{low}, a_2^{up}]$. The Fourier terms, $F_l(\phi_1)$ and $F_m(\phi_2)$, are defined in equation (3.13).

In each element, given by equation (3.30), the deduction of the velocity constraint (Q_i) from the corresponding displacement constraint (P_i), and the evaluation of the residue function, R_i, are again given by equations (3.15), (3.16), and (3.18). It should be noted that in the present example, the numerical values of the velocity constraints (Q_i) and the residue functions (R_i) are now evaluated at the Gaussian quadrature points for polynomials in the discretized two-dimensional amplitude domain. A three-by-three-point Gaussian quadrature formula is sufficient in the region, $\{(a_1,a_2)\mid a_1\in[a_1^{low},a_1^{up}],a_2\in[a_2^{low},a_2^{up}]\}$, using the inner product between the residue functions (R_i's) and the basis functions defined in equation (3.31). This yields,

$$\begin{aligned}\int_{a_1^{low}}^{a_1^{up}}\int_{a_2^{low}}^{a_2^{up}}\int_0^{2\pi}\int_0^{2\pi}\Big[&T_j(a_1)T_k(a_2)F_l(\phi_1)F_m(\phi_2)\\ &\times R_i(a_1,a_2,\phi_1,\phi_2;C)\Big]d\phi_1\,d\phi_2\,da_2\,da_1=0, \qquad (3.33)\\ \text{for } j,k=1,2;\ \ l=1\ldots N_{\phi_1};\ \ m=1\ldots N_{\phi_2};\ \ i=3\ldots 18.\end{aligned}$$

We set the number of the Fourier terms in expansion (3.31) to be $N_{\phi_1}=N_{\phi_2}=8$. As a result, the total number of the unknown coefficients, C's, in expansion (3.31) is equal to $4,096$ for all 16 slave constraint relationships, in each element. Note that the total number of unknown quantities resulting from the finite difference discretization scheme in the whole amplitude domain is equal to $65,536$. Thus, it is seen that the computational cost is tremendously reduced for the nonlinear solver, since the invariant manifold, defined by equation (3.29), is now solved for in each four-dimensional discretized element.

The initial values used in the numerical solution of the C's for each discretized element are determined as follows. For the first element, which has a two-dimensional amplitude domain given by,

$$\{(a_1,a_2)\mid a_1\in[0.01,0.1157],a_2\in[0.01,0.06571]\},$$

zeros are good initial values due to the fact that the nonlinearities are weak near the origin. Then, for subsequent elements, which have incremental values in the a_1 or a_2 directions, the expansion coefficients obtained from the preceding element are used as the initial values. Once the results for all discretized elements are obtained, the expansion coefficients from contiguous elements are averaged at their interface. The resulting solution for the invariant manifold is stitched together to cover the entire domain of interest. With the obtained invariant manifold, the reference model with 36 states can be reduced to a 4-state model for this internally resonant case.

A cross section of the invariant manifold is shown in figure 3.7. The slave constraint relationship for the third transverse deflection mode, P_3 in equation (3.29), is depicted at the phase angles $(\phi_1, \phi_2) = (0, 0)$. The amplitude domain, $a_1 \in [0.01, 0.75]$ and $a_2 \in [0.01, 0.4]$, is evenly divided into 7-by-7 patches, and the invariant manifold appears smooth with this mesh. Note that the invariant manifold defined in equation (3.29) is the ensemble of the displacement and velocity constraint relationships for all 16 slave coordinates, and Figure 3.7 represents simply the cross section of one slave coordinate among the 16.

Time responses for the displacements of the master and slave coordinates are shown and compared in figures 3.8 and 3.9 using three different simulation approaches: (i) direct time simulations based on the 36-state reference model, with initial conditions that satisfy the constraint relationships; (ii) time simulations for the master coordinates using the 4-state reduced-order model, along with the reconstruction of the slave coordinate responses using the constraint functions; and (iii) simulations based on the reduced-order model obtained by the asymptotic expansion method described in Pesheck *et al.* [56], wherein the invariant manifold and the corresponding reduced-order model were generated using asymptotic series expansions. It is seen that simulations obtained from the reduced-order model match the reference model results precisely, while the results from the asymptotic method depart from the reference response rather quickly as time progresses. This is not surprising, because the combination orders of the multi-dimensional polynomials used in the asymptotic expansion method are limited to three [56]. Here, the combination order of the trigonometric functions in equation (3.31) can be as large as eight. Consequently, the invariant manifolds constructed here are more accurate than the manifolds obtained in [56], and the simulations will match more closely, especially at larger amplitudes. The better accuracy of the reduced-order model can also be verified by observing simulations of the transverse displacement of the tip of the beam, as shown in figure 3.10.

In figures 3.8–3.10, the accuracy of the reduced-order model has been verified by comparisons of the simulated time responses. The 4-state reduced-order model can then be utilized to investigate the dynamic behavior of this system, which arises from the existence of the internal resonance. Amplitude modulation of the responses for the two master coordinates, $a_1(t)$ and $a_2(t)$. is demonstrated in figure 3.11, Note that there exists a continuous exchange of energy between the two modes. Within the first second, the time period of the energy exchange can be approximately determined as 0.12 second. Similar properties can also be found in figure 3.12, where motions are simulated over a long time period. The energy exchange shown in figure 3.12 occurs at a much slower time scale, with a period of about 9 seconds.

3.5 Conclusions

The following conclusions can be drawn from this study: (i) Multi-NNMs can be effectively generated by the invariant manifold approach. A systematic solution methodology for the invariant manifold has been proposed, which uses the polar form of the master coordinates. Four-dimensional invariant manifolds have been successfully constructed for the 3-DOF example system and for the rotating beam system, using a combination of finite difference or finite element discretization schemes in the amplitude domain and two-dimensional Fourier series expansions in the phase domain. (ii) A reduced-order model can be generated once the multi-NNM is obtained, and motions on the invariant manifold can be accurately captured by this model. The precision of the reduced-order model is controlled by the numerical parameters used in the solution procedure. (iii) Although only quadratic and cubic order nonlinear forces were considered in the systems considered, the construction method can be extended to systems with more complicated nonlinear forces, and this is relatively straightforward if the nonlinear forces do not depend on velocities. Otherwise, the numerical solution algorithm will need to simultaneously solve for the displacement (P_i) and velocity (Q_i) constraint functions, which will involve many more unknown coefficients. (iv) For complicated dynamic systems, such as more realistic rotating blade models that include lead-lag and torsional motions, gyroscopic effects and damping forces must be considered in the linear order model. The multi-mode invariant manifold approach can be extended to such systems. However, complex linear modal analysis must be used to obtain a revised form of the master and slave coordinates [55].

3.6 Figures

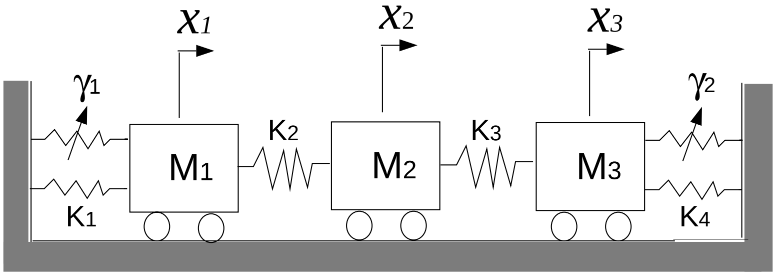

Figure 3.1: Schematic diagram of the mass–spring system: masses $M_1 = M_2 = M_3 = 1$ kg; spring stiffnesses $K_1 = 0.5$ N/m, $K_2 = 5$ N/m, $K_3 = 2.03$ N/m, $K_4 = 0.6$ N/m; nonlinear spring forces $\gamma_1 = 1.0 \times X_1(t)^3$ N, $\gamma_2 = 1.5 \times X_3(t)^3$ N. X_1, X_2, and X_3 denote the displacements of masses M_1, M_2, and M_3 respectively.

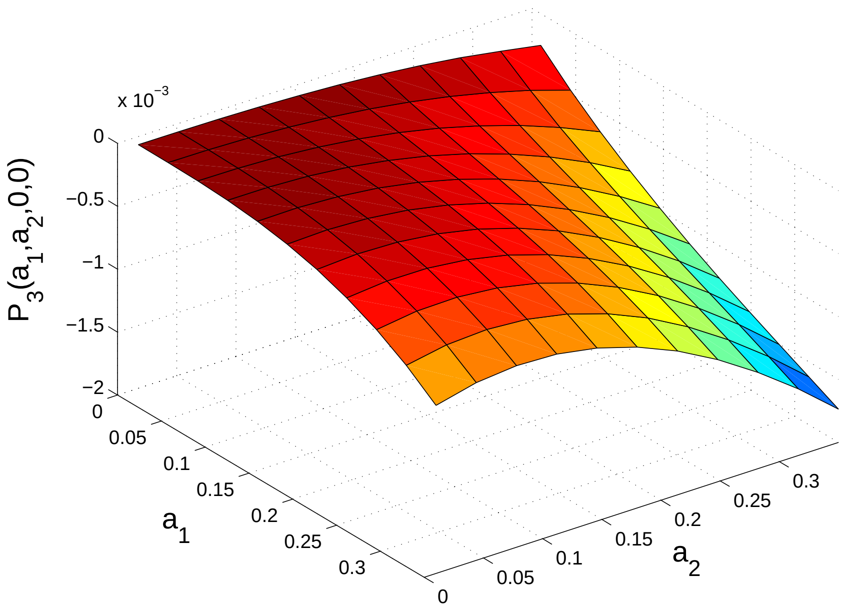

Figure 3.2: A section of one component of the invariant manifold for the system shown in figure 3.1. The modal displacement η_3 is shown at phase angles $(\phi_1, \phi_2) = (0, 0)$.

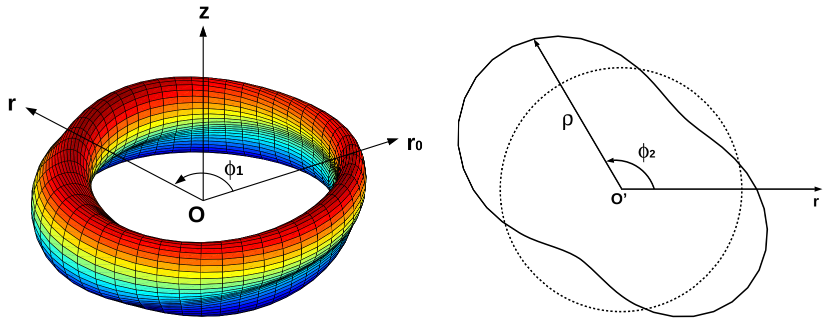

(a) (b)

Figure 3.3: Diagram of another section of a component of the invariant manifold for the system shown in figure 3.1. The modal displacement η_3 is shown at amplitude $(a_1, a_2) = (0.35,\ 0.35)$. (a) an illustration for the invariant manifold defined in the torus domain $\{\ (\phi_1, \phi_2) \mid \phi_1 \in [0, 2\pi],\ \phi_2 \in [0, 2\pi]\ \}$; (b) a cross sectional view of the invariant manifold at phase angle $\phi_1 = 2/3\,\pi$.

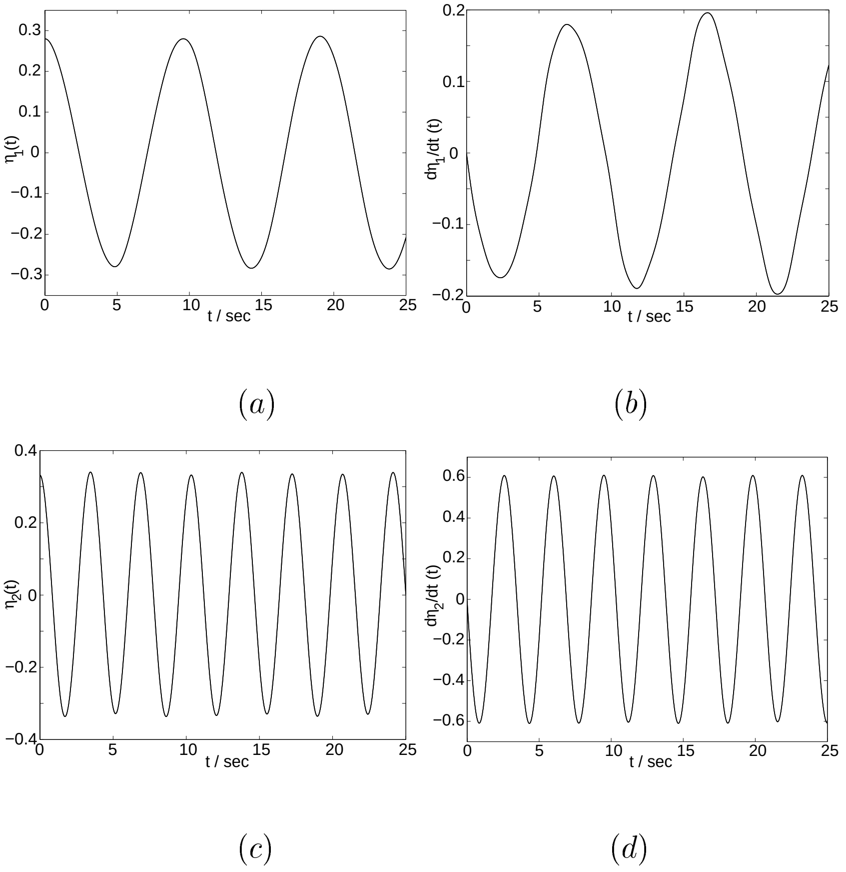

(a) (b)

(c) (d)

Figure 3.4: Comparison of the time responses of the master coordinates for the system shown in figure 3.1, for initial conditions $a_1(0) = 0.28$, $\phi_1(0) = 0.0$, $a_2(0) = 0.28$, $\phi_2(0) = 0.0$: (—) time simulation of the original system model; (- - -) simulation of the reduced-order model. Plot (a) shows the time response of η_1 versus t; (b) $\dot{\eta}_1(t)$; (c) $\eta_2(t)$; (d) $\dot{\eta}_2(t)$.

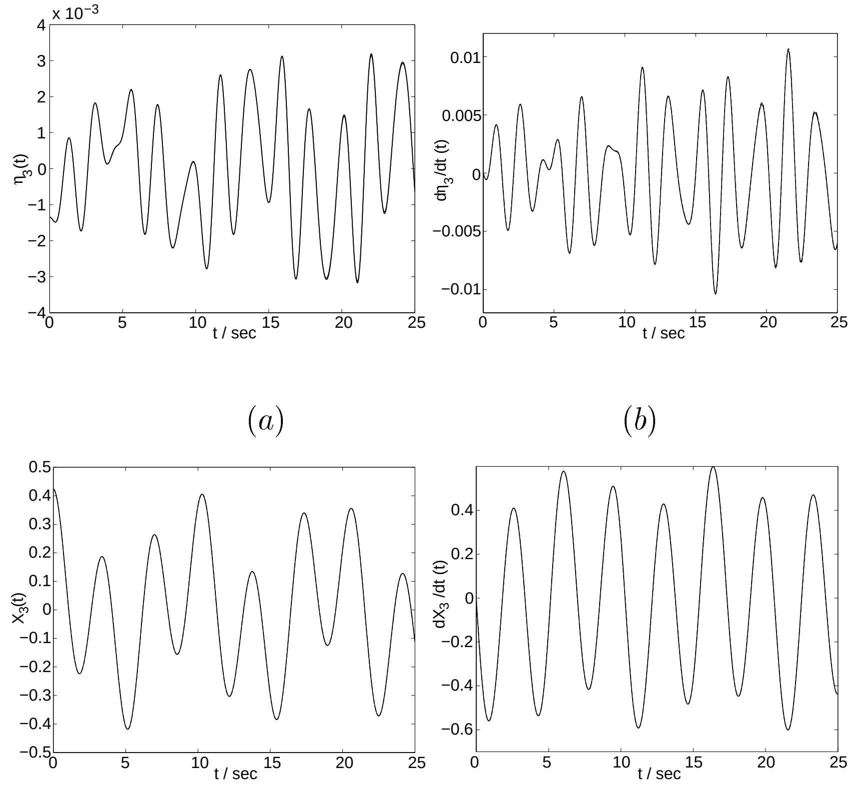

(a) (b)

(c) (d)

Figure 3.5: Comparison of the time responses of the slave coordinates and mass M_3 for the system shown in figure 3.1, for initial conditions deduced from the initial values of the master coordinates $a_1(0) = 0.28$, $\phi_1(0) = 0.0$, $a_2(0) = 0.28$, $\phi_2(0) = 0.0$: (—) time simulation of the original system model; (- - -) simulation based on the reduced-order model. Plot (a) shows the time response of η_3 versus t; (b) $\dot{\eta}_3(t)$; (c) $X_3(t)$; (d) $\dot{X}_3(t)$.

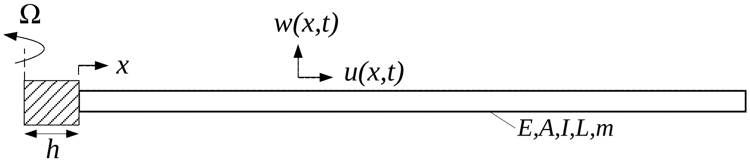

Figure 3.6: Schematic diagram of the rotating beam system. Rotating speed Ω is constant. The uniform beam has the following material and geometrical parameters: Young's modulus E, cross sectional area A, second moment of cross sectional area I, length L, and mass per unit length m. The hub radius is h. (Abridged from reference [56].)

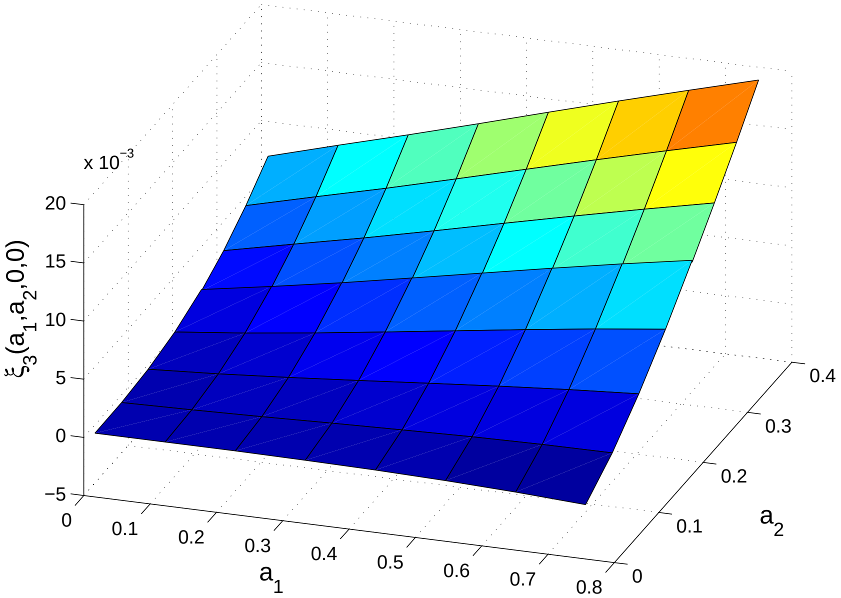

Figure 3.7: A section of one component of the invariant manifold for the system shown in figure 3.6. The displacement constraint relationship for the third transverse deflection mode, ξ_3, is shown at phase angle $(\phi_1, \phi_2) = (0, 0)$.

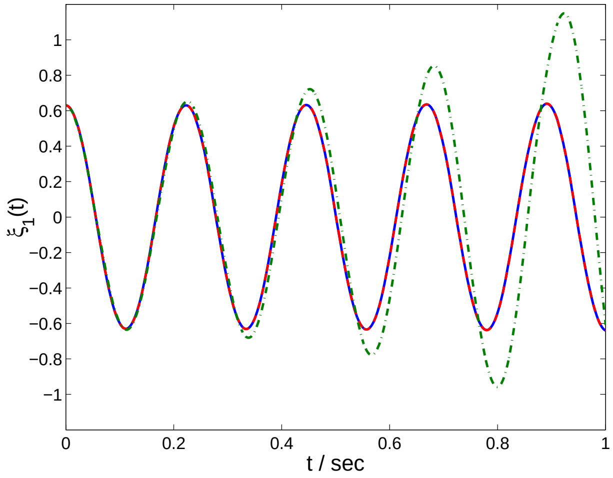

(a)

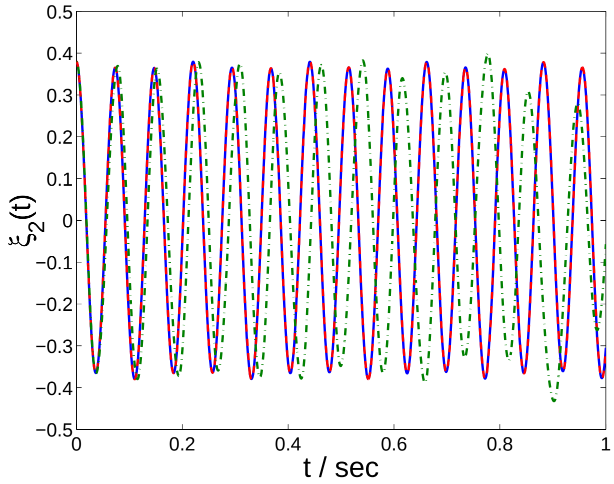

(b)

Figure 3.8: Comparison of the time histories of the master coordinates $\xi_1(t)$ and $\xi_2(t)$ for the system shown in figure 3.6, with initial conditions $a_1(0) = 0.63$, $\phi_1(0) = 0.0$, $a_2(0) = 0.38$, $\phi_2(0) = 0.0$. (—) time simulation of the full reference model; (- - -) simulation of the reduced-order model; $(- \cdot - \cdot -)$ results from the asymptotic expansion method. Plot (a) shows the first transverse modal displacement, $\xi_1(t)$; (b) second transverse modal displacement $\xi_2(t)$.

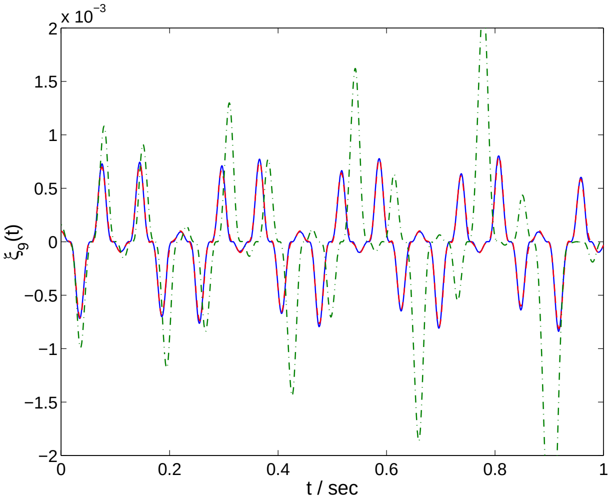

(a)

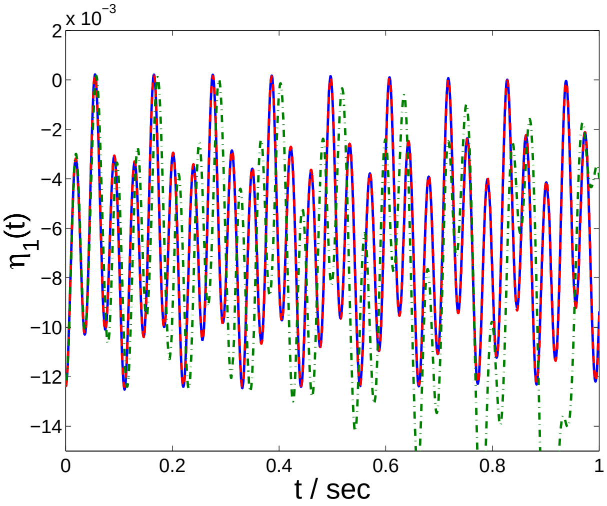

(b)

Figure 3.9: Time histories of the slave coordinates $\xi_9(t)$ and $\eta_3(t)$ for the system shown in figure 3.6, for initial conditions deduced from the initial values of the master coordinates $a_1(0) = 0.63$, $\phi_1(0) = 0.0$, $a_2(0) = 0.38$, $\phi_2(0) = 0.0$. (—) time simulation of the full reference model; (- - -) simulation of the reduced-order model; ($- \cdot - \cdot -$) results from the asymptotic expansion method. Plot (a) shows the ninth transverse modal displacement, $\xi_9(t)$; (b) first axial modal displacement $\eta_1(t)$.

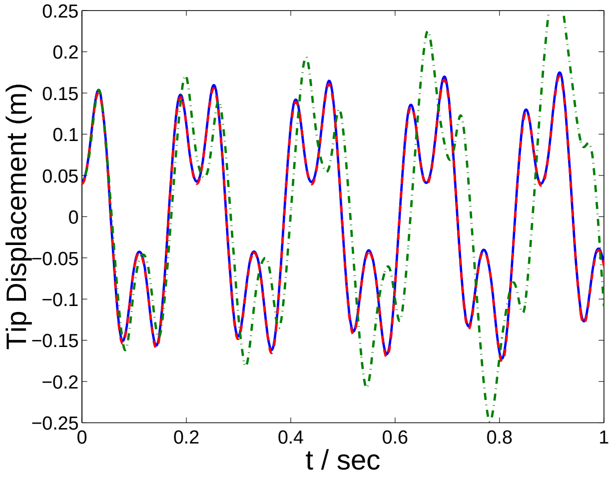

Figure 3.10: Time history of the transverse displacement at the tip of the beam for the system shown in figure 3.6, for initial conditions deduced from the initial values of the master coordinates $a_1(0) = 0.63$, $\phi_1(0) = 0.0$, $a_2(0) = 0.38$, $\phi_2(0) = 0.0$. (—) time simulation of the reference model; (- - -) simulation of the reduced-order model; $(- \cdot - \cdot -)$ results from the asymptotic expansion method.

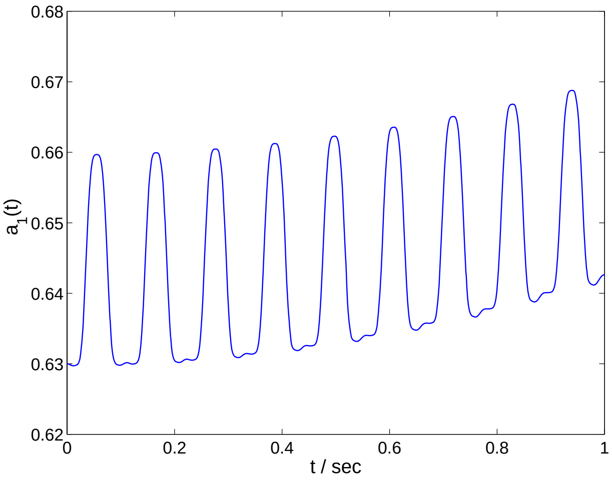

(a)

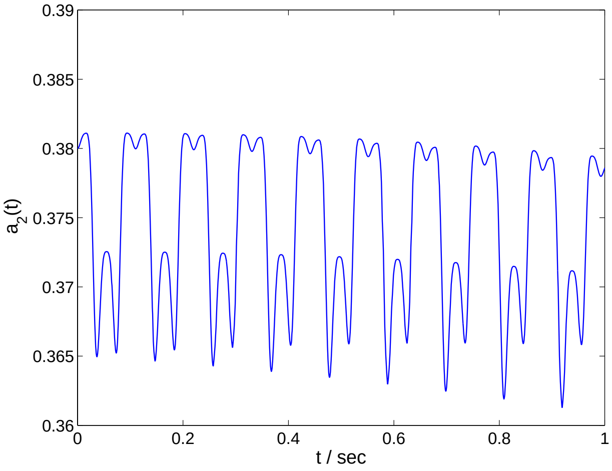

(b)

Figure 3.11: Time histories of the master coordinates $a_1(t)$ and $a_2(t)$ for system shown in figure 3.6 for 1 second, under initial conditions $a_1(0) = 0.63$, $\phi_1(0) = 0.0$, $a_2(0) = 0.38$, $\phi_2(0) = 0.0$. Plot (a) shows the amplitude of the first transverse modal displacement, $a_1(t)$; (b) amplitude of the second transverse modal displacement $a_2(t)$.

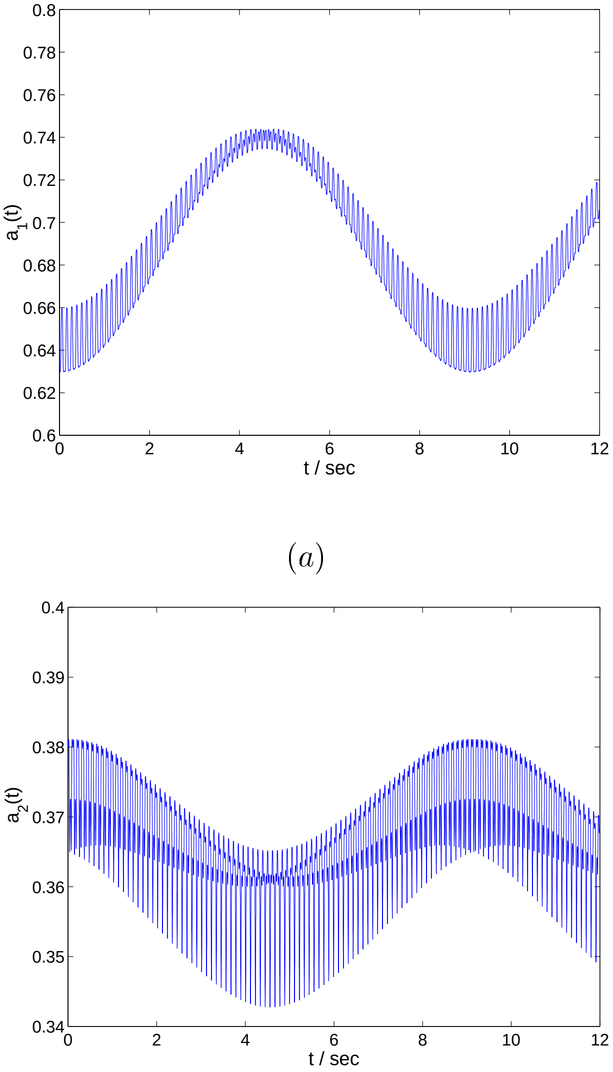

(a)

(b)

Figure 3.12: Time histories of the master coordinates $a_1(t)$ and $a_2(t)$ for the system shown in figure 3.6 for 12 seconds, under initial conditions $a_1(0) = 0.63$, $\phi_1(0) = 0.0$, $a_2(0) = 0.38$, $\phi_2(0) = 0.0$. Plot (a) shows the amplitude of the first transverse modal displacement, $a_1(t)$; (b) amplitude of the second transverse modal displacement $a_2(t)$.

CHAPTER IV

NONLINEAR NORMAL MODES FOR VIBRATORY SYSTEMS UNDER PERIODIC EXCITATION

4.1 Introduction

Many techniques exist for determining the response of nonlinear systems that are subjected to periodic excitation. In addition to brute-force simulations, there are a variety of approximate analytical methods, such as the method of multiple scales, harmonic balance, and averaging. When the system is responding in a periodic manner, it is behaving like a low order system, and the question arises as to whether or not a reduced order model can be found that captures the system response. In fact, the above analytical techniques do precisely this, by imposing various types of approximations.

For free vibration problems one uses system modes to construct reduced order models, and these techniques have been well developed for both linear and nonlinear systems [24, 25]. One such technique, introduced by Shaw and Pierre [1–3], defines the normal mode of a nonlinear oscillatory system in terms of invariant manifolds in the phase space that are tangent to the linear (eigen-)modes at the equilibrium point. In such a formulation, a *master* mode is selected (the mode of interest), and the normal mode is constructed by a formulation in which the remaining linear modes of the system, i.e., the *slave* modes, depend on the master mode. This dependence defines the invariant manifold for the nonlinear normal mode. The construction of the nonlinear normal mode invariant manifold is equivalent to the determination of the constraint relationships for all of the slave coordinates. Once these constraint relationships are obtained, the system dynamics can be restricted to the invariant manifold, resulting in a minimal-sized model that is in terms of only the master coordinates. By studying the dynamics of the reduced-order model, it is possible to recover the associated modal dynamics of the original nonlinear system. This model reduction approach is similar to the center manifold technique that allows one to study bifurcation problems using reduced order models of nonlinear systems [53].

Based on the invariant manifold approach, Boivin *et al.* [6] were able to construct nonlinear normal modes for weakly nonlinear systems using polynomial expansion functions to approximate the constraint relationships for the slave coordinates. The polynomial expansion has also been used by Nayfeh *et al.* [29] to construct invariant manifolds for systems with cubic nonlinearities. They found that a complex variable expression for the master coordinates is very convenient for the construction procedure. King and Vakakis [26] used an energy-based approach to compute nonlinear normal modes for a class of one-dimensional, conservative, continuous systems. They showed that under some circumstances, nonlinear normal modes cannot be constructed using physical coordinates and that a transformation to linear modal coordinates is necessary in order to define nonlinear normal modes. Vakakis and co-workers have carried out extensive investigations of nonlinear normal modes, including the consideration of stability and bifurcations [25]. Pesheck *et al.* [42] used numerical solutions of the invariant manifold equations to extend the invariant manifold approach to more general, strongly nonlinear systems. In this approach, the master coordinates were expressed in polar coordinate form, and a Galerkin-based solution technique was introduced to solve the invariant manifold equations. This methodology has been applied to a 45-degree-of-freedom rotating beam system [58] over a strongly nonlinear amplitude range in which significant coupling occurs between the linear modes, due to strong nonlinear effects. The invariant manifold based approach has also proved effective for systems with non-smooth characteristics (Jiang *et al.* [54]), and for gyroscopic and damped systems (Legrand *et al.* [55]).

In order to apply the invariant manifold-based model reduction method to nonlinear systems with harmonic excitation, Shaw *et al.* [59] introduced a new variable to represent the time-varying term, which is governed by a second-order differential equation. With this new variable, the invariant manifold-based approach can be extended to systems subjected to periodic excitation. Similarly, Agnes and Inman [60] treated forcing as an additional degree of freedom and applied the multiple scales method to solve for the nonlinear normal modes of a two-degree-of-freedom example system. Since the multiple scales method is based on perturbation ideas, their results are valid in the weakly nonlinear amplitude range. In the present study, model reduction of nonlinear systems under harmonic excitation is carried out by the inclusion of one additional dynamic state variable, the phase of the harmonic excitation, as a master coordinate in the invariant manifold. The constraint relationships for the slave coordinates are then defined in the augmented space, and they depend on the usual modal master coordinates as well as on the phase of the excitation. The resulting "forced" invariant manifold thus features one additional dimension compared to the free vibration manifold, and it can be solved for numerically over large amplitude regions using the Galerkin-based solution procedure [42]. This manifold is essentially a modal manifold that varies in time with a period equal to that of the excitation. By this means, it is possible to obtain accurate reduced-order models for strongly nonlinear systems subjected to periodic excitation.

The paper is organized as follows. In section 4.2, the class of nonlinear systems to be considered is defined, the invariant manifold formulation is reviewed, and the partial differential equations governing the invariant manifold are derived. In section 4.3, the Galerkin-based solution methodology is introduced and applied to the forced response of a simple two-degree-of-freedom system. The methodology is then applied to a more complicated system, a 12-degree-of-freedom beam model, in section 4.4, to further demonstrate the power and utility of the technique. Finally, some conclusions are drawn in section 4.5.

4.2 The invariant manifold approach

We consider an N-degree of freedom (DOF) nonlinear vibratory system wherein the nonlinearities depend only on displacements. In this case, a transformation of the equations of motion to linear modal coordinates yields the

$$\ddot{\eta}_i + 2\xi_i\omega_i\dot{\eta}_i + \omega_i^2\eta_i = A_i(\eta_j) + f_i\cos\phi_f, \quad i, j = 1\,, \dots\,,\ n \tag{4.1}$$

where η_i is the i-th linear modal coordinate and ω_i is the corresponding natural frequency of free vibrations of the associated linerized system. Damping is assumed to be small, and thus linear proportional damping can be employed, represented by the linear modal damping ratios, ξ_i. The nonlinear forces in the system (4.1) are included in the terms $A_i(\eta_j)$, which couple the linear modes to one another. In order to simplify the construction for the invariant manifold, the nonlinear forces, A_i, have been assumed to be independent of the linear modal velocities, $\dot{\eta}_j$. (This can be relaxed, but the solution is more cumbersome.) The external harmonic excitation has been projected onto the i-th linear modal coordinate, and is thus represented by the term $f_i\cos\phi_f$, where f_i is the linear modal force amplitude, and the phase, ϕ_f, has the form: $\phi_f = \omega_f t + \phi_{f0}$, where ω_f is the excitation frequency, and ϕ_{f0} is an initial phase angle. Note that in some applications (e.g., parametric excitation), f_i may depend on the modal coordinates, and this could be easily incorporated in the present formulation. Also, gyroscopic effects are not included in the formulation (4.1); again, this could be relaxed, but would complicate the solution procedure. Finally, it is assumed that the linear modal frequencies, ω_i, are not commensurable; this is a necessary restriction for the present formulation, since otherwise the nonlinear system response cannot be reduced to a single mode.

In order to obtain the reduced-order model for system (4.1), an extension of the invariant manifold approach [42, 58] is used. Consider the following $(2N+1)$-state augmented system:

$$\begin{cases} y_i = \dot{\eta}_i \\ \dot{y}_i + 2\xi_i\omega_i y_i + \omega_i^2\eta_i = A_i(\eta_j) + f_i\cos\phi_f \quad , \quad i,j = 1\ \ldots\ n \\ \dot{\phi}_f = \omega_f \end{cases} \tag{4.2}$$

where the state variables y_i are introduced as the modal velocities, and the phase variable ϕ_f is considered as an additional state, corresponding to an oscillatory degree of freedom with constant amplitude. By this means, the phase variable, ϕ_f, which represents the dynamics of the excitation, can be included in the expressions for the invariant manifold. As a result, the reduced-order model based on the invariant manifold can capture the dynamic behavior of system (4.1) with periodic excitation. This approach is analogous to bifurcation analyses using center manifolds, wherein the bifurcation parameter is deemed as the augmented variable, using the so-called “suspension trick” [53].

The next step is to divide the N pairs of state variables in system (4.2), $(\eta_i,\ y_i)\ \ i \in [1, n]$, into two separate groups, denoted as the *master* coordinates and the *slave* coordinates. The *master* coordinates, $(\eta_k,\ y_k)\ \ k \in S_M$, are the modal coordinates (in state variable form) that are to be kept in the final reduced-order model, where S_M is the set of indices that includes the master modes. The *slave* coordinates, $(\eta_i,\ y_i)\ \ i \notin S_M$, are all the remaining modal degrees of freedom, which are taken to depend on the master coordinates in a manner that satisfies the equations of motion. In this paper, we focus on the case where a single pair of state variables, whose modal frequency ω_k is close to the excitation frequency ω_f, are retained as the master coordinates. These master coordinates are supplemented by the forcing phase, ϕ_f, which also plays the role of a master coordinate. Thus, our investigation is limited to the primary resonance of a nonlinear system under harmonic excitation. Investigating super- or sub-resonances, or nonlinear systems with internal resonances, requires the selection of multiple pairs of state variables as the master coordinates [29, 61].

Before deriving the partial differential equations (PDE) governing the invariant manifold, the master coordinates, $(\eta_k,\ y_k)$, are transformed to polar coordinates, as follows:

$$\begin{cases} \eta_k = a\mathrm{cos}\phi \\ y_k = -a\omega_k\mathrm{sin}\phi \end{cases} \tag{4.3}$$

where a and ϕ are the amplitude and phase of the master coordinates, respectively, and ω_k is the k-th linear modal frequency. Substituting equation (4.3) into the differential equations governing $(\eta_k,\ \dot{\eta}_k)$ in system (4.2), yields

$$\begin{cases} \dot{a} = -2\xi_k a\omega_k\mathrm{sin}^2\phi - (A_k + f_k\mathrm{cos}\phi_f)\mathrm{sin}\phi/\omega_k \\ \dot{\phi} = \omega_k - \xi_k\omega_k\mathrm{sin}2\phi - (A_k + f_k\mathrm{cos}\phi_f)\mathrm{cos}\phi/(a\omega_k) \\ \dot{\phi}_f = \omega_f \end{cases} \tag{4.4}$$

In equation (4.4), the nonlinear force term, A_k, depends on all the linear modal coordinates, $\eta_j\ \ j \in [1, n]$, in system (4.2). In order to obtain the reduced-order model governing only on the master coordinates, a, ϕ, and ϕ_f, in the form of equation (4.4), the slave coordinates are assumed to depend on the master coordinates in the following form:

$$\begin{cases} \eta_i = P_i(a, \phi, \phi_f) \\ \qquad\qquad\qquad\qquad \text{for } \ i = 1\ \ldots\ n,\ \ i \neq k \\ \dot{\eta}_i = Q_i(a, \phi, \phi_f) \end{cases} \tag{4.5}$$

where the $(n-1)$ pairs of P_i's and Q_i's are the constraint relationships that represent the invariant manifold. The solution procedure for the P_i's and Q_i's follows the usual invariant manifold formulation.

Substituting expression (4.5) into system (4.2), yields

$$\begin{cases} \frac{\partial P_i}{\partial a}\dot{a} + \frac{\partial P_i}{\partial \phi}\dot{\phi} + \frac{\partial P_i}{\partial \phi_f}\dot{\phi}_f = Q_i \\ \\ \frac{\partial Q_i}{\partial a}\dot{a} + \frac{\partial Q_i}{\partial \phi}\dot{\phi} + \frac{\partial Q_i}{\partial \phi_f}\dot{\phi}_f + 2\xi_i\omega_i Q_i + \omega_i^2 P_i = A_i + f_i \cos\phi_f \end{cases} \tag{4.6}$$

$$\text{for } i = 1 \ \ldots \ n, \ \ i \neq k$$

Then, combining equation (4.4) and equation (4.6), the PDE's governing the invariant manifold are obtained. These are given by:

$$\begin{cases} Q_i = \frac{\partial P_i}{\partial a}\left[-2\xi_k a\omega_k \sin^2\phi - (A_k + f_k\cos\phi_f)\sin\phi/\omega_k\right] \\ \quad + \frac{\partial P_i}{\partial \phi}\left[\omega_k - \xi_k\omega_k \sin 2\phi - (A_k + f_k\cos\phi_f)\cos\phi/(a\omega_k)\right] \\ \quad + \frac{\partial P_i}{\partial \phi_f}\omega_f \\ \\ -2\xi_i\omega_i Q_i - \omega_i^2 P_i + A_i + f_i\cos\phi_f = \\ \quad \frac{\partial Q_i}{\partial a}\left[-2\xi_k a\omega_k \sin^2\phi - (A_k + f_k\cos\phi_f)\sin\phi/\omega_k\right] \\ \quad + \frac{\partial Q_i}{\partial \phi}\left[\omega_k - \xi_k\omega_k \sin 2\phi - (A_k + f_k\cos\phi_f)\cos\phi/(a\omega_k)\right] \\ \quad + \frac{\partial Q_i}{\partial \phi_f}\omega_f \end{cases} \tag{4.7}$$

$$\text{for } i = 1 \ \ldots \ n, \ \ i \neq k$$

Once equation (4.7) has been solved, the constraint relationships for the slave coordinates, the P_i's and Q_i's, are known and can be substituted into equation (4.4). The result is the desired reduced-order model, which has dynamic variables a, ϕ, and ϕ_f. The forced dynamics of the full system near the primary resonance are captured by this model, which is a single-DOF system with periodic excitation. It is interesting to note that parametric excitation terms are introduced during this process, in that the nonlinear force, A_k, now depends on the phase of the excitation, ϕ_f. Obviously, the governing equations for the invariant manifold, equation (4.7), are inherently nonlinear, and are not analytically tractable.

Compared with the invariant manifold approach in the free vibration case [42], the additional phase variable, ϕ_f, is included in the present model to account for the harmonic excitation. Consequently, the invariant manifold, defined by equation (4.5), is three-dimensional (or, equivalently, two-dimensional and moving in a time-periodic manner). The numerical construction procedure for the invariant manifold is therefore more complicated than that for the free oscillation case, where the manifold is two-dimensional. However, some useful properties can be utilized to alleviate the computational effort required in the solution process. First, in expression (4.5), the constraint relationships for the modal velocities, the Q_i's, are the time derivative of the corresponding position constraints, the P_i's. Hence, it is possible to eliminate the Q_i's from the unknowns during the numerical solution procedure, and deduce them from the solution of the P_i's. Another useful property is attributed to the polar form of the master coordinates, defined in equation (4.3). By this means, the three-dimensional space on which the invariant manifold is defined can be divided into a one-dimensional amplitude region, a, and a two-dimensional phase region, $(\phi,\ \phi_f)$. For the two-dimensional phase region, a two-dimensional Fourier series is the natural choice for the expansion functions in the Galerkin-based solution procedure. As a result, Fast Fourier Transforms can be applied to carry out the conversion between the values at the discretized points in the two-dimensional phase region and their Fourier coefficients in an efficient manner. These two simplifications are employed to construct the invariant manifolds for the two example systems.

4.3 A two-DOF mass-spring system

The first example presented is quite simple; it is used simply to demonstrate the steps in the process. The two-DOF mass-spring system under consideration is shown in figure 4.1. The equations of motion for the system are:

$$\begin{cases} m_1\ddot{x}_1 + k_1x_1 + \beta_1x_1^3 + k_2(x_1 - x_2) = f\cos\omega_f t \\ m_2\ddot{x}_2 + k_2x_2 - k_2x_1 + k_3x_2 + \beta_2x_2^3 = 0 \end{cases} \tag{4.8}$$

where m_1=1.0 kg, m_2=1.5 kg, k_1=2.0 N/m, k_2=3.5 N/m, k_3=5.0 N/m, β_1=β_2=1.0 N/m^3, and f=1.0 N. The excitation frequency ω_f varies within a certain range, and the invariant manifold is solved for at each frequency over that range.

The physical displacement coordinates, $\{x_1,\ x_2\}^T$, are first transformed to modal coordinates, $\{\eta_1,\ \eta_2\}^T$, as follows:

$$\begin{Bmatrix} x_1 \\ x_2 \end{Bmatrix} = \begin{bmatrix} 0.7173 & 0.6967 \\ 0.5689 & -0.5857 \end{bmatrix} \begin{Bmatrix} \eta_1 \\ \eta_2 \end{Bmatrix} \tag{4.9}$$

As a result, system (4.8) is transformed to the following standard form:

$$\begin{cases} \ddot{\eta}_1 + 2\xi_1\omega_1\dot{\eta}_1 + \omega_1^2\eta_1 = A_1 + f_1\cos\omega_f t \\ \ddot{\eta}_2 + 2\xi_2\omega_2\dot{\eta}_2 + \omega_2^2\eta_2 = A_2 + f_2\cos\omega_f t \end{cases} \tag{4.10}$$

where linear modal damping has been added to the system with damping ratios ξ_1=ξ_2=0.2. The two linear modal frequencies are ω_1=1.6506 rad/s, and ω_2=2.9056 rad/s. Projecting the external excitation onto the modal coordinates yields f_1=0.1435 and f_2=0.1393, and the cubic nonlinear forces, A_1 and A_2, are given by:

$$\begin{cases} A_1 = -0.7173(0.7173\eta_1 + 0.6962\eta_2)^3 \\ \qquad\quad - 0.5689(0.5689\eta_1 - 0.5857\eta_2)^3 \\ A_2 = -0.6967(0.7173\eta_1 + 0.6962\eta_2)^3 \\ \qquad\quad + 0.5857(0.5689\eta_1 - 0.5857\eta_2)^3. \end{cases} \tag{4.11}$$

In order to obtain the reduced-order model for system (4.10), the master coordinate, which is kept in the reduced-order model, must be specified. We first consider the primary resonance near the first linear mode, which occurs when the excitation frequency, ω_f, is close to the first linear modal frequency ω_1. Then, the state variables $(\eta_1,\ y_1)$, where y_1 is defined in equation (4.2), are the natural choice for the master coordinates.

The master coordinates, $(\eta_1,\ y_1)$, are transformed to the polar form defined in equation (4.3):

$$\begin{cases} \eta_1 = a\text{cos}\phi \\ y_1 = \dot{\eta}_1 = -a\omega_1\text{sin}\phi. \end{cases} \tag{4.12}$$

The constraint relationships for the slave coordinates, defined in equation (4.5), are given by:

$$\begin{cases} \eta_2 = P_2(a, \phi, \phi_f) \\ y_2 = \dot{\eta}_2 = Q_2(a, \phi, \phi_f), \end{cases} \tag{4.13}$$

and the partial differential equations governing the invariant manifold are as presented in equation (4.7).

A Galerkin-based method is utilized to numerically solve the invariant manifold equation. The three-dimensional space for which the invariant manifold is defined is spanned by one amplitude, $a \in [0, a_{max}]$, and two phases , $\phi \in [0, 2\pi]$ and $\phi_f \in [0, 2\pi]$. A two-dimensional Fourier series is the natural choice for the basis functions for the phases, while a variety of functions can be used for the amplitude expansion. It has been shown that the computational cost for the construction of the invariant manifold is significantly reduced if the amplitude domain is discretized into small segments, so that simple piecewise linear functions can be used as the basis functions for each discretized segment in the a direction [42, 58]. As a result, in any three-dimensional region,

$$\big\{(a, \phi, \phi_f) \mid a \in [a_0, a_1], \phi \in [0, 2\pi], \phi_f \in [0, 2\pi]\big\} \tag{4.14}$$

where a_0 and a_1 are the lower and upper limits of the amplitude segment, respectively, the unknown constraint relationship, P_2, can be expanded as follows:

$$P_2(a,\phi,\phi_f) = \sum_{j=1}^{2}\sum_{l=1}^{N_\phi}\sum_{m=1}^{N_{\phi f}} C_{jlm}T_j(a)F_l(\phi)F_m(\phi_f) \tag{4.15}$$

where $T_j(a)$are the piecewise linear functions defined in the amplitude segment, $a \in [a_0, a_1]$, as follows,

$$T_1(a) = \frac{a-a_0}{a_1-a_0}, \qquad T_2(a) = \frac{a_1-a}{a_1-a_0}, \tag{4.16}$$

and $F_l(\phi)$ and $F_m(\phi_f)$ are Fourier terms defined as:

$$F_l(\phi) = \begin{cases} \cos\frac{l-1}{2}\phi, & l \text{ is odd} \\ \sin\frac{l}{2}\phi, & l \text{ is even,} \end{cases} \tag{4.17}$$

and N_ϕ and N_{ϕ_f} are the number of terms of the Fourier expansions in ϕ and ϕ_f, respectively.

As mentioned in section 4.2, the constraint relationship Q_2 can be constructed from P_2. Hence, the invariant manifold in this three-dimensional region is completely determined (in this approximate form) once the unknown coefficients, the C's in expression (4.15), have been obtained. Note that each small amplitude segment has its own set of C's.

In the Galerkin-based procedure, the expansion for P_2 is substituted into the governing differential equations for the invariant manifold, equation (4.7). Then, a set of nonlinear algebraic equations governing the unknown coefficients can be explicitly obtained by requiring that the projection of the residuals of equation (4.7) onto each basis function, defined in expansion (4.15), be equal to zero. The C coefficients can then be solved for numerically using an iterative technique. The method selected here is the hybrid Powell's method, which simplifies the solution procedure in a manner such that the explicit form of the set of nonlinear algebraic equations in the C's is not necessary during the iteration process [57].

For a given set of initial values for the C's, the expression of the velocity constraint, Q_2, can be explicitly determined from the following relationship:

$$\begin{aligned}
Q_2(a,\phi,\phi_f;C) = &\sum_{j=1}^{2}\sum_{l=1}^{N_\phi}\sum_{m=1}^{N_{\phi f}} C_{jlm}\frac{dT_j}{da}(a)F_l(\phi)F_m(\phi_f)\times \\
&\left[-2\xi_1 a\omega_1 \text{sin}^2\phi - (A_1(a,\phi,\phi_f;C)+f_1\text{cos}\phi_f)\text{sin}\phi/\omega_1\right] \\
&+\sum_{j=1}^{2}\sum_{l=1}^{N_\phi}\sum_{m=1}^{N_{\phi f}} C_{jlm}T_j(a)\frac{dF_l}{d\phi}(\phi)F_m(\phi_f)\times \\
&\left[\omega_1 - \xi_1\omega_1\text{sin}2\phi - (A_1(a,\phi,\phi_f;C)+f_1\text{cos}\phi_f)\text{cos}\phi/(a\omega_1)\right] \\
&+\sum_{j=1}^{2}\sum_{l=1}^{N_\phi}\sum_{m=1}^{N_{\phi f}} C_{jlm}T_j(a)F_l(\phi)\frac{dF_m}{d\phi_f}(\phi_f)\omega_f, \qquad (4.18)
\end{aligned}$$

which is the algebraic form of one of the differential equations governing the invariant manifold, namely the first equation in system (4.7). It should be noted that the nonlinear force, A_1, in equation (4.18) is only dependent on the C's, since all the nonlinear forces are independent of velocities in system (4.8). Otherwise, the relationship for Q_2 would be implicit. The velocity constraint, Q_2, would then have to be expanded in a similar manner as P_2 in expression (4.15), and the unknown coefficients for Q_2 would need to be solved for simultaneously with the C's, in an iterative manner.

Equation (4.18) is one of the differential equations governing the invariant manifold. The other partial differential equation is the second equation in system (4.7), and it is given by:

$$\begin{aligned}
&-2\xi_2\omega_2 Q_2(a,\phi,\phi_f;C) - \omega_2^2 P_2(a,\phi,\phi_f;C) + A_2(a,\phi,\phi_f;C) \\
&+ f_2\text{cos}\phi_f \;=\; \frac{\partial Q_2}{\partial a}(a,\phi,\phi_f;C)\Bigg[-2\xi_1 a\omega_1\text{sin}^2\phi \\
&-(A_1(a,\phi,\phi_f;C)+f_1\text{cos}\phi_f)\frac{\text{sin}\phi}{\omega_1}\Bigg] + \frac{\partial Q_2}{\partial \phi}(a,\phi,\phi_f;C) \\
&\times\left[\omega_1 - \xi_1\omega_1\text{sin}2\phi - (A_1(a,\phi,\phi_f;C)+f_1\text{cos}\phi_f)\frac{\text{cos}\phi}{a\omega_1}\right] \\
&+\omega_f\frac{\partial Q_2}{\partial\phi_f}(a,\phi,\phi_f;C) \qquad (4.19)
\end{aligned}$$

Once we have a method to determine the derivatives, $\partial Q_2/\partial a$, $\partial Q_2/\partial \phi$, and $\partial Q_2/\partial \phi_f$, equation (4.19) can be evaluated numerically.

The derivative along the a direction, $\partial Q_2/\partial a$, can be accurately determined using a finite difference scheme, since the three-dimensional domain given in equation (4.14) can be taken to be arbitrarily small in the a direction during the discretization. Furthermore, the discrete grid points in a are selected as Gaussian quadrature points for polynomials. Since piecewise linear functions are used as the basis functions for a, the highest possible polynomial order is three in equation (4.18). Thus, a three-point Gaussian quadrature formula is sufficient in the region $a \in [a_0, a_1]$, considering the inner product between the residue of equation (4.19) and the basis functions defined in equation (4.15).

The derivatives along the ϕ and ϕ_f directions, $\partial Q_2/\partial \phi$ and $\partial Q_2/\partial \phi_f$, are determined by means of a two-dimensional Fast Fourier Transform. At any Gaussian quadrature point $a = a^*$, the expression for Q_2 is expanded as follows:

$$Q_2(a^*, \phi, \phi_f) = \sum_{m=\frac{-N_\phi}{2}}^{\frac{N_\phi}{2}} \sum_{n=\frac{-N_{\phi_f}}{2}}^{\frac{N_{\phi_f}}{2}} D_{mn}\, e^{im\phi}\, e^{in\phi_f} \tag{4.20}$$

where $i = \sqrt{-1}$, and N_ϕ and N_{ϕ_f} are set to be even. The complex Fourier coefficients, D_{mn}, are efficiently obtained by taking the Fast Fourier Transform at the grid points for Q_2, which is evaluated using equation (4.18):

$$Q_2(a^*, \bar{\phi}^I, \bar{\phi}_f^J) \quad \text{where} \begin{cases} \bar{\phi}^I = \frac{I\pi}{N_\phi} \\ \bar{\phi}_f^J = \frac{J\pi}{N_{\phi_f}} \end{cases}$$
$$\text{for} \quad I = 1 \ \ldots \ 2N_\phi, \quad J = 1 \ \ldots \ 2N_{\phi_f}$$

Note that $2N_\phi \times 2N_{\phi_f}$ grid points are used to evaluate the $N_\phi \times N_{\phi_f}$ complex Fourier coefficients in equation (4.20), in order to reduce aliasing errors in the Fourier transform. Once the complex Fourier coefficients, D_{mn}, are obtained, the determination of the derivatives, $\partial Q_2/\partial\phi$ and $\partial Q_2/\partial\phi_f$, is trivial by using the inverse Fourier transform, along with the manipulation of the complex Fourier coefficients.

The final step is to project the residue of equation (4.19) onto each basis function defined in expansion (4.15), shown as follows:

$$\begin{aligned}\int_{a_0}^{a_1}\int_0^{2\pi}\int_0^{2\pi}\Big[&T_j(a)F_l(\phi)F_m(\phi_f)\\ &\times Res(a,\phi,\phi_f;C)\Big]\,\mathrm{d}\phi\,\mathrm{d}\phi_f\,\mathrm{d}a = 0 \qquad (4.21)\\ \text{for }\ j = 1,2;\quad l = 1\ldots N_\phi;&\quad m = 1\ldots N_{\phi_f}\end{aligned}$$

where, $Res(a,\phi,\phi_f;C)$ represents the residue of equation (4.19). The solution for the invariant manifold is thus obtained by requiring the $2\times N_\phi\times N_{\phi_f}$ inner products between the residue and the basis functions to be all zero. Numerical integration for the projections can be efficiently carried out, since the numerical values of the residue are evaluated only at Gaussian quadrature points. In practice, we employ hybrid Powell's method [57], imbedded in the numerical package NAG, to search for the solution from the initial guess.

Once the solution for the C's is obtained, the original system (4.10) can be reduced to two first-order ordinary differential equations with time periodic coefficients that govern the master coordinates, as described in equation (4.4). As a result, the periodic responses of the original system can be captured using the reduced-order model.

As a specific example, we set the excitation frequency, ω_f=1.93 rad/s, and construct the three-dimensional invariant manifold. The result is depicted in figure 4.2 using four cross-sections corresponding to equally-spaced values of the excitation phase angle, ϕ_f. Along the amplitude direction a, the overall construction domain for the invariant manifold is set as $a\in[0,3.0]$, which is evenly divided into 60 segments. For each discretized element (as defined in expression (4.14) with a_0 and a_1 as the lower and upper bounds of the amplitude segment, respectively), the number of Fourier terms in equation (4.15) are set to $N_\phi = N_{\phi_f} = 16$. The initial guess values for the C's for each discretized segment are determined as follows: For the first segment, $a \in [0, 0.05]$, the results for the C's obtained from the linearized system are good initial values due to the weak effects of nonlinearities in the small amplitude region. Then, for the subsequent segments, the expansion coefficients obtained from the proceeding segment are used as initial values, since the increments in a are quite small. Once the results for all discretized segments are obtained, the expansion coefficients from contiguous segments are averaged at their interface. As a result, the solution for the invariant manifold is stitched together to cover the entire domain of interest.

Some interesting properties of the invariant manifold can be seen in figure 4.2. First, the invariant manifold varies as the phase angle of the excitation force ϕ_f changes, and therefore as time increases. The time dependence of the manifold can be easily understood since one additional dimension corresponding to the external excitation, ϕ_f, is included in the definition of the manifold. The manifold can be thought of as a two-dimensional surface that varies periodically in time, and figure 4.2 depicts it at four different instants. Moreover, the manifold is not equal to zero as the amplitude a tends to zero, which is different from what occurs in the free oscillation cases, where the invariant manifold is tangent to the corresponding linear modal space at the static equilibrium position [2].

Time responses at the excitation frequency $\omega_f = 1.93$ rad/s can be obtained from the reduced-order model, equation (4.4). Results for two different sets of initial conditions are shown in figure 4.3 and 4.4, along with comparisons of the responses obtained from the original system model, equation (4.10). With the reduced-order model governing a and ϕ, the time response for $a(t)$ and $\phi(t)$ can be obtained for any initial conditions $(a(0),\ \phi(0))$ in the construction domain. The responses of the master and slave coordinates are then reconstructed using the polar transformation definition (4.3) and the constraint relationships (4.5), respectively. For time simulations of the original system, initial conditions are taken to be those on which the reduced-order model is initiated, that is, the constraint relations are used to determine the starting conditions for the second mode. As can be seen in figure 4.3 and 4.4, the forced response obtained from the reduced-order model precisely matches the forced response from the original system model. Note that the responses in figure 4.3 and figure 4.4 converge to different steady-state responses, as is typical in such a nonlinear system.

The variation of the steady-state response amplitude of system (4.10) in terms of frequency is shown in figure 4.5 near the first resonance frequency, ω_1. From the original system model, the frequency response is obtained by sweeping the excitation frequency, ω_f, from 1.5 rad/s to 2.2 rad/s. At each excitation frequency, the direct shooting method [62] is used to search for the initial conditions corresponding to the steady-state response. As a result, multiple steady-state solutions are found near the resonance, where one branch of the solutions is unstable. The steady-state responses can also be obtained using simulations of the reduced-order models, constructed at a series of discrete excitation frequencies within the frequency range of interest, $\omega_f \in [1.5, 2.2]$. At each sample frequency ω_f, an invariant manifold-based reduced-order model is constructed following the Galerkin-based procedure described above. As can be seen in figure 4.5, the frequency response obtained from the reduced-order models matches the exact results extremely well, and even the unstable response branch is captured by the reduced-order models. In other words, at any excitation frequency ω_f, the dynamics of the original system is captured by the invariant manifold-based reduced-order model.

The steady-state frequency response near the second linear modal frequency, ω_2, is shown in figure 4.6. In this case, the master coordinates are chosen as the second linear modal coordinates in state variable form, $(\eta_2,\ \dot{\eta}_2)$. The corresponding invariant manifolds are constructed in the same manner. Again, excellent agreement is found between the full model and the reduced-order model, as shown in figure 4.6.

We now turn to a more substantial example, where the power and utility of the technique is more fully demonstrated.

4.4 An Euler-Bernoulli beam with nonlinear spring

The invariant manifold-based model reduction approach, elaborated in section 4.3, is applied here to a more complicated example system, an Euler-Bernoulli beam attached to ground at one end by a nonlinear torsional spring. As shown in figure 4.7, the beam has the following geometric and material parameters: length $l = 1$ m, cross sectional area $A = 0.0025$ m^2, second moment of area of the cross section $I = 5.0 \times 10^{-8}$ m^4, mass density $\rho = 7860$ kg/m^3, Young's modulus $E = 2 \times 10^{11}$ N/m^2, and linear spring stiffness $k = 10^8$ N/m. The moment from the nonlinear torsional spring at $x = 0$ is given by

$$\gamma_t(t) = 5000 \left[\frac{\partial u}{\partial t}(0,t)\right]^2 + 20000 \left[\frac{\partial u}{\partial t}(0,t)\right]^3 \text{ N}$$

where $u(x,t)$ is the transverse displacement of the beam. The amplitude of the harmonic excitation at $x = l$ is taken to be $f_0 = 3 \times 10^6$ N.

The equation of motion governing $u(x,t)$ is given in weak form as follows:

$$\begin{aligned} \int_{t_1}^{t_2} \Big\{ \int_0^l & (-\rho A \ddot{u} \delta u - EI u_{,xx} \delta u_{,xx})\, dx - k u(l,t) \delta u(l,t) \\ & - \gamma_t \delta u_{,x}(0,t) + F \delta u(l,t) \Big\}\, dt = 0\,, \quad \forall \quad t_1 < t < t_2 \end{aligned} \tag{4.22}$$

where $\dot{(\ )}$ denotes the partial derivative with respect to time, and $(\ )_{,x}$ is the partial derivative with respect to x.

In order to obtain the discretized ordinary differential equations for system (4.22), the Rayleigh-Ritz method is applied, wherein the transverse displacement, $u(x,t)$, is expanded as follows:

$$u(x,t) = \sum_{i=1}^{n-2} \bar{U}_i(x)a_i(t) + \psi_{c0}(x)q_{c0}(t) + \psi_{cl}(x)q_{cl}(t). \tag{4.23}$$

The basis functions in the above expansion are of two kinds: the fixed-interface normal modes, $\bar{U}_i(x)$ (that is, the modes of free vibration of the beam clamped at $x = 0$ and pinned at $x = l$), and the static constraint modes, $\psi_{c0}(x)$ and $\psi_{cl}(x)$, obtained by imposing a unit slope at $x = 0$ and a unit deflection at $x = l$, as described below. The selection of these basis functions is motivated by the Craig-Bampton technique, which is commonly used for improved modal convergence in linear vibration problems. The fixed-interface normal modes, $\bar{U}_i(x)$, are calculated from the following boundary-value problem:

$$\begin{cases} -\rho A\bar{\omega}_i^2\bar{U}_i(x) + EI\frac{d^4\bar{U}_i(x)}{dx^4} = 0, \quad \text{for } i = 1 \ \ldots \ n-2 \\ \text{Boundary conditions:} \\ \bar{U}_i(0) = 0, \ \frac{d\bar{U}_i}{dx}(0) = 0, \ \bar{U}_i(l) = 0, \ \frac{d^2\bar{U}_i}{dx^2}(l) = 0 \end{cases} \tag{4.24}$$

where $\bar{\omega}_i$ is the i-th eigenvalue corresponding to the eigenvector $\bar{U}_i$. Note that the rotation at $x = 0$ and transverse displacement at $x = l$ are fixed in equation (4.24). These degrees of freedom are captured by the static constraint modes, which are determined by solving the following problems:

$$\begin{cases} EI\frac{d^4\psi_{c0}}{dx^4}(x) = 0 \\ \psi_{c0}(0) = 0, \ \frac{d\psi_{c0}}{dx}(0) = 1.0, \ \psi_{c0}(l) = \frac{d^2\psi_{c0}}{dx^2}(l) = 0 \end{cases} \tag{4.25}$$

and

$$\begin{cases} EI\frac{d^4\psi_{cl}}{dx^4}(x) = 0 \\ \psi_{cl}(0) = \frac{d\psi_{cl}}{dx}(0) = 0, \ \psi_{cl}(l) = 1.0, \ \frac{d^2\psi_{cl}}{dx^2}(l) = 0 \end{cases} \tag{4.26}$$

The expansion (4.23) is substituted into the weak formulation, equation (4.22), resulting in

$$\begin{aligned}
\int_{t_1}^{t_2} \Bigg\{ \int_0^l \Bigg[& - \rho A (\sum_i \bar{U}_i \ddot{a}_i + \psi_{c0} \ddot{q}_{c0} + \psi_{cl} \ddot{q}_{cl}) \times \\
& (\sum_j \bar{U}_j \delta a_j + \psi_{c0} \delta q_{c0} + \psi_{cl} \delta q_{cl}) \\
& - EI (\sum_i \bar{U}_i^{''} a_i + \psi_{c0}^{''} q_{c0} + \psi_{cl}^{''} q_{cl}) \times \\
& (\sum_j \bar{U}_j^{''} \delta a_j + \psi_{c0}^{''} \delta q_{c0} + \psi_{cl}^{''} \delta q_{cl}) \Bigg] dx \\
& - k q_{cl} \delta q_{cl} - \gamma_t (q_{c0}) \delta q_{c0} + F \delta q_{cl} \Bigg\} \, dt = 0 \, , \qquad (4.27) \\
& \quad \forall \;\; t_1 < t < t_2
\end{aligned}$$

where $(\;)'$ denotes $d(\;)/dx$. Equation (4.28) can be written in matrix form as follows:

$$\begin{bmatrix} \mathbf{I} & \mathbf{M_{aq}} \\ \mathbf{M_{aq}^T} & \mathbf{M_{qq}} \end{bmatrix} \begin{Bmatrix} \ddot{\mathbf{a}} \\ \ddot{\mathbf{q}} \end{Bmatrix} + \begin{bmatrix} \Lambda & \mathbf{0} \\ \mathbf{0} & \mathbf{K_{qq}} \end{bmatrix} \begin{Bmatrix} \mathbf{a} \\ \mathbf{q} \end{Bmatrix} = \begin{Bmatrix} \mathbf{0} \\ \mathbf{F} \end{Bmatrix} \qquad (4.28)$$

where $\mathbf{I}$ is the identity matrix, Λ is a diagonal matrix with elements $\lambda_i = \bar{\omega}_i^2$, the vectors $\mathbf{a} = [\mathbf{a_1}, \mathbf{a_2}, \ldots, \mathbf{a_{n-2}}]^\mathbf{T}$ and $\mathbf{q} = [\mathbf{q_{c0}},\ \mathbf{q_{cl}}]^\mathbf{T}$ contain the amplitudes of the basis functions in the expansion of equation (4.23), and $\mathbf{F} = [-\gamma_\mathbf{t},\ \mathbf{f_0}\mathrm{cos}\omega_\mathbf{f}\mathbf{t}]^\mathbf{T}$ is the force vector.

Linear modal analysis can be applied to the linear homogeneous part of equation (4.28), i.e., by setting $\mathbf{F} = \mathbf{0}$, as follows:

$$\left\{ -\omega_i^2 \begin{bmatrix} \mathbf{I} & \mathbf{M_{aq}} \\ \mathbf{M_{aq}^T} & \mathbf{M_{qq}} \end{bmatrix} + \begin{bmatrix} \Lambda & \mathbf{0} \\ \mathbf{0} & \mathbf{K_{qq}} \end{bmatrix} \right\} \phi_\mathbf{i} = \mathbf{0} \qquad (4.29)$$

For the i-th linear mode, the frequency and mode shape are denoted as ω_i and ϕ_i, respectively. The coordinate transformation is defined as $\mathbf{X} = \Phi\eta$ where $\mathbf{X} = [\mathbf{a^T} \;\; \mathbf{q^T}]^\mathbf{T}$, Φ is the matrix of eigenvectors $\phi_\mathbf{i}$, and η is the n-dimensional modal coordinate vector. Consequently, system (4.28) is transformed to the standard form (given in equation (4.1)):

$$\ddot{\eta}_i + 2\xi_i\omega_i\dot{\eta}_i + \omega_i^2\eta_i = A_i(\eta_j) + f_i\mathrm{cos}\omega_f t, \quad i, j = 1 \;\ldots\; n \qquad (4.30)$$

where proportional damping effects have been added with linear modal damping ratios of $\xi_i = 0.03$.

By changing the number of the fixed-interface normal modes used in expansion (4.23), the convergence of the response near the first linear modal frequency, $\omega_1 = 222.43$ rad/s, is checked for system (4.30). It is found that a 12-DOF model is needed to capture the first primary resonance accurately, including ten fixed-interface modes along with the two static constraint modes.

A single pair of state variables, (η_1, y_1), where $y_1 = \dot{\eta}_1$, in system (4.30), along with the forcing phase, ϕ_f, are chosen as the master coordinates in the construction procedure for the reduced-order model near the first primary resonance. After employing the polar coordinate transformation for the master mode, $(\eta_1, y_1) \rightarrow (a, \phi)$, the remaining slave coordinates are constrained as:

$$\eta_i = P_i(a, \phi, \phi_f), \quad y_i = \dot{\eta}_i = Q_i(a, \phi, \phi_f), \qquad i = 2 \ \ldots \ 12$$

where $\phi_f = \omega_f t$. The governing partial differential equations for the constraint relationships, equation (4.7), are solved numerically using the Galerkin-based procedure described in section 4.2 and 4.3. In order to construct the invariant manifold at each excitation frequency near the resonance, the amplitude region $a \in [0, 3.0]$ was evenly divided into 60 segments. For each discretized segment, the numbers of Fourier expansion terms were set at $N_\phi = N_{\phi_f} = 8$. From the constructed invariant manifold, the reduced-order model is obtained at each excitation frequency, as shown in equation (4.4).

The steady-state response of master coordinate η_1 is shown in figure 4.8. As can be seen, both the stable branch and the unstable branch of the response are accurately captured by the simulation based on the reduced-order model. Note that at the excitation frequency $\omega_f = 242$ rad/s, the amplitude of η_1 reaches its peak at 1.0, which is physically equivalent to a 0.3m displacement near the middle point of the one-meter-long beam. While at such a large amplitude, the assumptions for an Euler-Bernoulli beam are violated, the example clearly demonstrates the capability of accurately capturing the forced response over a strongly nonlinear amplitude range.

The transient response at the excitation frequency, $\omega_f = 242$ rad/s, is also shown in figures 4.9 and 4.10 for two different initial conditions. As can be seen, the response from the reduced-order model matches very closely that from the original system for a range of initial conditions. This demonstrates that the dynamics near the primary resonance can be very accurately captured by the invariant manifold approach. Similar results can be obtained for other resonances, by choosing master modes accordingly.

4.5 Conclusions

Based on the results obtained from the mass-spring system studied in section 4.3, and from the beam system examined in section 4.4, the following conclusions are drawn: (i) With the additional phase variable representing the external harmonic excitation, the invariant manifold approach developed for free oscillations can be extended to nonlinear vibration systems subjected to periodic excitation. (ii) Once the invariant manifold is constructed, the corresponding reduced-order model can be obtained to capture the forced dynamics of the original system. (iii) The invariant manifold can be constructed numerically using a Galerkin-based technique that employs piece-wise linear amplitude functions and Fourier series for the phase variables. Using the Fast Fourier Transform, the solution procedure is quite efficient. (iv) The domain in which the invariant manifold is defined can be taken out to large amplitudes, and is discretized into small amplitude segments. Consequently, this methodology can be applied to systems with complex nonlinearities, such as systems with non-smooth restoring forces, general types of damping, etc. (v) The present method works for any type of harmonic excitation, external and/or parametric. Furthermore, the approach can be extended to include any type of excitation that can be modeled by a finite-state auxiliary dynamic system.

4.6 Figures

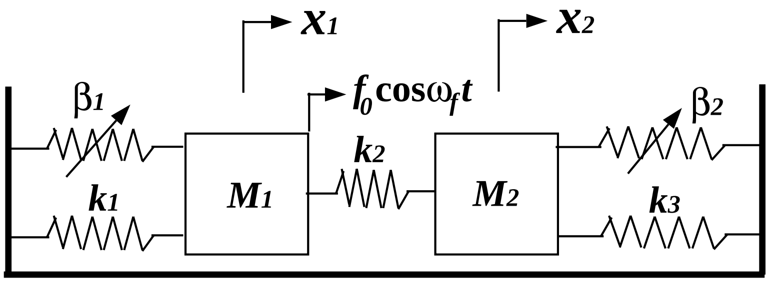

Figure 4.1: A two-degree-of-freedom mass-spring system

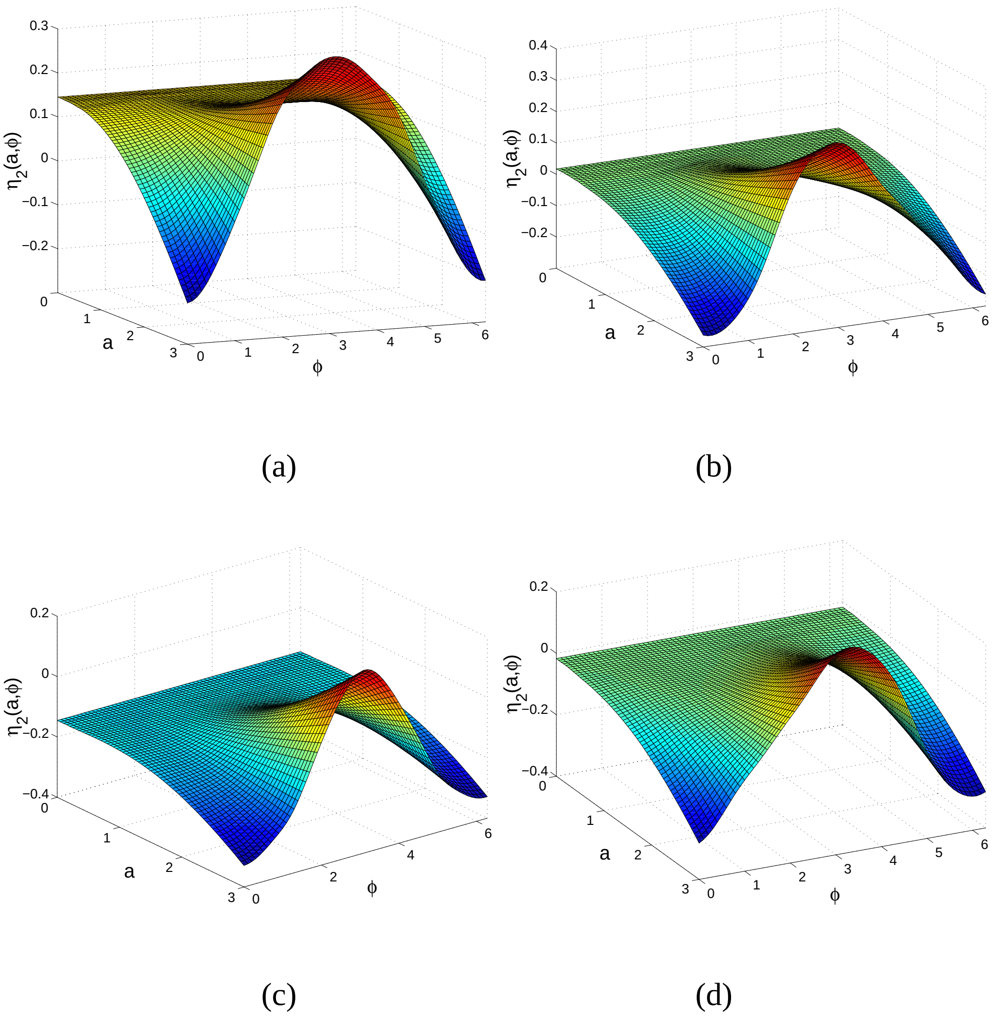

(a) (b)

(c) (d)

Figure 4.2: The first nonlinear mode invariant manifold for the position constraint, $\eta_2 = P_2(a, \phi, \phi_f)$, at various phase angles ϕ_f: (a) $\phi_f = 0.0$ (b) $\phi_f = \pi/2$ (c) $\phi_f = \pi$ (d) $\phi_f = 1.5\pi$.

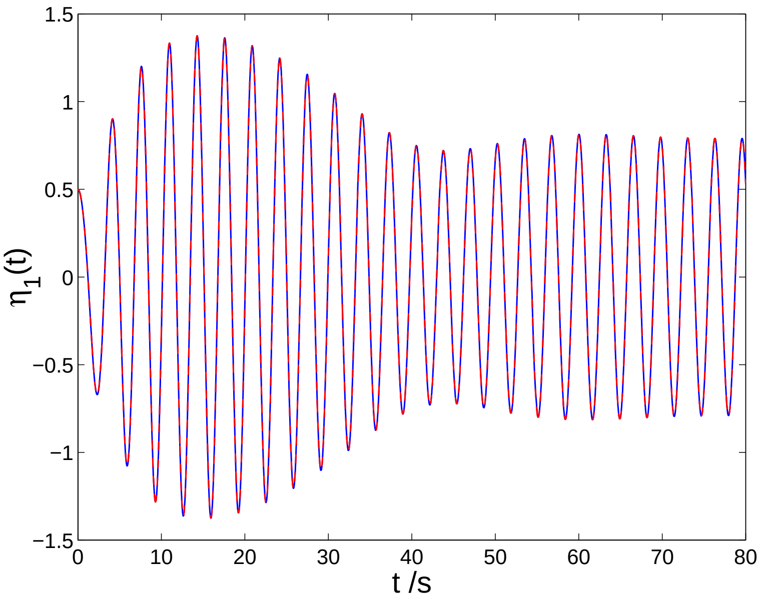

(a)

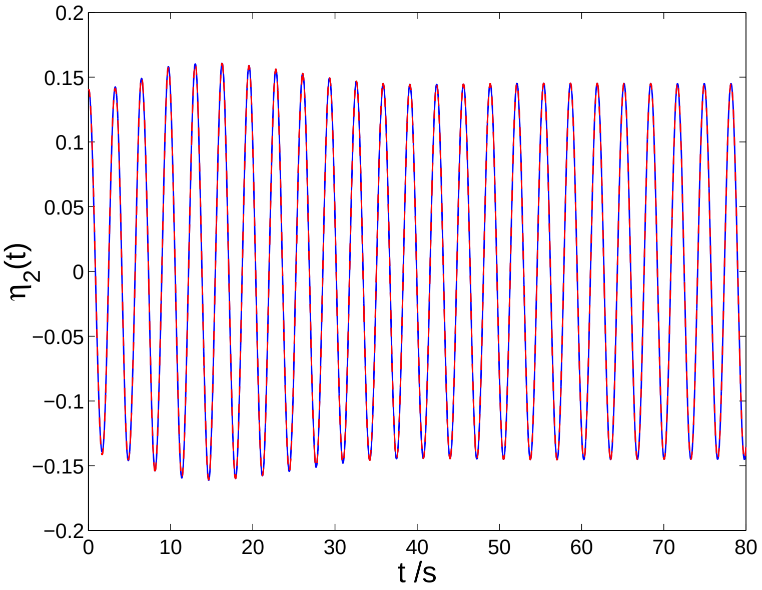

(b)

Figure 4.3: Comparison of the transient forced response of the modal coordinates, $\eta_1(t)$ and $\eta_2(t)$, with initial conditions $a(0) = 0.5$, $\phi(0) = 0.0$. ——, response obtained from the original system model; - - - , response from the reduced-order model.

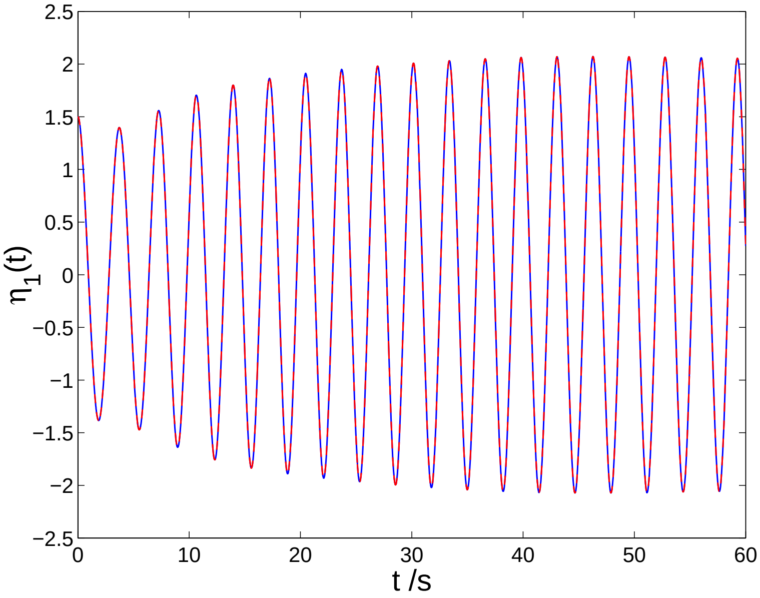

(a)

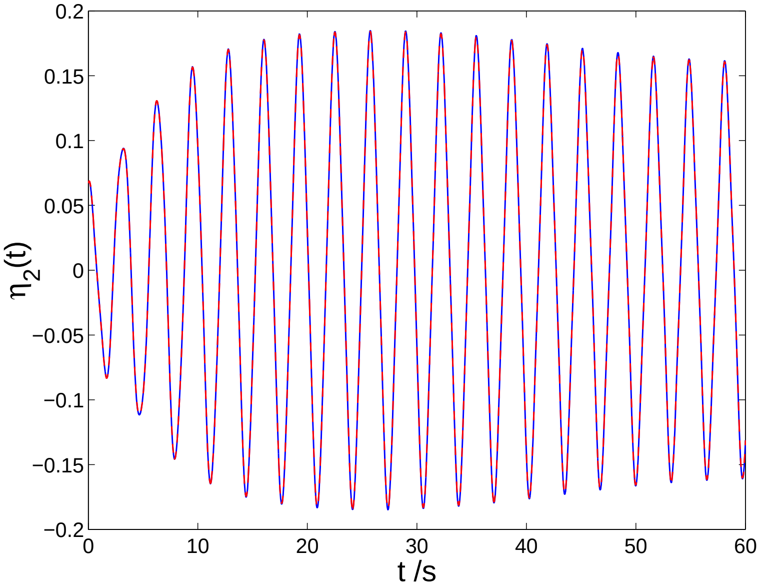

(b)

Figure 4.4: Comparison of the transient forced response of the modal coordinates, $\eta_1(t)$ and $\eta_2(t)$, with initial conditions $a(0) = 1.5$, $\phi(0) = 0.0$. ——, response obtained from the original system model; - - - , response from the reduced-order model.

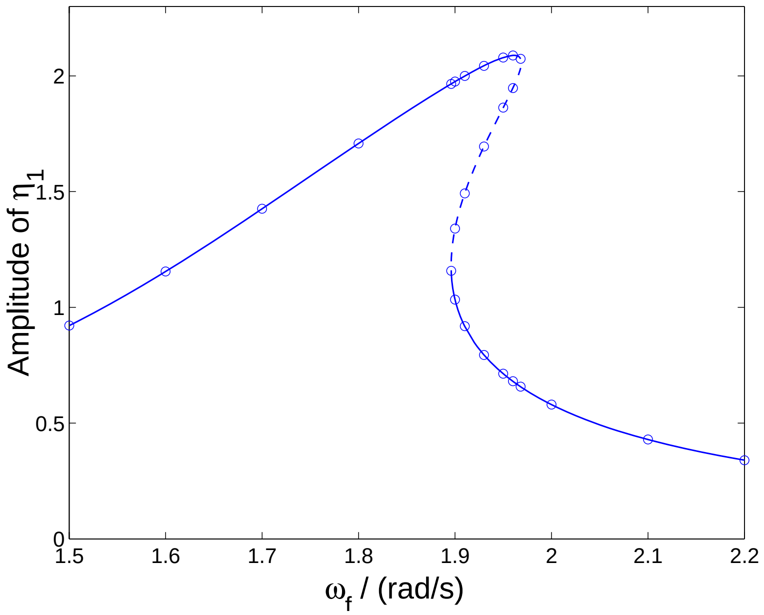

(a)

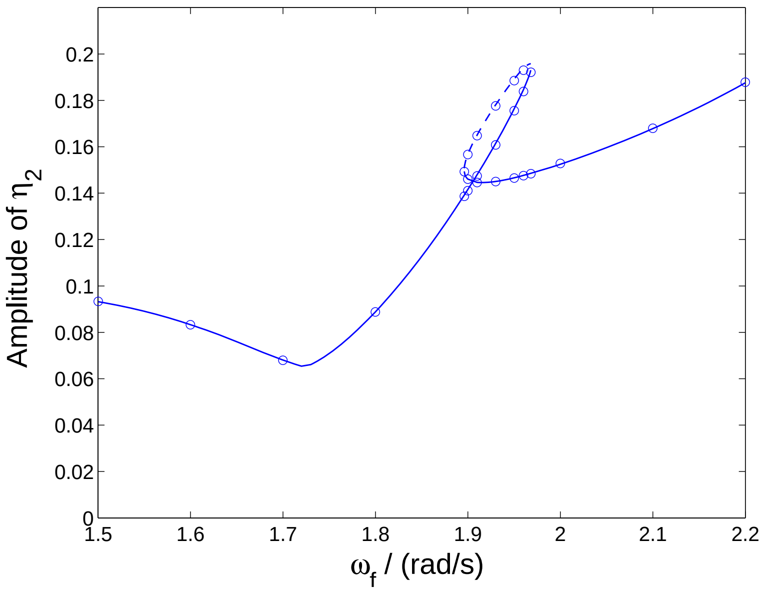

(b)

Figure 4.5: The amplitude of the steady-state response of the modal coordinates, $\eta_1(t)$ and $\eta_2(t)$, versus the excitation frequency, ω_f. ——, stable steady-state response obtained from the original system model; - - - , unstable steady-state response from the original system model; ‘ o ’ , steady-state response from the reduced-order model.

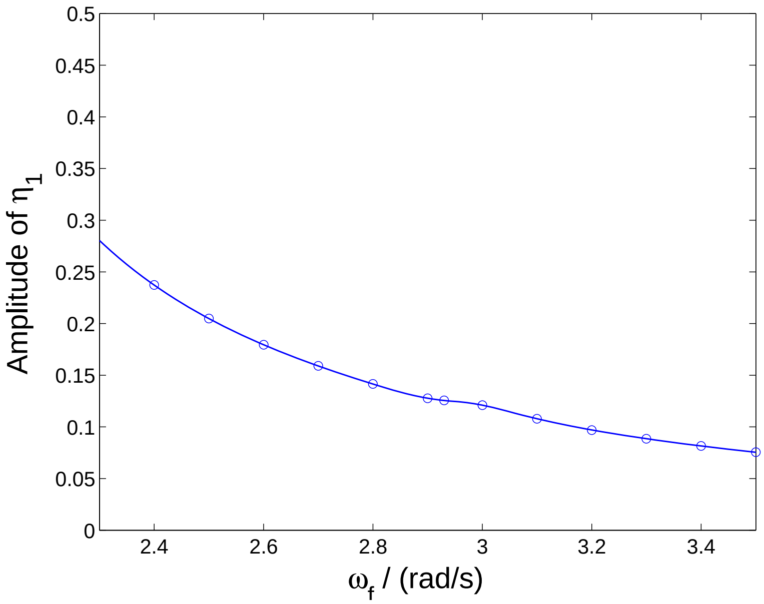

(a)

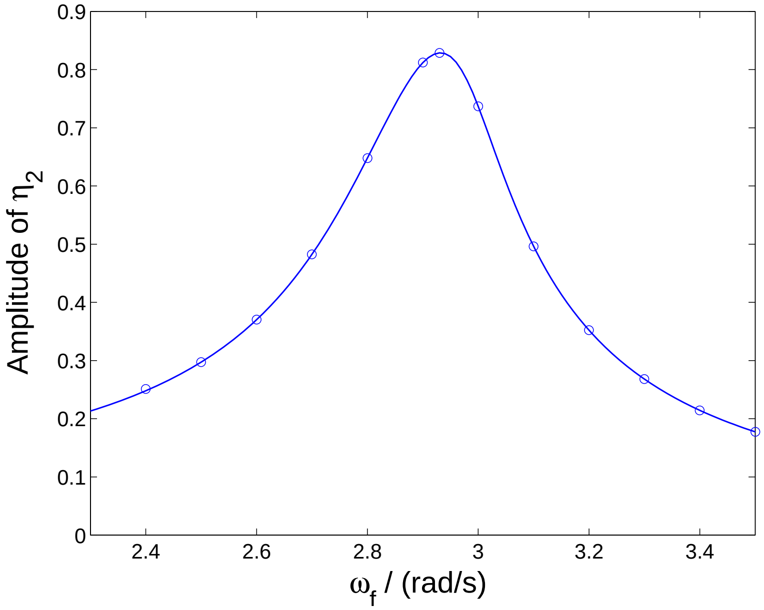

(b)

Figure 4.6: The amplitude of the steady-state response of the modal coordinate, $\eta_1(t)$ and $\eta_2(t)$, versus the excitation frequency, ω_f. ——, steady-state response obtained from the original system model; ‘ o ’ , steady-state response from the reduced-order model.

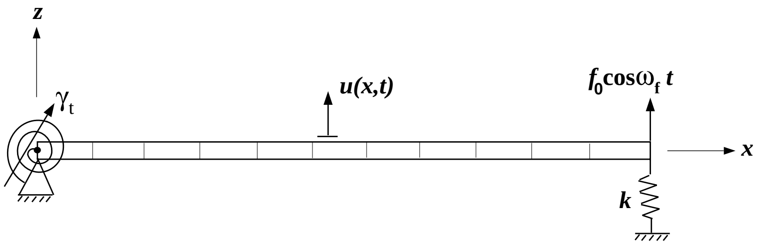

Figure 4.7: An Euler-Bernoulli beam with a nonlinear torsional spring, γ_t, at one end.

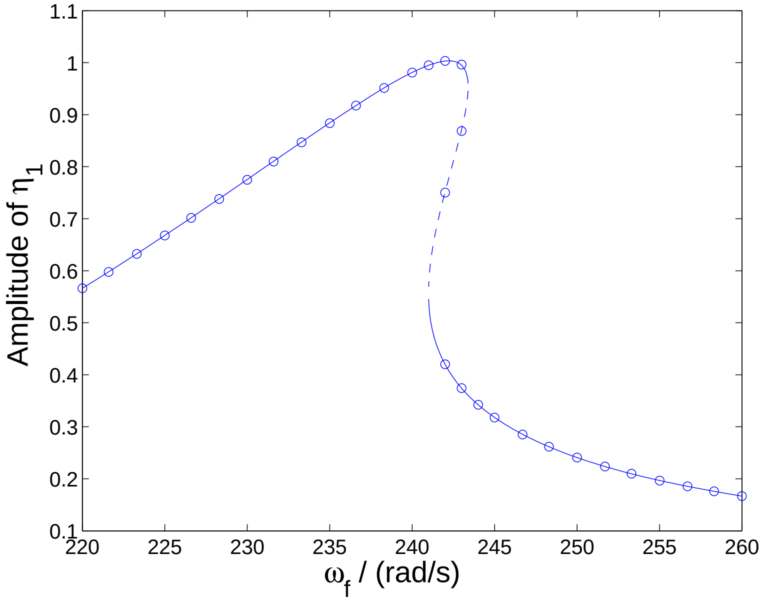

Figure 4.8: The amplitude of the steady-state response of the modal coordinates, $\eta_1(t)$, versus the excitation frequency, ω_f. ——, stable steady-state response obtained from the original system model; - - - , unstable steady-state response from the original system model; ‘ o ’ , steady-state response from the reduced-order model.

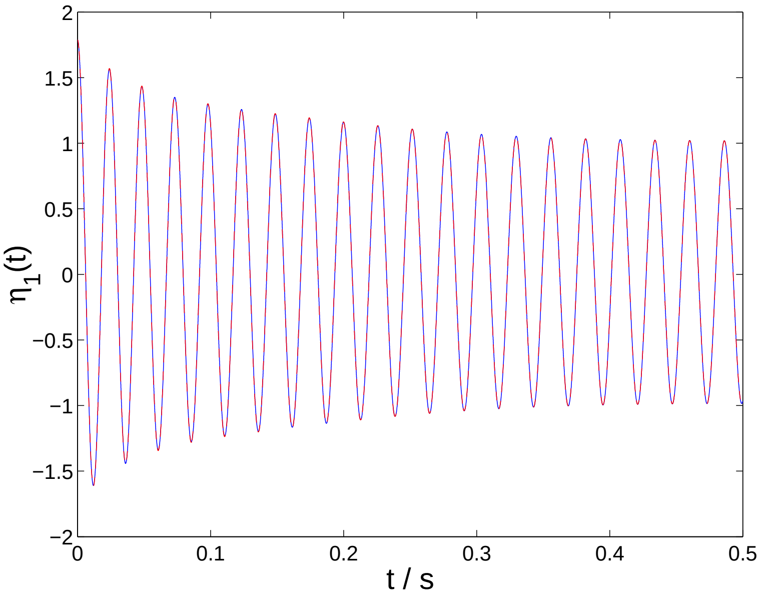

(a)

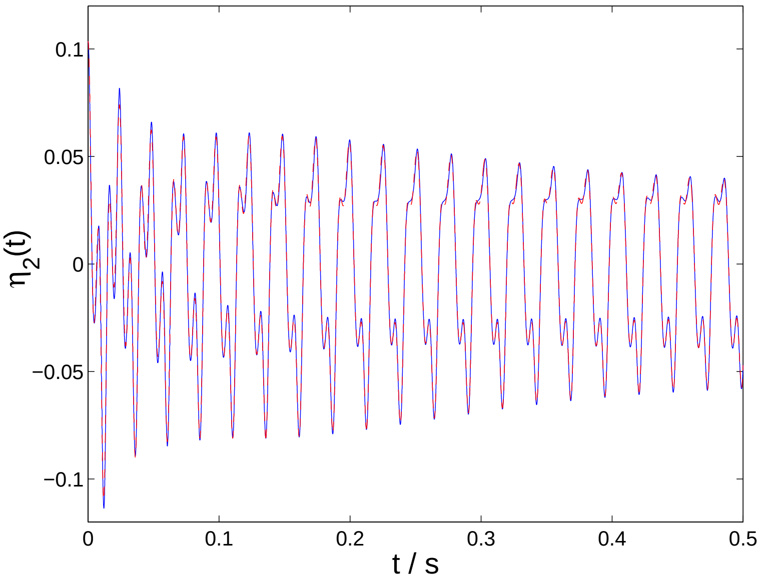

(b)

Figure 4.9: Comparison of the transient forced response of the modal coordinates, $\eta_1(t)$ and $\eta_2(t)$, with initial conditions $a(0) = 1.79$, $\phi(0) = 0.0$. ——, response obtained from the original system model; - - - , response from the reduced-order model.

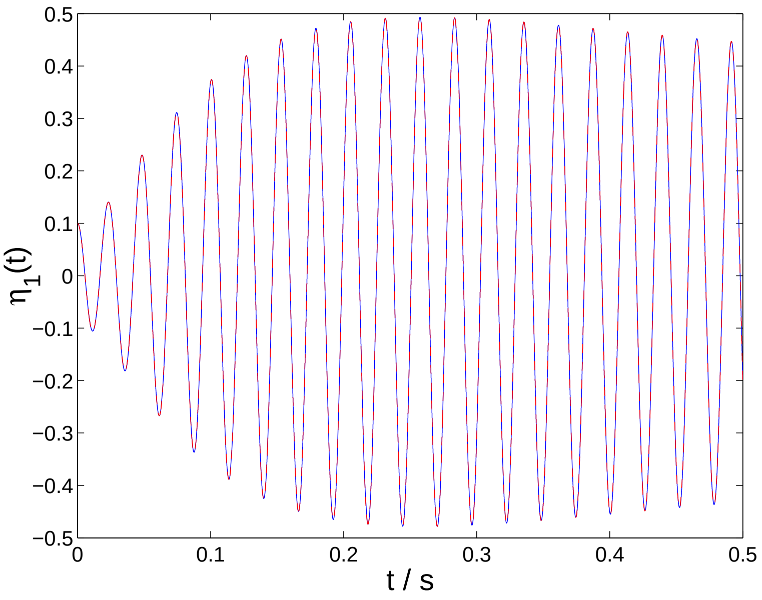

(a)

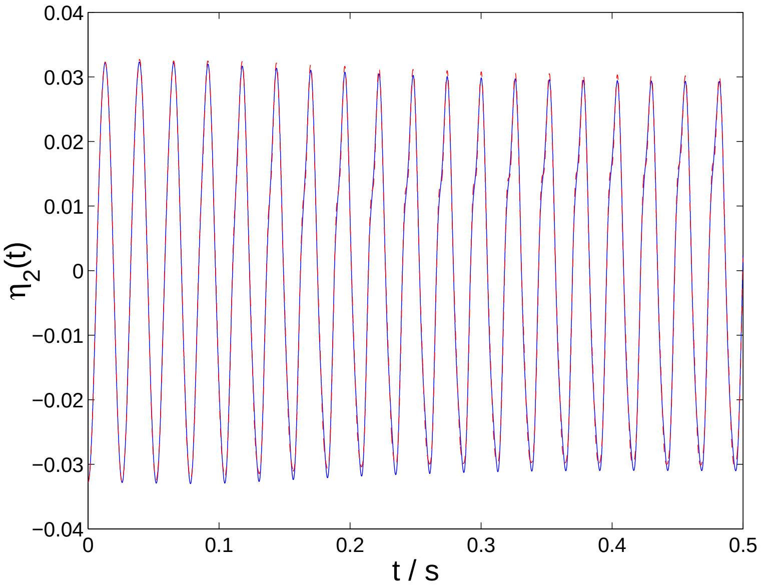

(b)

Figure 4.10: Comparison of the transient forced response of the modal coordinates, $\eta_1(t)$ and $\eta_2(t)$, with initial conditions $a(0) = 0.1$, $\phi(0) = 0.0$. ——, response obtained from the original system model; - - - , response from the reduced-order model.

CHAPTER V

APPLICATION OF NONLINEAR NORMAL MODES TO A ROTATING BLADE SYSTEM

5.1 Introduction

In the preceding chapters, the theory of nonlinear normal modes has been developed and applied to several example systems with various types of nonlinearities. The companion invariant manifold approach and Galerkin-based method have also been shown to be effective and efficient in the construction of the attendant reduced order models. In this chapter, the nonlinear normal mode theory is applied to a rotating rotorcraft blade, which is inherently nonlinear due to the complexity of its structural model.

Rotor blade models are crucially important to the accurate modeling of rotary-wing aircraft. In general blades are made of composite materials, and they can exhibit geometrically nonlinear behavior. It has been shown that nonlinearities arise primarily from the initial stress effect due to the high-speed rotation of the blade, and from the deformation-induced rotation of the cross sections of the blade [63]. In general, linear structural models do not effectively capture the dynamics of rotorcraft blades, especially for hingeless and bearingless blades.

A number of beam theories are available to account for moderate and large blade deflections. A review of the extensive literature concerned with the development of these theories is beyond the scope of this dissertation. The reader is referred to the excellent review paper by Friedmann and Hodges [63], which gives a thorough survey of research on beam kinematics during the past few decades. For moderate-deflection rotor blades, such as hingeless rotor blades, the nonlinearities are basically accounted for in the beam models by using ordering schemes. For rotor blades with large deflections, like bearingless rotors, ordering schemes are no longer valid, and geometrically exact theories must be used.

In this chapter, a large-deflection beam theory developed by Hodges [64] is utilized to formulate the nonlinear model of a rotating rotorcraft blade. The theory is based on a two-field variational principle of the Reissner-Hellinger type. A series of exact intrinsic equations can be obtained by using a mixed finite element formulation [65]. The resulting discretized finite element blade model is a complex model that is perfectly suited to illustrate the effectiveness of the model reduction technique based on nonlinear normal modes, since (a) the model is inherently nonlinear; (b) the deformation of the blade can be geometrically large and the corresponding nonlinear restoring forces can be strong; (c) different types of beam deformations, such as bending, torsion, lead-lag, and axial elongation, are present and are strongly coupled. As a result, an accurate reduced-order model can prove quite valuable in understanding the dynamic behavior of rotorcraft blades undergoing large deformations.

This chapter is organized as follows. In section 5.2, the beam theory utilized is briefly described, along with the companion mixed finite element discretization. In section 5.3, the example rotating blade system, an active twist rotor (ATR) blade system, is introduced. The ATR blade [66] has been used as a potential candidate for vibration and noise reductions in helicopters through the use of individual blade control. Here, the structural dynamics of the ATR blade are investigated. Linear modal analysis is applied to the linear part of the finite element equations of motion, and the resulting modal equations are subsequently transformed to standard form via a secondary modal analysis. In section 5.4, the nonlinear normal mode theory is extended and applied to the nonlinear blade model, and the construction method for the invariant manifolds is described. In section 5.5, the invariant manifolds are obtained for the nonlinear rotating blade, and the dynamics on them are computed and validated with time domain simulations. Finally, conclusions are drawn in section 5.6.

5.2 Large-deformation beam theory and finite element discretization

The large-deformation beam theory used here was developed by Hodges [64], and it is originally based on the three-field variational principle of the Hu-Washizu type. The beam configuration and base vectors are shown in figure 5.1, where x_1 denotes the length along the curved reference line r in the undeformed, but initially curved and twisted beam. The position vector $\mathbf{r}(x_1)$ locates a particle on the beam reference line relative to a fixed point in the reference frame A. According to the definition in reference [64], the frame A is an absolute frame in the sense that the orientation of the local undeformed beam cross-section in A is a function only of x_1 and not of time t. The motion of frame A in an inertial frame is known for all time. At each point along the reference line r, a frame b is defined with orthogonal unit vectors $\mathbf{b}_i$ for $i = 1, 2, 3$, where $\mathbf{b}_1$ is tangent to r, and $\mathbf{b}_2(x_1)$ and $\mathbf{b}_3(x_1)$ define the directions of local axes x_2 and x_3, respectively. Obviously, frame b gives the orientation of the undeformed cross-section plane in the frame A at any fixed point on the reference line r. Frame b varies along the beam if the beam is initially curved or twisted.

In the configuration of the deformed beam as shown in figure 5.1, a different curve R shows the locus of material points along r, and the length along R is denoted as s. A frame B is introduced at each point along R with orthogonal unit vectors $\mathbf{B}_i(x_1)$ for $i = 1, 2, 3$. The interpretation of the "intrinsic" frame B and the derivation of the beam formulation can be found in Hodges [64], and is not repeated here.

In order to facilitate the finite element formulation of the beam model, a two-field (Reissner-Hellinger type) variational formulation is used instead of the three-field principle [65]. The formulation is also adapted to a global coordinate system representation in the reference frame A. As a result, the initial configuration of the beam can be embedded conveniently in the formulation [65].

Another difficulty in the derivation of a large-deformation beam model is the determination of the material and geometric properties at each cross-section along the deformed reference curve R. These cross-sectional properties can be calculated numerically by using VABS, a code developed by Cesnik and Hodges [67], in matrix form as follows,

$$\left\{ \begin{array}{c} F_B \\ M_B \end{array} \right\} = [S] \left\{ \begin{array}{c} \gamma \\ \kappa \end{array} \right\} , \tag{5.1}$$

where γ and κ are the force and moment strain measures, respectively; F_B and M_B are the components of force and moment at the beam reference line in the deformed beam reference frame B; and the 6×6 coefficient matrix $[S]$ gives the cross-sectional information [65].

The finite element-based beam equations can be written in the following operator form, as given in reference [65],

$$G(X, \dot{X}, \bar{F}) = 0 \,, \tag{5.2}$$

where X is the vector of unknowns and G is a set of nonlinear functions derived from the finite element discretization[1]. The force vector $\bar{F}$ contains the effective nodal loads. The dimension of both X and G is $18N + 12$, where N is the total number of beam elements.

---

[1] The explicit form of each term in G is listed in reference [65], and it is not repeated here.

In the case of a cantilevered beam, the vector X is explicitly listed as follows,

$$\begin{aligned} X^T = \big[& \hat{F}_1^T \;\; \hat{M}_1^T \;\; u_1^T \;\; \theta_1^T \;\; F_1^T \;\; M_1^T \;\; P_1^T \;\; H_1^T \;\; \ldots \\ & u_N^T \;\; \theta_N^T \;\; F_N^T \;\; M_N^T \;\; P_N^T \;\; H_N^T \;\; \hat{u}_{N+1}^T \;\; \hat{\theta}_{N+1}^T \big] \; , \end{aligned} \tag{5.3}$$

where u_i^T and θ_i^T are the displacement and rotation measures at the i-th node respectively, F_i^T and M_i^T are the corresponding internal force and moment at the node, and P_i^T and H_i^T are the unknown linear and angular momentum. For a cantilevered beam, the reaction force and moment at the root where rotor and blade are connected are $\hat{F}_1^T$ and $\hat{M}_1^T$, while the unknown displacement and rotation are $\hat{u}_{N+1}^T$ and $\hat{\theta}_{N+1}^T$ at the blade tip. All the unknown quantities are expressed in the reference frame A.

The steady-state response of the rotating beam (i.e., its quasi-static response, which is constant in frame A) is solved from equation (5.2) by applying the Newton-Ralphson method [65]. Once the steady-state solution is obtained, equation (5.2) can be linearized about the equilibrium state, which results in a set of first-order differential equations,

$$[A]\{\dot{\tilde{X}}\} + [B]\{\tilde{X}\} = \{\tilde{F}\} \; , \tag{5.4}$$

where $\tilde{X}$ is the linearized dynamic response near the equilibrium state, $[A] = \frac{\partial G}{\partial \dot{X}}$, $[B] = \frac{\partial G}{\partial X}$, and $\tilde{F}$ contains the dynamic part of the external load. In this chapter, the external load on the beam is assumed to be static in the reference frame A. Consequently, the linear vibration eigen-modes of the system can be obtained from equation (5.4).

5.3 Rotating blade system model and linear modal analysis

The system selected is an active twist rotor (ATR) blade [66] shown in figure 5.2. The general properties of the ATR blade are listed in table 5.1. Note that a static load of 3800 N is applied to the blade tip in the axial direction due to the specified centrifugal loading. The cross-sectional property matrix $[S]$ used in equation (5.1) is not listed for the sake of simplicity. The dynamic response of this ATR blade model bas been investigated by Cesnik *et al.* [66]. Here, the aerodynamic coupling and the adaptive actuation are removed from the model, since only the structural dynamics are studied at this stage. The blade model is evenly divided into 11 beam elements in the reference frame A. The total number of DOF of the finite element model is 210.

At a constant rotating speed $\Omega = 72$ rad/s, the steady-state equilibrium position of the blade is shown in figure 5.3 with respect to the reference frame A. The steady-state position is a combination of the axial elongation, u_{A1}, and the deflection in the lead-lag direction, u_{A2}. The bending deflection u_{A3} and the torsion θ_{A1} are zero at the equilibrium position. The axial elongation can be attributed to the centrifugal load applied to the rotating blade, while the lead-lag deflection results from the intrinsic coupling between the axial elongation and the lead-lag motion for this ATR blade model. This coupling can be evidenced by performing a linear modal analysis, as described below.

Linear modal analysis can be applied to the rotating blade model linearized about the steady-state equilibrium position, which is given symbolically in equation (5.4). With the assumption that the external dynamic load is zero in equation (5.4), the free vibration eigen-modes can be obtained by seeking a solution in the form,

$$\tilde{X} = \phi_i e^{\lambda_i t} \ , \tag{5.5}$$

where ϕ_i is the i-th eigenvector and λ_i is the corresponding eigenvalue. The eigenvectors and the eigenvalues are complex in general, since the matrices $[A]$ and $[B]$ in equation (5.4) are not symmetric. The Lanczos method is used here to extract the complex eigen-modes.

The first 25 eigen-modes [1] are listed in table 5.2. The physical characteristics of the various mode shapes are denoted by the letters A, B, L, and T, which stand for the axial

---

[1] For each mode, there exists a complex conjugate counterpart, which is not listed for the sake of simplicity.

elongation, bending deflection, lead-lag deflection, and torsion of the blade, respectively. It is found that for most modes, the vibration shape is a combination of two of these characteristic motions. In particular, the bending deflection is always coupled with the torsion, as depicted in figure 5.4, while the lead-lag motion is always coupled with the axial elongation, as shown in figure 5.5.

In table 5.2, it is observed that each eigenvalue features a small, but nonzero real part, either negative or positive, corresponding to amplitude decay or growth in the corresponding mode, respectively. Since structural damping is not included in the blade model, it is believed that these nonzero real parts originate from numerical approximations, both in the algorithm used for the eigen-analysis and in the cumbersome calculations of the elements of the linear system matrices (this was confirmed after discussion with the provider of the ATR blade model [66]). In addition, the real parts in table 5.2 are very small, at least six orders of magnitude smaller than the corresponding imaginary parts. As a result, the equilibrium position of this ATR blade can be considered stable, since the actual structural damping in the blade would be always be large enough to compensate for the positive real part of the eigenvalues.

Using the obtained 25 linear eigen-modes, the linearized ATR blade model, equation (5.4), can be reduced to an approximate subspace spanned by 25 vibration modes. With the introduction of the coordinate transformation,

$$\tilde{X} = [\Phi] Y \ , \tag{5.6}$$

where

$$\begin{aligned} [\Phi] &= [\ \mathrm{Re}(\phi_1), \mathrm{Im}(\phi_1), \mathrm{Re}(\phi_2), \mathrm{Im}(\phi_2), \cdots, \mathrm{Re}(\phi_{25}), \mathrm{Im}(\phi_{25})\ ] \ , \\ Y &= [\ y_1,\ y_2,\ \cdots\ ,\ y_{50}\ ]^T \ , \end{aligned}$$

equation (5.4) is transformed via linear modal analysis to

$$[M_r]\dot{Y} + [K_r]Y = 0 \; , \tag{5.7}$$

where

$$[M_r] = [\Phi]^T [A][\Phi], \quad [K_r] = [\Phi]^T [B][\Phi] \; .$$

Inverting the matrix $[M_r]$, the reduced-order system, equation (5.7), can be rewritten as

$$\dot{Y} + [K_D]Y = 0 \; , \tag{5.8}$$

where $[K_D] = [M_r]^{-1}[K_r]$.

Next, secondary linear modal analysis can be applied to the reduced-order blade system, equation (5.8). These new eigen-modes are obtained in the form,

$$Y = \psi_i e^{\lambda_i t}, \qquad i = 1, \cdots, 25 \;\; , \tag{5.9}$$

where ψ_i is the i-th eigenvector and λ_i is the i-th eigenvalue. The i-th eigenvalue is equal to the corresponding eigenvalue obtained in the first modal analysis, and is shown in table 5.2. The coordinate transformation for the secondary modal analysis is defined as

$$Y = [\Psi]\eta \; , \tag{5.10}$$

$$\begin{aligned} [\Psi] &= [\ \mathrm{Re}(\psi_1), \mathrm{Im}(\psi_1), \mathrm{Re}(\psi_2), \mathrm{Im}(\psi_2), \cdots, \mathrm{Re}(\psi_{25}), \mathrm{Im}(\psi_{25})\ ] \; , \\ \eta &= [\ s_1,\ t_1,\ s_2,\ t_2, \cdots,\ s_{25},\ t_{25}\ ]^T \; , \end{aligned}$$

where (s_i, t_i) are the first-order modal coordinates associated with the i-th mode. The final linearized reduced-order system takes the form

$$\dot{\eta} + [\Lambda_D]\eta = 0 \; , \tag{5.11}$$

where $[\Lambda_D] = [\Psi]^{-1}[K_D][\Psi]$. The matrix $[\Lambda_D]$ is block diagonal [68], and it takes the following form

$$[\Lambda_D] = \left[\begin{array}{cccc}
\begin{array}{cc} -\text{Re}(\lambda_1) & -\text{Im}(\lambda_1) \\ \text{Im}(\lambda_1) & -\text{Re}(\lambda_1) \end{array} & 0 & \cdots & 0 \\
0 & \begin{array}{cc} -\text{Re}(\lambda_2) & -\text{Im}(\lambda_2) \\ \text{Im}(\lambda_2) & -\text{Re}(\lambda_2) \end{array} & \cdots & 0 \\
\vdots & \vdots & \ddots & 0 \\
0 & 0 & 0 & \begin{array}{cc} -\text{Re}(\lambda_{25}) & -\text{Im}(\lambda_{25}) \\ \text{Im}(\lambda_{25}) & -\text{Re}(\lambda_{25}) \end{array}
\end{array}\right] \tag{5.12}$$

System (5.11) is decoupled with respect to each pair of linear modal coordinates, s_i and t_i. Since the two coordinate transformations used in the linear modal analysis procedure are real, the final reduced-order system is expressed solely in terms of real quantities. This two-step coordinate transformation is necessary to facilitate the construction of the nonlinear normal modes for the ATR blade model, which is described next.

5.4 Nonlinear normal mode theory for the rotor-blade system

The finite element-based ATR blade model is expressed in the following symbolic form

$$[A]\dot{\tilde{X}} + [B]\tilde{X} + F_{nl}(\tilde{X}) = 0 \; , \tag{5.13}$$

where the matrices $[A]$, $[B]$, and the vector $\tilde{X}$ are defined in equation (5.4), which represents the linearized system with respect to the equilibrium position. The nonlinear force vector, $F_{nl}(\tilde{X})$, can only be obtained numerically from the finite element code provided by Cesnik *et al.* [66]. This is because no explicit expression of the nonlinear force is available due to the complexity of the ATR blade model. For the sake of simplicity, it is assumed that the nonlinear force is independent of the time derivative of the dynamic response, $\dot{\tilde{X}}$. Furthermore, the dynamic external load is not included in equation (5.13).

With the two-step linear modal analysis defined in equations (5.6–5.11), system (5.13) can be transformed to the following form

$$\left\{\begin{array}{l} \dot{s}_i + \xi_i\omega_i s_i - \omega_i t_i + f_{s_i}(s_1,\cdots,s_{25};t_1,\cdots,t_{25}) = 0 \\ \\ \dot{t}_i + \omega_i s_i + \xi_i\omega_i t_i + f_{t_i}(s_1,\cdots,s_{25};t_1,\cdots,t_{25}) = 0 \end{array}\right. , \quad \text{for } i = 1,\cdots,25 \qquad (5.14)$$

where the linear part is block-diagonal. For each linear vibration mode, the linear modal frequency, ω_i, and the linear modal damping ratio, ξ_i, are introduced with the definitions [2]

$$\omega_i = \text{Im}(\lambda_i), \quad \xi_i = -\frac{\text{Re}(\lambda_i)}{\text{Im}(\lambda_i)} . \qquad (5.15)$$

The nonlinear force expressed in finite element coordinates is projected onto the 25 pairs of linear mode shapes, yielding the nonlinear force in the linear modal coordinates, as follows

$$\left\{\begin{array}{c} f_{s_1} \\ f_{t_1} \\ \vdots \\ f_{s_{25}} \\ f_{t_{25}} \end{array}\right\} = [\Psi]^{-1}[M_r]^{-1}[\Phi]^T F_{nl}([\Phi][\Psi]\eta) . \qquad (5.16)$$

The transformation matrices $[\Psi]$, $[M_r]$, and $[\Phi]$, and the vector η are defined in equations (5.6–5.11).

---

[2] According to the conventional definitions of the linear modal frequency and the modal damping ratio [68], it follows that

$$\text{Re}(\lambda_i) = -\xi_i\omega_i, \quad \text{Im}(\lambda_i) = \omega_i\sqrt{1-\xi_i^2} .$$

Here, an approximate version of this definition is utilized since the damping ratios are very small for the ATR blade model.

In order to initiate the construction of the nonlinear normal modes for the ATR blade model, one pair of linear modal coordinates, (s_k, t_k), is chosen to be the master coordinates. These are transformed to polar form as follows

$$\begin{cases} s_k = a\cos\phi \\ t_k = a\sin\phi \end{cases}, \quad k = 1, \cdots, 25 \; . \tag{5.17}$$

The efficiency of the use of polar form master coordinates, (a, ϕ), in nonlinear normal mode construction has been justified for numerous applications [54, 56]. The selection of the master coordinates is based on the frequency region in which the nonlinear dynamic response of the ATR blade is of interest. For instance, the master coordinates can be chosen as the first linear modal coordinates, $k = 1$, if the dynamic response near the first bending mode (flap blade motion) needs to be investigated.

According to the definition of the invariant manifold, all the remaining DOFs of the system are constrained to the master coordinates. The remaining linear modal coordinates are denoted as slave coordinates, and their constraint relationships with the master coordinates are expressed symbolically as

$$\begin{cases} s_i = P_i(a, \phi) \\ t_i = Q_i(a, \phi) \end{cases}, \quad i = 1, \cdots, 25, \; i \neq k \; . \tag{5.18}$$

The essential part in the construction of the nonlinear normal mode is to determine the constraint relationship, P_i's and Q_i's.

The derivation of the partial differential equations governing the slave constraint relationships is briefly described as follows. First, the constraint relationships, equation (5.18), are substituted into the nonlinear system of equations of motion, equation (5.14). It follows that

$$\begin{cases} \frac{\partial P_i}{\partial a}\dot{a} + \frac{\partial P_i}{\partial \phi}\dot{\phi} + \xi_i\omega_i P_i - \omega_i Q_i + f_{s_i} = 0 \\ \frac{\partial Q_i}{\partial a}\dot{a} + \frac{\partial Q_i}{\partial \phi}\dot{\phi} + \omega_i P_i + \xi_i\omega_i Q_i + f_{t_i} = 0 \end{cases}, \quad i = 1, \cdots, 25, \; i \neq k \; . \tag{5.19}$$

Then, the polar form master coordinates, equation (5.17), are substituted into the system of equations (5.14) to obtain the governing equations in the master coordinates,

$$\left\{ \begin{array}{l} \dot{a} = -\xi_k \omega_k a - f_{s_k} \text{cos}\phi - f_{t_k} \text{sin}\phi \\ \dot{\phi} = -\omega_k + (f_{s_k} \text{sin}\phi - f_{t_k} \text{cos}\phi)/a \end{array} \right. . \tag{5.20}$$

Equation (5.20) is then substituted into equation (5.19), and the differential equations governing the slave constraints are finally obtained as

$$\left\{ \begin{array}{l} \frac{\partial P_i}{\partial a}(-\xi_k \omega_k a - f_{s_k} \text{cos}\phi - f_{t_k} \text{sin}\phi) + \\ \qquad \frac{\partial P_i}{\partial \phi}[-\omega_k + (f_{s_k} \text{sin}\phi - f_{t_k} \text{cos}\phi)/a] + \xi_i \omega_i P_i - \omega_i Q_i + f_{s_i} = 0 \\ \frac{\partial Q_i}{\partial a}(-\xi_k \omega_k a - f_{s_k} \text{cos}\phi - f_{t_k} \text{sin}\phi) + \\ \qquad \frac{\partial Q_i}{\partial \phi}[-\omega_k + (f_{s_k} \text{sin}\phi - f_{t_k} \text{cos}\phi)/a] + \omega_i P_i + \xi_i \omega_i Q_i + f_{t_i} = 0 \end{array} \right. , \tag{5.21}$$

for $i = 1, \cdots, 25, \;\; i \neq k$.

Once equation (5.21) is solved, the constraint relationships can be substituted into equation (5.20). Consequently, the nonlinear dynamics on the invariant manifold are solely governed by the master coordinates, (a, ϕ).

The differential equations for the invariant manifold, equation (5.21), has to be solved numerically, and here a Galerkin method is used. First, the two-dimensional solution domain

$$\left\{ \; (a, \phi) \; \middle| \; a \in (0, a_{max}], \; \phi \in [0, 2\pi] \; \right\} , \tag{5.22}$$

is evenly discretized into n stripe-shaped segments,

$$\left\{ \; (a, \phi) \; \middle| \; a \in [l\Delta a, (l+1)\Delta a], \; \phi \in [0, 2\pi] \; \right\}, \;\; 0 \leq l \leq n-1 , \tag{5.23}$$

where a_{max} is the upper limit of the construction domain for the invariant manifold, and $\Delta a = a_{max}/n$ is the width of each segment in the a direction. In each segment, the constraint relationships, P_i's and Q_i's, are then expanded as

$$\begin{cases} P_i(a,\phi) = \sum_{\alpha=1}^{2} \sum_{\beta=1}^{N_\phi} C^i_{\alpha\beta} T_\alpha(a) H_\beta(\phi) \\ Q_i(a,\phi) = \sum_{\alpha=1}^{2} \sum_{\beta=1}^{N_\phi} D^i_{\alpha\beta} T_\alpha(a) H_\beta(\phi) \end{cases} , \quad i = 1, \cdots, 25, \;\; i \neq k \ , \tag{5.24}$$

where $C^i_{\alpha\beta}$, $D^i_{\alpha\beta}$ are the unknown coefficients, and the expansion functions are defined as

$$T_1(a) = \frac{a - l\Delta a}{\Delta a}, \quad T_2(a) = \frac{(l+1)\Delta a - a}{\Delta a}, \quad \text{for } a \in \big[l\Delta a, (l+1)\Delta a\big], \tag{5.25}$$

and

$$H_\beta(\phi) = \begin{cases} \cos\frac{\beta-1}{2}\phi \ , & \beta \text{ is odd} \\ \sin\frac{\beta}{2}\phi \ , & \beta \text{ is even} \end{cases} . \tag{5.26}$$

Using this approach, the accuracy of the slave constraints, P_i's and Q_i's, is controlled by the segment width Δa and the total number of terms, N_ϕ, in the Fourier expansion.

The expansions (5.24) are substituted into the invariant manifold equation (5.21). Using a Galerkin projection, a series of algebraic equations can be obtained in the unknown coefficients, C's and D's. The Galerkin projection is expressed as

$$\int_{l\Delta a}^{(l+1)\Delta a} \int_0^{2\pi} T_\alpha(a) H_\beta(\phi) Rsd_i(a, \phi, \mathbf{C}, \mathbf{D}) \, d\phi \, da = 0 \ , \tag{5.27}$$
$$\text{for } \alpha = 1, 2, \;\; \beta = 1, \cdots, N_\phi, \;\; i = 1, \cdots, 25, \;\; \text{and } i \neq k \ ,$$

where $\mathbf{C}$ and $\mathbf{D}$ are the vectors of the unknown coefficients $C^i_{\alpha\beta}$ and $D^i_{\alpha\beta}$. The residual functions $Rsd_i(a, \phi, \mathbf{C}, \mathbf{D})$ represent the left hand side of the invariant manifold equation, which are projected onto each expansion function defined in equation (5.24). The Hybrid Powell's method [57] is used to solve the resulting algebraic equations numerically. Once the invariant manifold has been constructed in each discretized segment, the various pieces can be assembled [54] and the invariant manifold can be obtained over the whole solution domain (5.22).

5.5 Invariant manifold results

The motion of the nonlinear rotating ATR blade in its first (lowest frequency) mode of vibration is investigated. In order to construct the nonlinear normal mode, the linear modal coordinates corresponding to the first linear mode, (s_1, t_1) in system (5.14), are selected as the master coordinates. Note that in this first linear mode the motion is primarily first-order bending (flap) along with a small first-order torsion component. The slave coordinates are chosen as the 10 pairs of linear modal coordinates, (s_i, t_i), $i = 2, 3, \cdots, 11$, in system (5.14). According to table 5.2, this selection of slave coordinates includes the following ATR blade modes: the bending (flap) modes up to the fifth order, the torsion modes up to the second order, the lead-lag modes up to the third order, and the axial elongation modes up to the second order. It is believed that this selection of the slave coordinates is sufficient for the determination of the first bending nonlinear mode. All the remaining DOFs for high-order modes, (s_i, t_i), $i = 12, 13, \cdots, 25$, in system (5.14), are neglected in the construction of the invariant manifold. In other words, the constraint relationships, P_i's and Q_i's, are set equal to zero for these high-order modes.

Linear modal damping is added to system (5.14) to increase numerical stability in the construction of the nonlinear normal mode. As shown in table 5.3, the modal damping ratio added to the master and slave modes ranges from 0.01 for the low modes to 0.1 for the high modes. The latter value is not small in the sense of structural damping, but may be reasonable if aerodynamic damping is considered.

In the numerical construction of the nonlinear normal mode corresponding to the first-order bending motion, the upper limit of the solution domain, a_{max} in equation (5.22), is taken as 1200, and the amplitude domain is evenly discretized into 60 segments. The total number of harmonic terms in the Galerkin expansion (5.24) in the phase coordinate is set as $N_\phi = 18$. The unknown coefficients in equation (5.24) are solved for using the Hybrid Powell method, and the resulting constraint relationships for the slave coordinates are depicted in figures 5.6–5.9 for four out of the ten slave modes. These constraints define the geometry of the invariant manifold for the first nonlinear normal mode. One conclusion that can immediately be drawn is that, among all slave modes (those shown, but also all others), the first axial elongation mode, which is shown in figure 5.9, makes the largest contribution to the motion of the blade system in its first nonlinear normal mode. Moreover, the contribution from the first lead-lag mode, figure 5.6, is much larger than the contributions from the second bending mode, figure 5.7, and from the first torsion mode, figure 5.8. Thus, the constraint relationships clearly demonstrate that the axial elongation modes and the lead-lag modes are crucial in the analysis of the bending motion of the ATR blade model.

Once the invariant manifold for the first nonlinear normal mode has been determined, the dynamics on the manifold can be reduced to those of the master coordinates, (a, ϕ), which are governed by the reduced-order model, equation (5.20). Figures 5.10–5.13 depict the time responses corresponding to a motion on the first mode invariant manifold. The results shown are obtained from three different procedures. In the *first* procedure, the blade system response is obtained from the single-DOF, invariant manifold-based reduced-order model, equation (5.20). The master coordinates are first computed by numerical integration. The responses of the slave coordinates are then recovered using the slave constraint relationships, equation (5.18). In the *second* procedure, the response of the original nonlinear equations of motion in the linear modal coordinates, equation (5.14), is obtained directly by numerical integration (with 11 retained linear modes rather than 25). The initial conditions for the 11 pairs of modal coordinates, (s_i, t_i) for $i = 1 \cdots 11$, are the same as in the first procedure. The *third* procedure consists of a single-mode time simulation of the equations of motion, namely equation (5.14) in which only the modal coordinates (s_1, t_1) of the first linear mode are retained, with all other modal coordinates, (s_i, t_i) for $i > 1$, being set to zero for all time. In all three time simulation procedures, the initial conditions for the master coordinates are set as $(s_1(0), t_1(0)) = (1190, 0)$.

In figure 5.10, the simulation obtained from the invariant manifold-based reduced-order model matches the time response obtained from the original 11-DOF model precisely, while the single-mode simulation deviates significantly from the original system response as time marches. In the comparisons of the time responses for the slave coordinates, figures 5.11–5.13, the responses from the reduced-order model are very good representations of the original system responses. The one-mode simulations are not plotted since they are all zero. It is observed that the effect of damping in the reduced-order model is slightly larger than in the original system. The reason for this “over-damping” in the invariant manifold is not understood yet.

These results show that the efficient single-DOF reduced-order model based on the invariant manifold provides an accurate approximation of the blade response, while the nonlinear model truncated to a single linear blade mode does not. In fact, a model that includes 11 linear modes is needed to achieve the accuracy of the single-DOF nonlinear normal mode model. This means that the blade’s higher vibration modes, and particularly the first axial elongation mode, have a significant effect on the first-order bending mode response through nonlinear coupling effects.

The comparisons of the responses of the master and slave coordinates, figures 5.10–5.13, evidence the accuracy of the constructed nonlinear normal mode for the first-order bending motion. Based on the time responses obtained from the invariant manifold-based reduced-order model, the motion of the ATR blade model in the physical coordinates, $\tilde{X}$ in equation (5.13), is shown in figures 5.14 and 5.15. The peak-to-peak bending deflection at the blade tip is about $16\ cm$, which is considerable for a blade of length $1.397\ m$. The torsional motion of the blade is also large, with the peak-to-peak twist angle at the blade tip being above $0.2\ radians$ ($11.4\ degrees$). Although the lead-lag and the axial elongation vibrational motion amplitudes are very small compared to the steady-state position of the ATR blade model (see figure 5.3), the nonlinear interactions contributed from these motions are important to the accuracy of the nonlinear normal mode, because the blade stiffness in these directions is designed to be much larger than the stiffness in the bending and torsion directions.

5.6 Conclusions

For a typical rotating blade model, namely an active twist rotor (ATR) blade, the nonlinear normal mode corresponding to the first-order bending motion has been successfully constructed. A single-DOF reduced-order model has been obtained from the corresponding invariant manifold. This reduced-order model accurately and efficiently represents the nonlinear dynamics of the blade in its first-order bending mode. Numerical time simulations on the invariant manifold have shown that the lead-lag and the axial elongation motions are essential in capturing the bending-dominated blade motion accurately.

Nonlinearities in the rotating blade are much more intricate than those in the example systems of the preceding chapters, and the finite element method had to be utilized to obtain the blade's equations of motion. Also, in general the eigenvalues and eigenvectors of the linearized system are complex. A numerical methodology has been proposed for the construction of the invariant manifold for such complicated nonlinear systems. This methodology can be conveniently extended to more complete rotating blade models, including those with structural damping and aerodynamic coupling.

In this study, a single pair of linear modal coordinates is selected as the master coordinates. In practice, additional linear modes can be included as master modes, and the current numerical methodology can be extended to the construction of multi-mode invariant manifolds for rotating blade systems.

5.7 Tables and Figures

Blade chord, c	10.77 cm
Blade length	1.397 m
Blade pretwist	0 rad
Hinge offset	7.62 cm
Root cutoff	31.75 cm
Pitch axis	25% chord
Elastic axis	25% chord
Center of gravity	25% chord
Centrifugal loading at tip	738.5 g
Rotor speed	72.0 rad/s
Mass per unit span	0.6960 kg/m
Section torsional inertia	$3.307 \times 10^{-4}\ kg\ m^2\ m^{-1}$

Table 5.1: General properties of the ATR blade model [66].

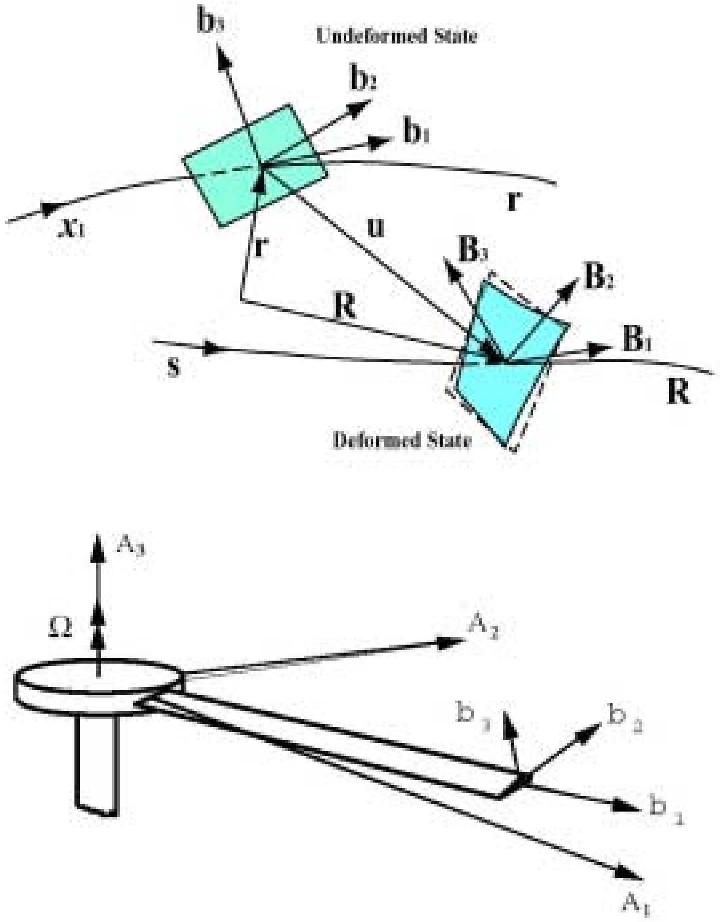

Figure 5.1: Schematic of the undeformed and deformed beam reference lines and cross-sections [64–66].

Mode # i	Eigenvalue λ_i	Modal shape
1	1.011E-6 + i 1.336E2	1B-1T
2	6.857E-6 + i 1.605E2	1L-1A
3	1.447E-6 + i 3.747E2	2B-1T
4	-1.386E-4 + i 5.463E2	1T
5	1.109E-4 + i 6.308E2	3B-1T
6	1.874E-5 + i 6.898E2	2L-2A
7	-1.462E-4 + i 1.016E3	4B-2T
8	1.767E-5 + i 1.604E3	3L-2A
9	-3.690E-3 + i 1.652E3	2T-5B
10	3.483E-3 + i 1.662E3	5B-2T
11	-2.643E-5 + i 2.403E3	1A
12	-1.367E-3 + i 2.729E3	6B-3T
13	9.730E-4 + i 2.862E3	6B-3T
14	1.856E-5 + i 3.085E3	4L-3A
15	-4.512E-4 + i 4.237E3	4T-7B
16	-3.662E-4 + i 4.569E3	4T-7B
17	-1.187E-3 + i 5.769E3	5L-4A
18	3.702E-4 + i 5.781E3	7B-5T
19	8.918E-4 + i 7.161E3	2A-6L
20	3.601E-4 + i 7.244E3	8B-6T
21	-2.952E-3 + i 7.869E3	8B-6T
22	3.093E-3 + i 9.447E3	7T
23	5.520E-3 + i 1.025E4	6L-5A
24	-1.526E-2 + i 1.081E4	3A
25	-1.375E-2 + i 1.372E4	8B

Table 5.2: The first 25 linear eigen-modes of the ATR blade. In the modal shape column, B denotes the bending deflection, T the torsion, L the lead-lag deflection, and A the axial elongation.

Mode number, i	Modal damping ratio, ξ_i
1, 2, 3	0.01
4, 5, $\cdots$, 9	0.05
10, 11	0.10

Table 5.3: Modal damping ratios added to system (5.14) for the construction of the first nonlinear normal mode.

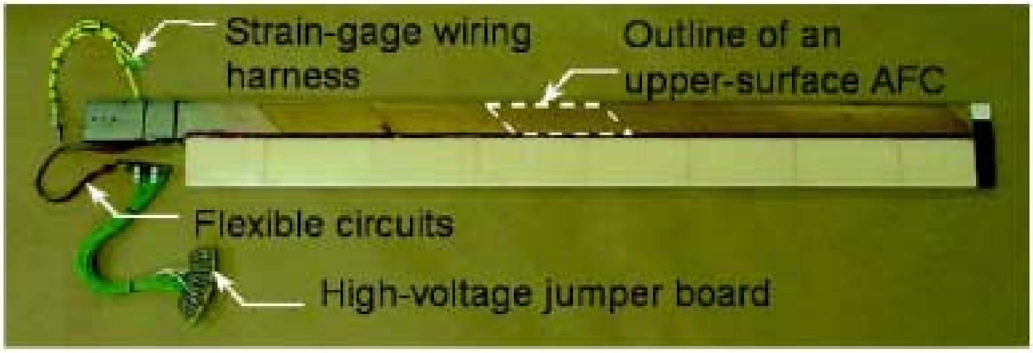

Figure 5.2: The prototype of the active twist rotor (ATR) blade [66]. AFC denotes the active fiber composites.

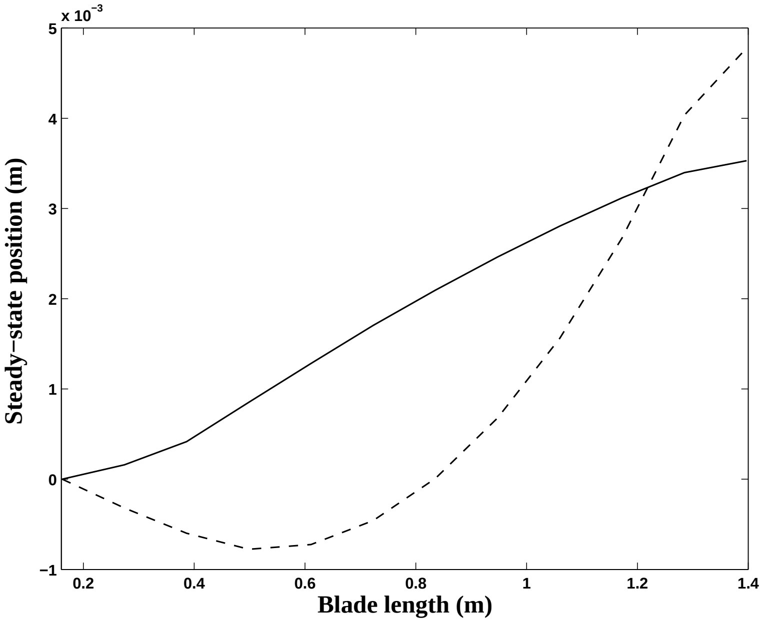

Figure 5.3: The steady-state equilibrium position of the ATR blade model. ‘——’, the axial elongation u_{A1}; ‘- - -’, the lead-lag displacement u_{A2}.

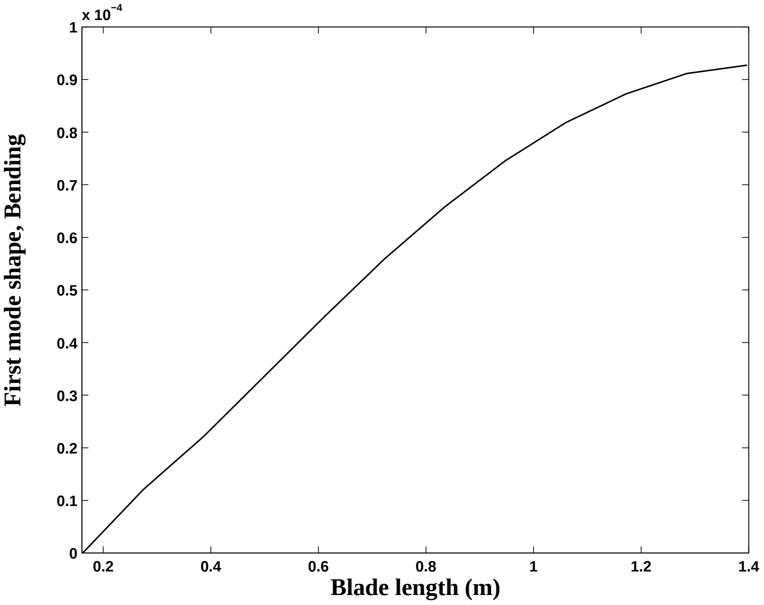

(a)

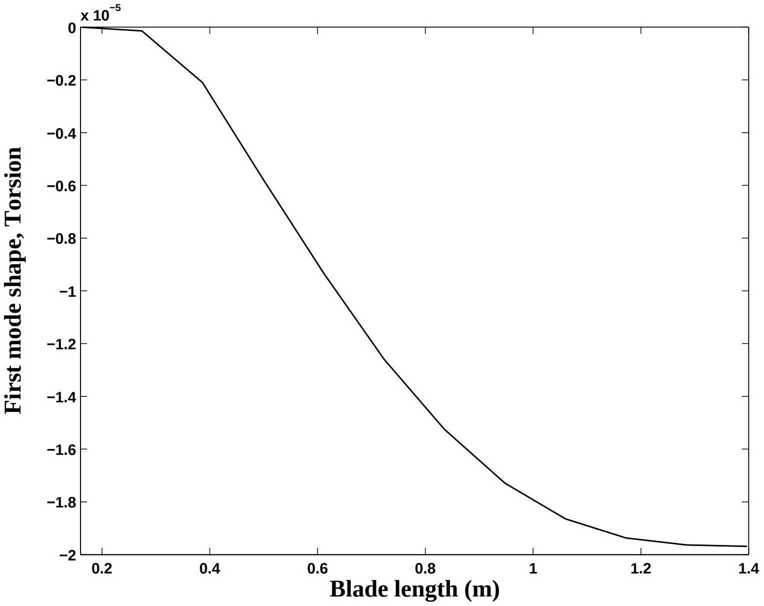

(b)

Figure 5.4: The first linear mode shape of the ATR blade model: (a) Bending deflection, (b) Torsion.

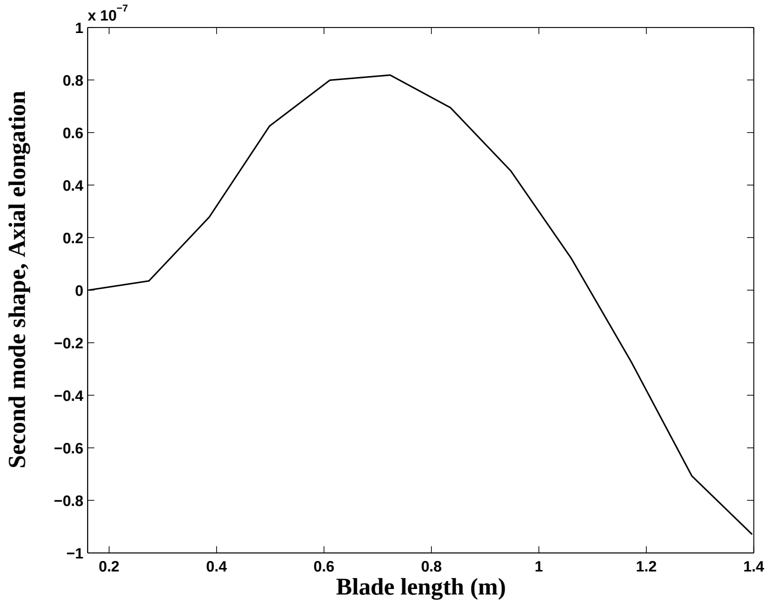

(a)

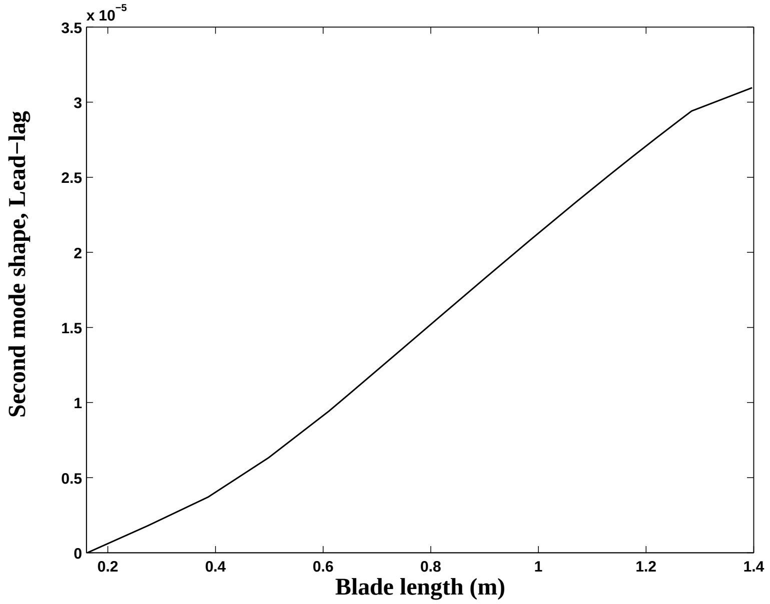

(b)

Figure 5.5: The second linear mode shape of the ATR blade model: (a) Axial elongation, (b) Lead-lag deflection.

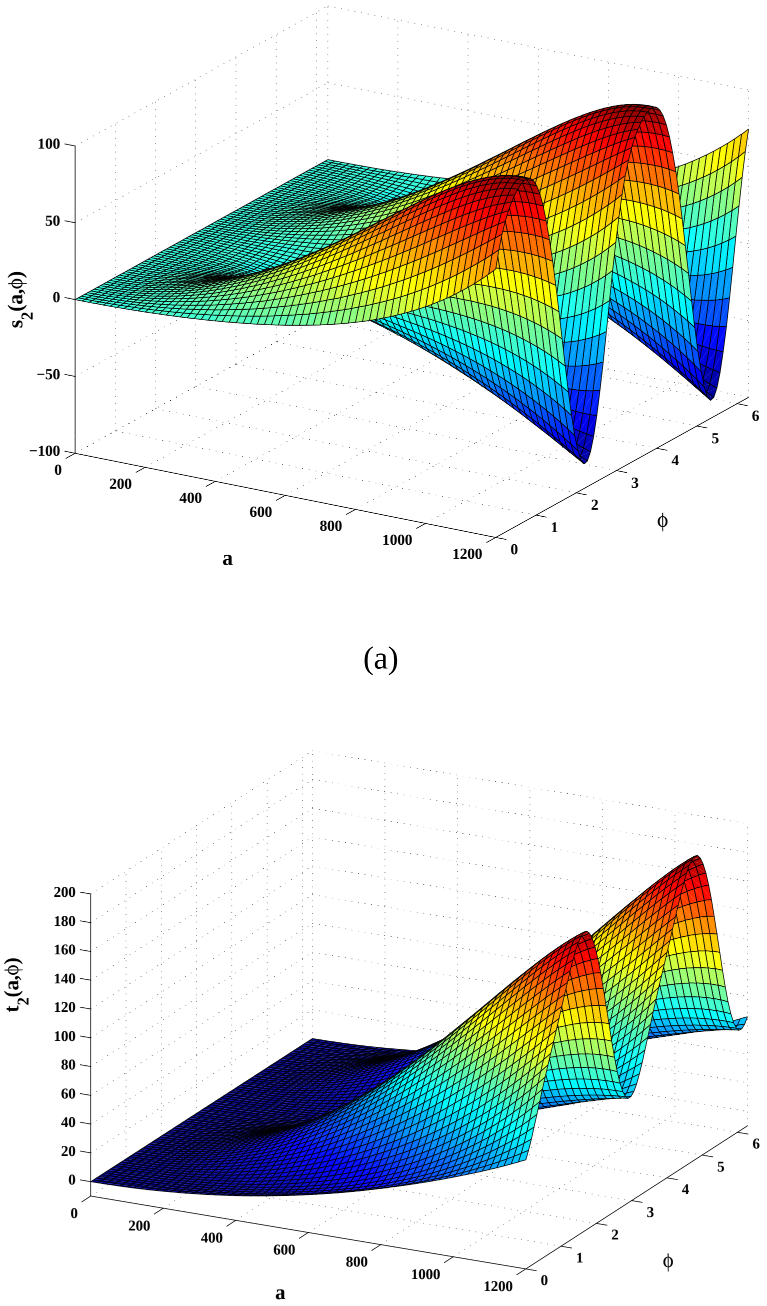

(a)

(b)

Figure 5.6: The invariant manifold for the first nonlinear normal mode — the slave constraint relationship of the second modal coordinate to the master coordinate: (a) $s_2(a, \phi)$, (b) $t_2(a, \phi)$.

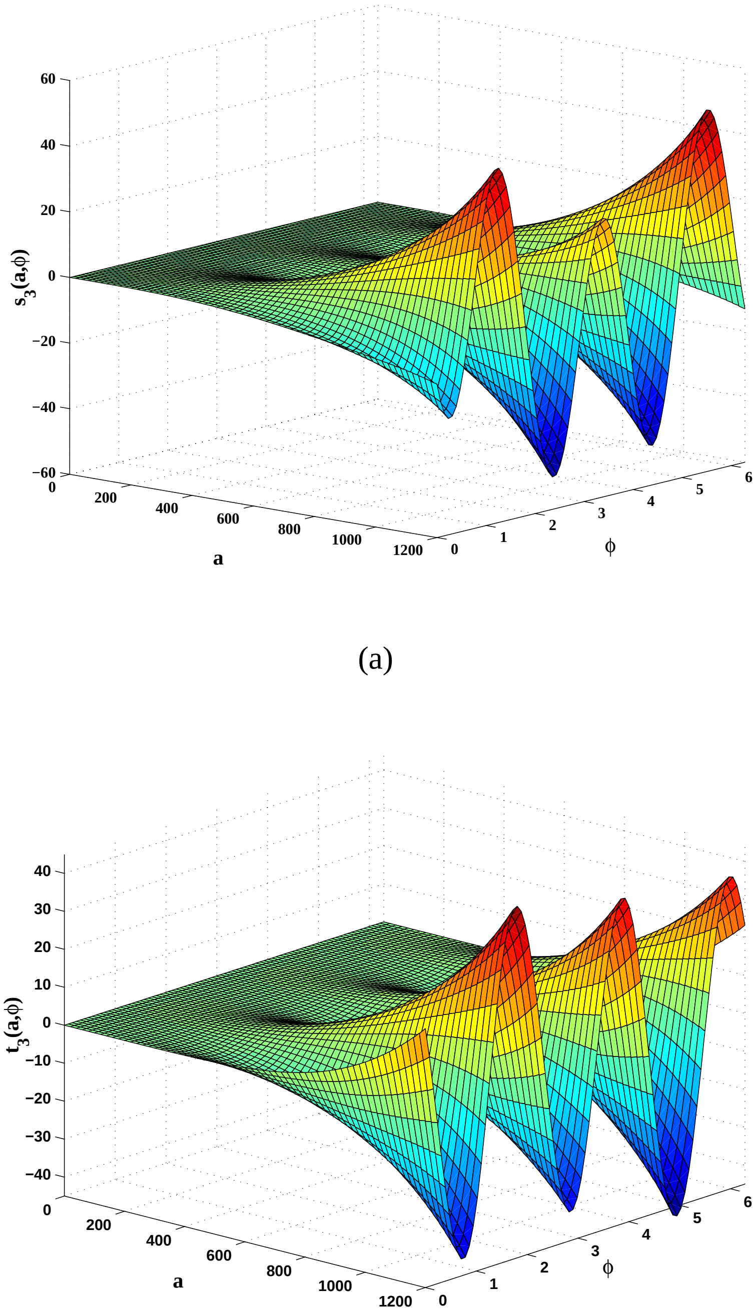

(a)

(b)

Figure 5.7: The invariant manifold for the first nonlinear normal mode — the slave constraint relationship of the third modal coordinate to the master coordinate: (a) $s_3(a, \phi)$, (b) $t_3(a, \phi)$.

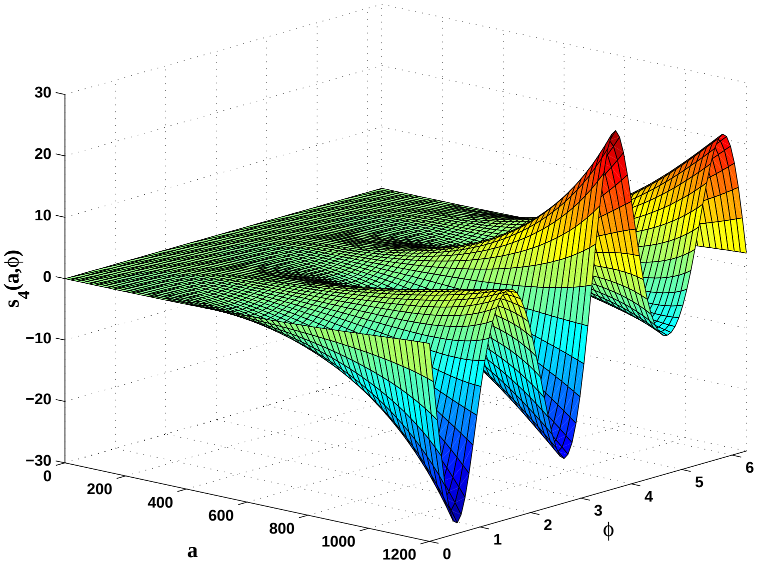

(a)

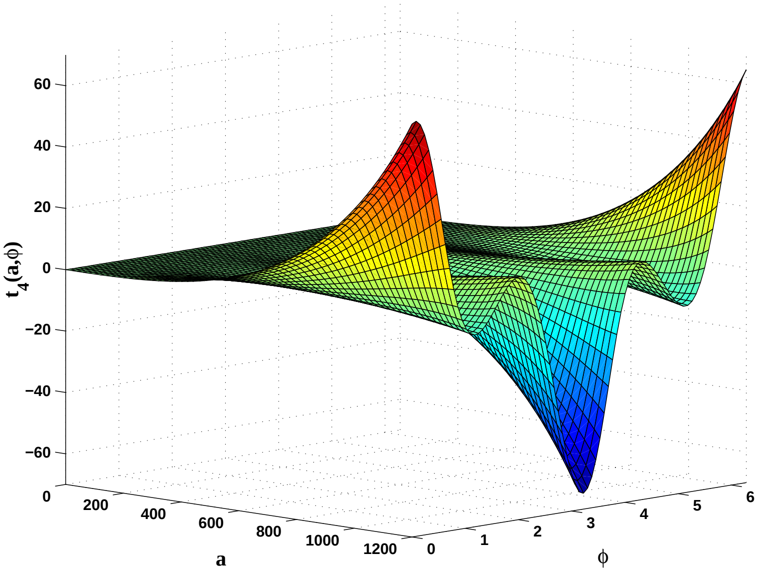

(b)

Figure 5.8: The invariant manifold for the first nonlinear normal mode — the slave constraint relationship of the fourth modal coordinate to the master coordinate: (a) $s_4(a,\phi)$, (b) $t_4(a,\phi)$.

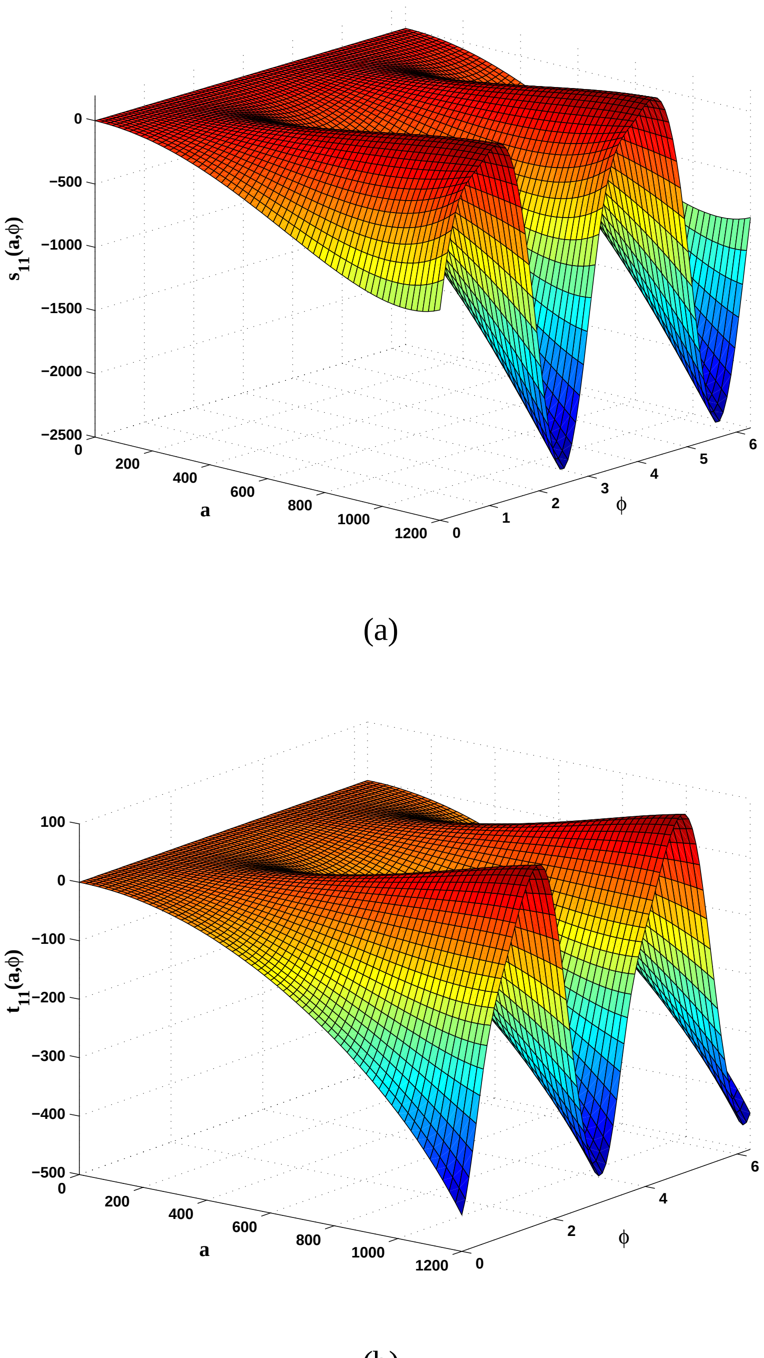

Figure 5.9: The invariant manifold for the first nonlinear normal mode — the slave constraint relationship of the 11th modal coordinate to the master coordinate: (a) $s_{11}(a, \phi)$, (b) $t_{11}(a, \phi)$.

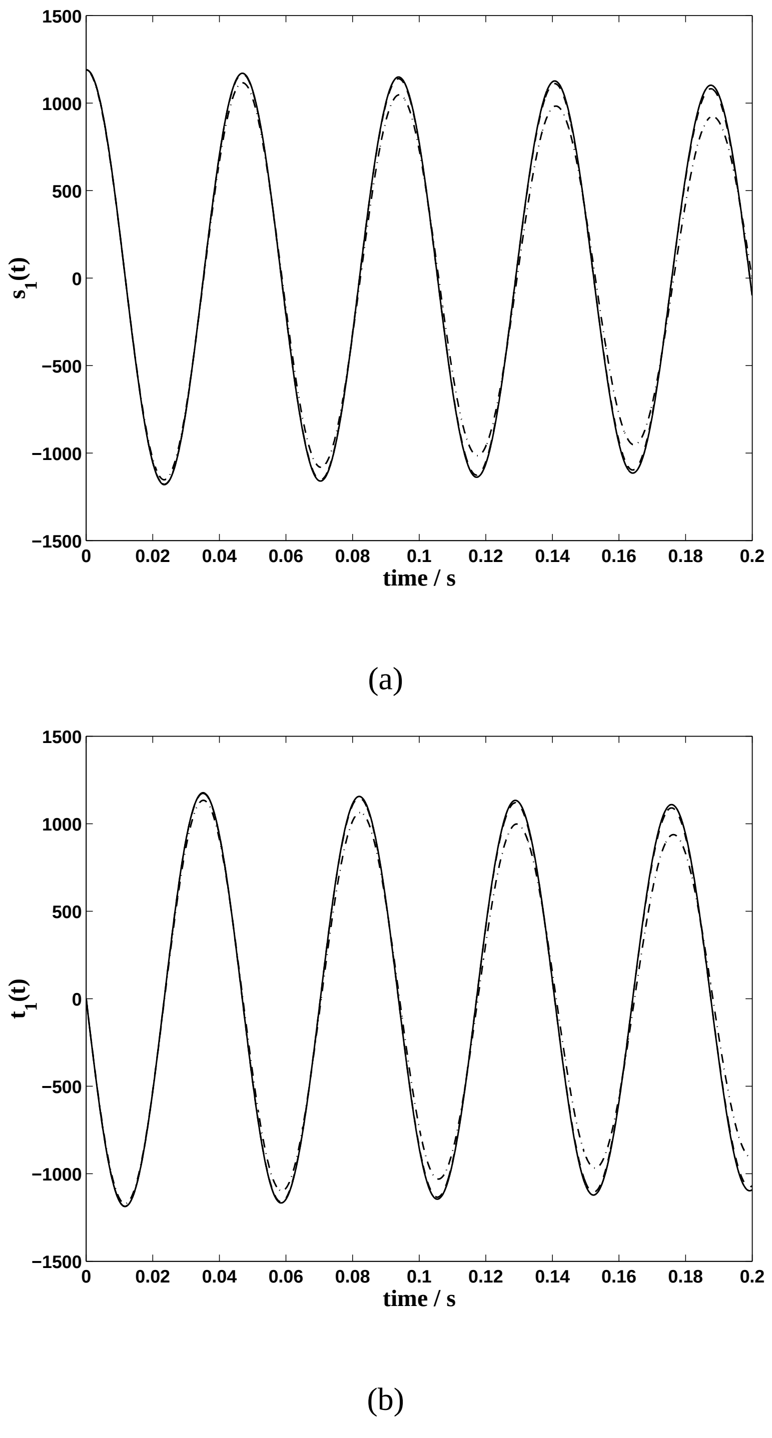

Figure 5.10: Time response on the invariant manifold of the first nonlinear normal mode – the master coordinate: (a) $s_1(t)$, (b) $t_1(t)$. '——', simulation based on the original 11-linear mode system; '- - -', simulation based on the nonlinear mode reduced-order model; '-··-··-·', one-linear mode simulation.

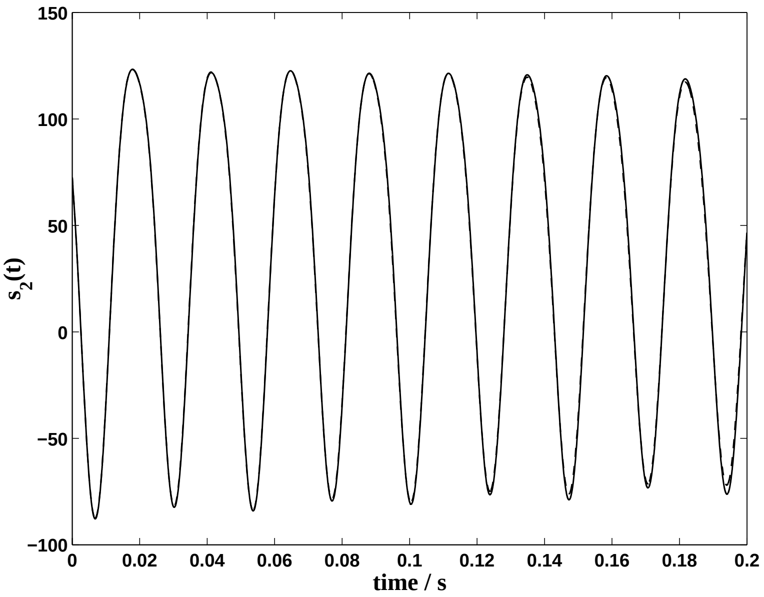

(a)

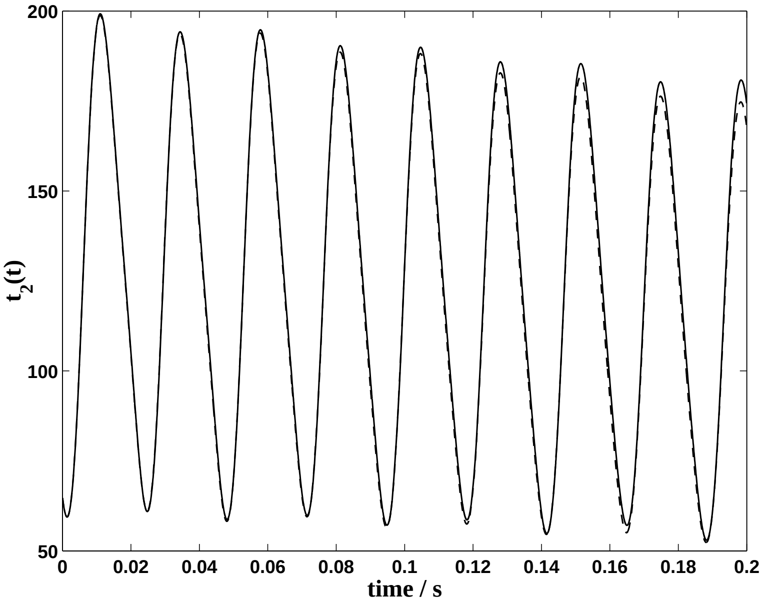

(b)

Figure 5.11: Time response on the invariant manifold of the first nonlinear normal mode – the slave coordinate corresponding to the first lead-lag mode: (a) $s_2(t)$, (b) $t_2(t)$. '——', simulation based on the original 11-linear mode system; '- - -', simulation based on the nonlinear mode reduced-order model.

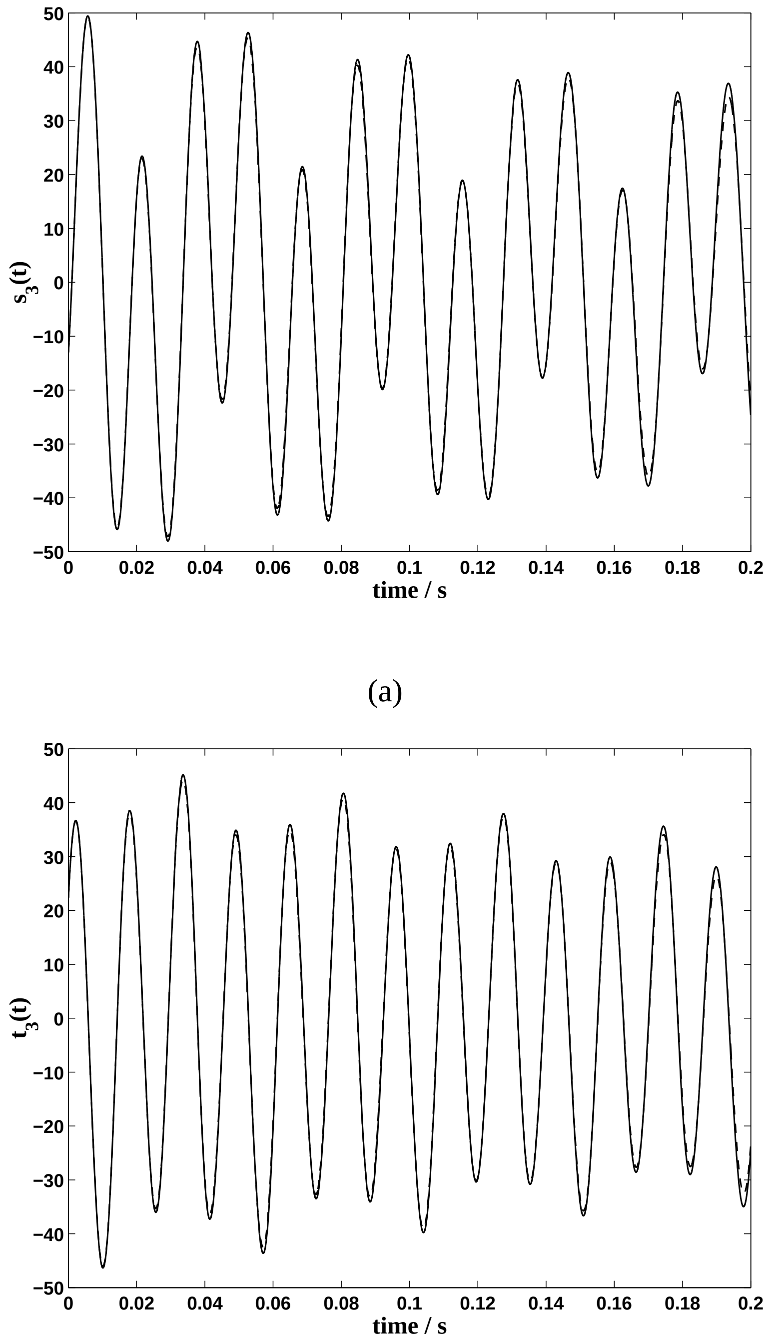

(a)

(b)

Figure 5.12: Time response on the invariant manifold of the first nonlinear normal mode – the slave coordinate corresponding to the second bending mode: (a) $s_3(t)$, (b) $t_3(t)$. '——', simulation based on the original 11-linear mode system; '- - -', simulation based on the nonlinear mode reduced-order model.

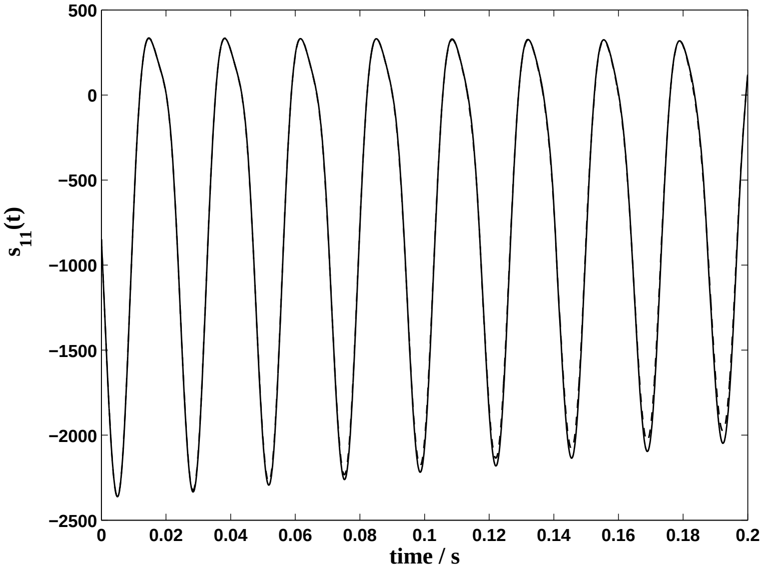

(a)

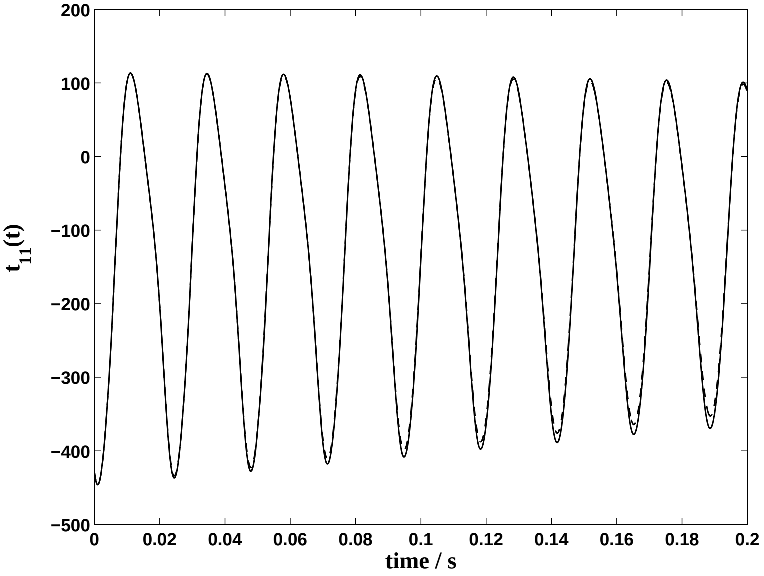

(b)

Figure 5.13: Time response on the invariant manifold of the first nonlinear normal mode – the slave coordinate corresponding to the first axial elongation mode: (a) $s_{11}(t)$, (b) $t_{11}(t)$. '——', simulation based on the original 11-linear mode system; '- - -', simulation based on the nonlinear mode reduced-order model.

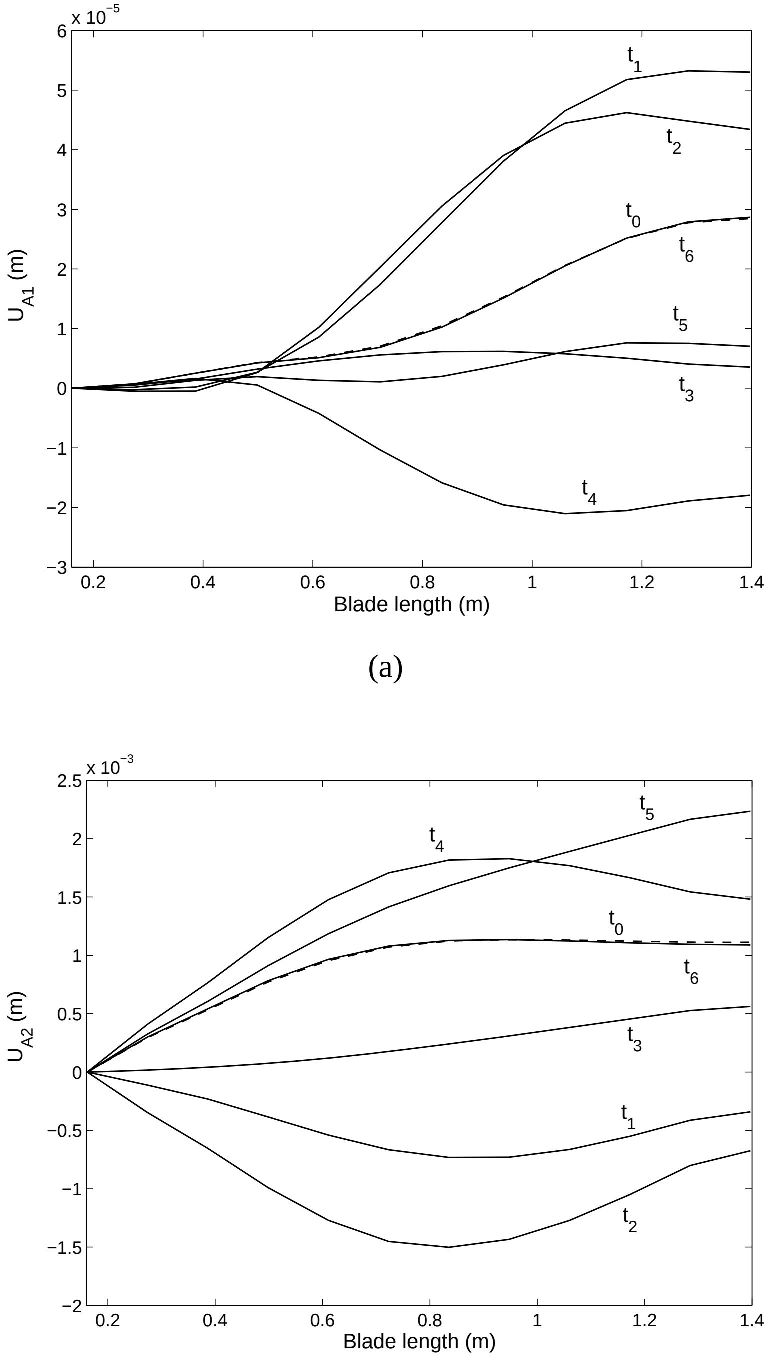

(a)

(b)

Figure 5.14: Time response on the invariant manifold of the first nonlinear normal mode – the physical displacements of the ATR blade: (a) Axial elongation u_{A1}, (b) Lead-lag motion u_{A2}. Initial time $t_0 = 0$; $t_1 = 0.0039\ s$; $t_2 = 0.0078\ s$; $t_3 = 0.0117\ s$; $t_4 = 0.0157\ s$; $t_5 = 0.0196\ s$; end time $t_6 = 0.0235\ s$, '- - - ', which is approximately one half period of the motion in the master coordinates (see figure 5.10).

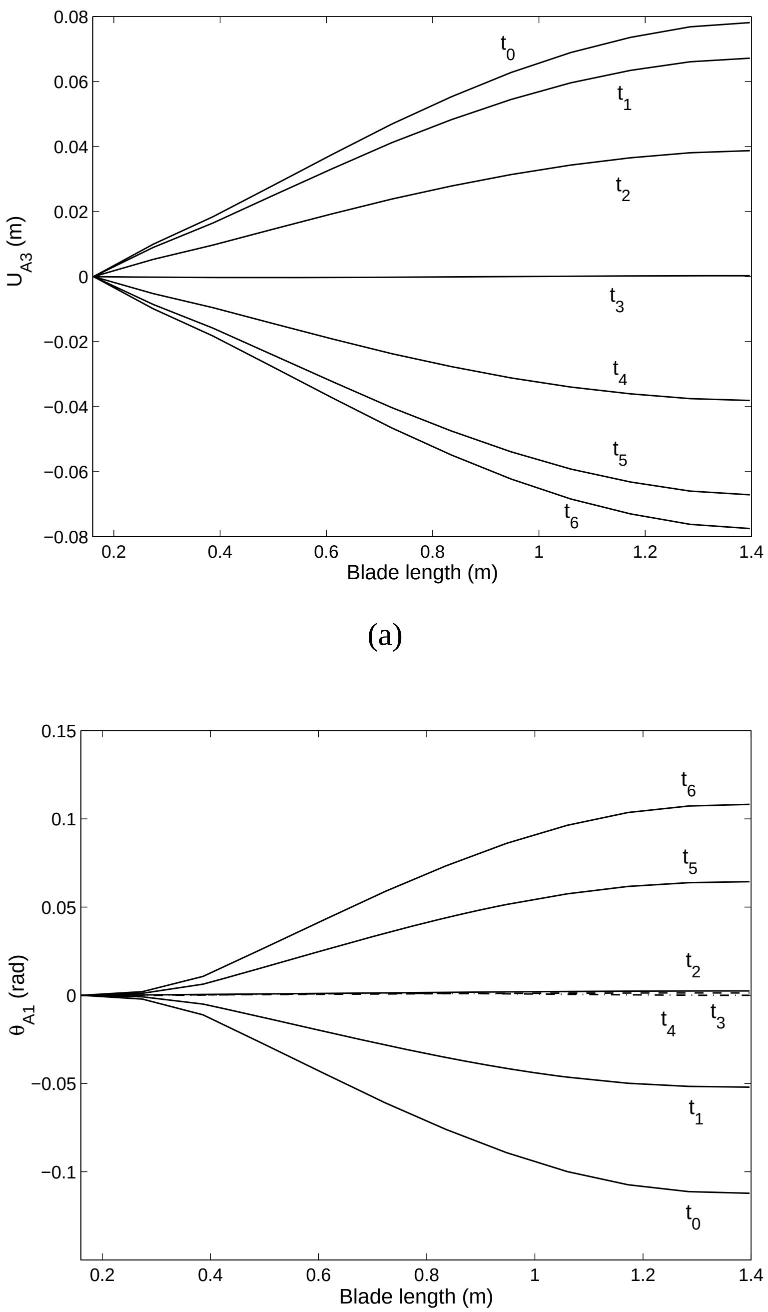

(a)

(b)

Figure 5.15: Time response on the invariant manifold of the first nonlinear normal mode – the physical displacements of the ATR blade: (a) Bending deflection u_{A3}, (b) torsion θ_{A1}. Initial time $t_0 = 0$; $t_1 = 0.0039\ s$; $t_2 = 0.0078\ s$; $t_3 = 0.0117\ s$, '- - - ' in Figure (b); $t_4 = 0.0157\ s$, '-··-··-·' in Figure (b); $t_5 = 0.0196\ s$; end time $t_6 = 0.0235\ s$, which is approximately one half period of the motion in the master coordinates (see figure 5.10).

CHAPTER VI

CONCLUSIONS

The essence of nonlinear modal analysis is to generate a minimal reduced order model that can capture the dynamics of the original system accurately. An effective normal-mode-based model order reduction methodology must satisfy two basic criteria. First, the method must be systematic, which means it can deal with various kinds of nonlinear forces and it can handle various structural models such as finite element models. Second, the construction of the nonlinear normal modes must be numerically efficient, in the sense that the solution can be obtained from a computer code in a reasonable time, regardless of the size of the actual nonlinear system. The results obtained in this dissertation demonstrate that the invariant-manifold-based approach is general enough to account for various types of nonlinear forces, such as non-smooth restoring forces, conventional quadratic and cubic nonlinear forces, and complex intrinsic nonlinear effects such as those in the model of a rotating rotorcraft blade. Also, the Galerkin-based solution technique developed has been shown to allow for the efficient generation of the invariant manifolds, for large nonlinear systems and up to large amplitudes. Therefore, this approach allows for the practical application of the invariant manifold formulation for a wide variety of engineering structures. As a result, the work presented in this dissertation has achieved significant advances for strongly nonlinear systems on two critical fronts — the *accuracy* of the reduced-order model and the *efficiency* of the attendant computations.

6.1 Contributions

The original contributions of this dissertation are described by re-examining the results obtained in the preceding chapters, as follows.

- In Chapter II, the Galerkin-based method for the construction of the invariant manifolds, originally developed for dynamic systems with smooth nonlinearities, has been extended to piecewise linear systems. The transformation of the master coordinates to polar form and the discretization in the amplitude domain make the Galerkin-based approach applicable in strongly nonlinear regions, as well as in the transition region between linear and nonlinear motions, with little additional analytical work. Previous to this work, no general method existed for the construction of nonlinear normal modes for systems with non-smooth restoring forces.

- In Chapter III, multi-nonlinear normal modes have been effectively generated by the invariant manifold approach. A systematic and efficient solution methodology for the invariant manifolds has been proposed, which uses the polar form of the master coordinates. Four-dimensional invariant manifolds have been successfully constructed for a rotating beam system, using a combination of finite difference or finite element discretization schemes in the amplitude domain and two-dimensional Fourier series expansions in the phase domain. This two-DOF reduced order model captures accurately the nonlinear internal resonance between two beam modes, which traditional nonlinear mode models derived using asymptotic methods are unable to describe.

- In Chapter IV, the invariant manifold approach has been generalized to nonlinear vibratory systems subjected to periodic excitation. One additional phase variable has been introduced to represent the external harmonic excitation. The reduced order model corresponding to the augmented invariant manifold has been shown to capture the forced dynamics of the original system accurately. Furthermore, this approach is general and can be extended to any type of excitation that can be modeled by a finite-state auxiliary dynamic system, including any type of external and/or parametric periodic excitation.

- In Chapter V, invariant-manifold-based nonlinear modal analysis has been applied to a complete nonlinear rotorcraft blade model. Contrary to the example systems studied in the preceding chapters, the rotating blade features complex, intrinsic nonlinearities. The invariant manifold approach has been successfully used for this complex system, producing an accurate single-DOF reduced order model that imbeds all significant physical blade motions. It is the first time that the nonlinear normal modes of a practical rotating blade model have been constructed.

6.2 Future research

Some thoughts for the future research in this field are discussed here.

- A stability analysis of the invariant manifolds for forced nonlinear systems would be of interest; this is related to the bifurcation work done by Rand [19–21], Vakakis [10, 25], etc. For autonomous systems, the invariant manifold approach can be considered as the direct extension of the center manifold theorem. For nonlinear systems with external excitation, the physical meaning of the invariant manifold needs to be justified by a thorough investigation of the nonlinear dynamics near the limit cycle with respect to the external excitation.

- The construction of multi-mode invariant manifolds is computationally expensive, and it represents a bottleneck for obtaining high-precision reduced order models efficiently. One difficulty is that the number of terms in the Fourier series expansions increases geometrically with the order ofthe manifold. This could possibly be overcome by using finite difference or finite element discretizations in the multi-dimensional phase domain.

- Systems with non-smooth restoring forces are another interesting topic of nonlinear modal analysis research. Composite materials are widely used in air vehicles, and in some cases the evaluation of their response can be difficult due to the asymmetry in material properties. For example, carbon-fiber reinforced materials feature different Young's modulus in traction and in compression. This means that the dynamic response of a structure made of carbon-fiber reinforced material cannot be obtained from linear vibration theory. Developing nonlinear reduced-order models for such advanced composite material would be valuable since their dynamics can be captured on the invariant manifolds.

- For the rotating ATR blade in Chapter V, structural damping, gravity, and aerodynamic coupling need to be included in the model, and the invariant manifold approach needs to be adjusted to account for these effects. This is deemed numerically feasible since the aerodynamic coupling can be expressed in terms of real numbers. It would also be of interest to embed the excitation from the smart material in the invariant manifold. Then, the resulting reduced order model could be utilized to carry out studies of active control.

BIBLIOGRAPHY

BIBLIOGRAPHY

[1] S. W. Shaw and C. Pierre. Non-linear normal modes and invariant manifolds. *Journal of Sound and Vibration*, 150:170–173, 1991.

[2] S. W. Shaw and C. Pierre. Normal modes for nonlinear vibratory systems. *Journal of Sound and Vibration*, 164:85–124, 1993.

[3] S. W. Shaw and C. Pierre. Normal modes of vibration for nonlinear continuous systems. *Journal of Sound and Vibration*, 169:319–347, 1994.

[4] S. W. Shaw. An invariant approach to nonlinear normal modes of vibration. *Journal of Nonlinear Science*, 4:419–448, 1994.

[5] N. Boivin. *Non-linear Modal Analysis of Structural Systems Using Invariant Manifolds*. Ph.D. Dissertation, The University of Michigan, Ann Arbor, MI., 1995.

[6] N. Boivin, C. Pierre, and S. W. Shaw. Non-linear normal modes, invariance, and modal dynamics approximations of non-linear systems. *Nonlinear Dynamics*, 8:315–346, 1995.

[7] E. Pesheck. *Reduced order modeling of nonlinear structural systems using nonlinear normal modes and invariant manifolds*. PhD thesis, The University of Michigan, Ann Arbor, MI., 2000.

[8] C. Atkinson and B. Taskett. A study of the nonlinearly related modal solutions of coupled nonlinear systems by superposition techniques. *ASME Journal of Applied Mechanics*, 32:359–364, 1965.

[9] R. Rand. Nonlinear normal mode in 2 degrees of freedom systems. *ASME Journal of Applied Mechanics*, 38:561, 1971.

[10] T. K. Caughey and A. F. Vakakis. A method of examining steady state solutions of forced discrete systems with strong nonlinearities. *International Journal of Non-Linear Mechanics*, 26:89–103, 1991.

[11] L. Jezequel and C. H. Lamarque. Analysis of non-linear dynamical systems by the normal form theory. *Journal of Sound and Vibration*, 149(3):429–459, 1991.

[12] A. H. Nayfeh, J. F. Nayfeh, and D. T. Mook. On methods for continuous systems with quadratic and cubic nonlinearities. *Nonlinear Dynamics*, 3:145–162, 1992.

[13] J. Aubrecht and A. F. Vakakis. Localized and non-localized nonlinear normal modes in a multi-span beam with geometric nonlinearities. *Journal of Vibration and Acoustics, Transactions of the ASME*, 118(4):533–541, 1996.

[14] M. Chati, R. Rand, and S. Mukherjee. Modal analysis of a cracked beam. *Journal of Sound and Vibration*, 207:249–270, 1997.

[15] G. Chakraborty, A. K. Mallik, and H. Hatwal. Normal modes and near-resonance response of beams with non-linear effects. *Journal of Sound and Vibration*, 210(1):19–36, 1998.

[16] R. M. Rosenberg. On nonlinear vibrations of systems with many degrees of freedom. *Advances in Applied Mechanics,* 9:155–242, 1966.

[17] C. Cooke and R. Struble. The existence of periodic solutions and normal mode vibrations in nonlinear systems. *Quarterly of Applied Mathematics*, 24:177–193, 1966.

[18] C. Pak and R. Rosenberg. On the existence of normal mode vibrations in nonlinear systems. *Quarterly of Applied Mathematics*, 26:403–416, 1968.

[19] R. Rand. The geometrical stability of nonlinear normal modes in 2 degrees of freedom systems. *International Journal of Non-Linear Mechanics*, 8:161–168, 1973.

[20] L. A. Month and R. H. Rand. An application of poincaré map to the stability of nonlinear normal modes. *ASME Journal of Applied Mechanics*, 47:645–651, 1980.

[21] C. Pak, R. Rand, and A. Vakakis. Bifurcaion of nonlinear normal modes in a class of 2 degrees of freedom systems. *Acta Mechanica*, 3:129–145, 1992.

[22] H. Greenberg and T. L. Yang. Modal subspaces and normal mode vibrations. *International Journal of Non-Linear Mechanics*, 6:311–326, 1971.

[23] R. Rand. A direct method for nonlinear normal modes. *International Journal of Non-Linear Mechanics*, 9:363–368, 1974.

[24] A. F. Vakakis, L. I. Manevitch, Y. V. Mikhlin, V. N. Pilipchuk, and A. A. Zevin. *Normal modes and localization in nonlinear systems*. New York: John Wiley, 1996.

[25] A. F. Vakakis. Non-linear normal modes and their applications in vibration theory: an overview. *Mechanical Systems and Signal Processing*, 11:3–22, 1997.

[26] M. E. King and A. F. Vakakis. An energy-based formulation for computing nonlinear normal modes in undamped continuous systems. *ASME Journal of Vibration and Acoustics*, 116:332–340, 1994.

[27] M. E. King and A. F. Vakakis. An energy-based approach to computing resonant nonlinear normal modes. *ASME Journal of Applied Mechanics*, 63:810–819, 1996.

[28] A. H. Nayfeh and S. A. Nayfeh. On nonlinear modes of continuous systems. *ASME Journal of Vibration and Acoustics*, 116:129–136, 1994.

[29] A. H. Nayfeh, C. Chin, and S. A. Nayfeh. On nonlinear normal modes of systems with internal resonance. *ASME Journal of Vibrations and Acoustics*, 118:340–345, 1996.

[30] E. Pesheck, C. Pierre, and S. W. Shaw. Accurate reduced-order models for a simple rotor blade model using nonlinear normal modes. *Mathematical and Computer Modelling*, 33:1085–1097, 2001.

[31] A. J. Roberts. The invariant manifold of beam deformations. *Journal of Elasticity*, 30:1–54, 1993.

[32] I. T. Georgiou and I. B. Schwartz. Slaving the in-plane motions of a nonlinear plate to its flexural motions: An invariant manifold approach. *Journal of Applied Mechanics, Transactions of the ASME*, 64:175–182, 1997.

[33] I. T. Georgiou, A. K. Bajaj, and M. Corless. Slow and fast invariant manifolds, and normal modes in a two degree-of freedom structural dynamical system with multiple equilibrium states. *International Journal of Non-linear Mechanics*, 33(2):275–300, 1998.

[34] A. H. Nayfeh, W. Lacarbonara, and C. Chin. Nonlinear normal modes of buckled beams: three-to-one and one-to-one internal resonances. *Nonlinear Dynamics*, 18:253–273, 1999.

[35] T. B. Burton and M. N. Hamdan. On the calculation of non-linear normal modes in continuous systems. *Journal of Sound and Vibration*, 197(1):117–130, 1996.

[36] A. Y. T. Leung and T. Ge. Normal multi-modes of non-linear euler beams. *Journal of Sound and Vibration*, 202(2):145–160, 1997.

[37] S. Chen and S. W. Shaw. Normal modes for piecewise linear vibratory systems. *Nonlinear Dynamics*, 10:135–163, 1996.

[38] J. C. Slater. A numerical method for determining nonlinear normal modes. *Nonlinear Dynamics*, 10:19–30, 1996.

[39] J. C. Slater and D. J. Inman. On the effect of weak non-linearities on linear controllability and observability norms, an invariant manifold approach. *Journal of Sound and Vibration*, 199(3):417–429, 1997.

[40] R. M. Rosenberg. The normal modes of nonlinear n-degree-of-freedom systems. *ASME Journal of Applied Mechanics*, 30:7–14, 1962.

[41] R. M. Rosenberg and J. K. Kuo. Nonsimilar normal mode vibrations of nonlinear systems having two degrees of freedom. *ASME Journal of Applied Mechanics*, 31:283–290, 1964.

[42] E. Pesheck, C. Pierre, and S. W. Shaw. A new galerkin-based approach for accurate non-linear normal modes through invariant manifolds. *Journal of Sound and Vibration*, 249:971–993, 2002.

[43] Y. S. Choi and S. T. Noah. Forced periodic vibration of unsymmetric piecewise-linear systems. *Journal of Sound and Vibration*, 121:117–126, 1988.

[44] R. J. Comparin and R. Singh. Non-linear frequency response characteristics of an impact pair. *Journal of Sound and Vibration*, 134:259–290, 1989.

[45] R. J. Comparin and R. Singh. Frequency response characteristics of a multi-degree-of-freedom system with clearances. *Journal of Sound and Vibration*, 142:101–124, 1990.

[46] S. W. Shaw and P. J. Holmes. A periodically forced piecewise linear oscillator. *Journal of Sound and Vibration*, 90:129–155, 1983.

[47] J. M. T. Thompson and H. B. Stewart. *Nonlinear Dynamics and Chaos*. Chichester: John Wiley, 1986.

[48] I. A. Mahfouz and F. Badrakhan. Chaotic behavior of some piecewise linear systems, part i: systems with set-up spring or with unsymmetric elasticity. *Journal of Sound and Vibration*, 143:255–288, 1990.

[49] L. Zuo and A. Curnier. Non-linear real and complex modes of conewise linear systems. *Journal of Sound and Vibration*, 174:289–313, 1994.

[50] A. P. Ivanov. The stability of periodic solutions of discontinuity systems that intersect several surfaces of discontinuity. *J. Appl. Maths Mechs*, 62:677–685, 1998.

[51] R. Seydel. *From equilibrium to chaos - practical bifurcation and stability analysis*. New York: Elsevier Science, 1988.

[52] M. A. Aizerman and F. R. Gantmakher. Stability in the linear approximation of a periodic solution of a system of differential equations with discontinuous right-hand sides. *Prikl. Mat. Mekh.*, 21:658–669, 1957.

[53] J. Guckenheimer and P. Holmes. *Nonlinear Oscillations, Dynamical Systems and Bifurcations of Vector Fields, Applied Mathematical Sciences 42*. New York: Springer-Verlag, 1989.

[54] D. Jiang, C. Pierre, and S. W. Shaw. Large-amplitude nonlinear normal modes of piecewise linear systems. *Journal of Sound and Vibration*, In Press, 2004.

[55] M. Legrand, D. Jiang, C. Pierre, and S. W. Shaw. Nonlinear normal modes of a rotating shaft based on the invariant manifold method. In *Ninth International Symposium on Transport Phenomena and Dynamics of Rotating Machinery (ISROMAC-9)*, Honolulu, Hawaii, February 10–14 2002.

[56] E. Pesheck, C. Pierre, and S. W. Shaw. Model reduction of a nonlinear rotating beam through nonlinear normal modes. *ASME Journal of Vibration and Acoustics*, 124(2):229–236, 2002.

[57] M. J. D. Powell. *Numerical methods for nonlinear algebraic equations*. London: Gordon and Breach Science Publisher, 1970.

[58] P. Apiwattanalunggarn, S. W. Shaw, C. Pierre, and D. Jiang. Finite-element-based nonlinear modal reduction of a rotating beam with large-amplitude motion. *Journal of Vibration and Control*, 9(3), 2003.

[59] S. W. Shaw, C. Pierre, and E. Pesheck. Modal analysis-based reduced-order models for nonlinear structures – an invariant manifold approach. *The Shock and Vibration Digest*, 31:3–16, 1999.

[60] G. S. Agnes and D. J. Inman. Performance of nonlinear vibration absorbers for multi-degrees-of-freedom systems using nonlinear normal modes. *Nonlinear Dynamics*, 25:275–292, 2001.

[61] D. Jiang, C. Pierre, and S. W. Shaw. The construction of nonlinear normal modes for systems with internal resonance: application to rotating beams. In *Proceedings of 2002 ASME International Mechanical Engineering Congress, ASME Paper IMECE02-32412*, New Orleans, Louisianan, November 17–22 2002.

[62] P. Sundararajan and S. T. Noah. An algorithm for response and stability of large order non-linear systems — application to rotor systems. *Journal of Sound and Vibration*, 214:695–723, 1998.

[63] P. P. Friedmann and D. H. Hodges. *Fight-vehicle materials, structures, and dynamics: structural dynamics and aeroelasticity (edited by A. K. Noor and S. L. Venneri)*. New York: ASME press, 1993.

[64] D. H. Hodges. A mixed variational formulation based on exact intrinsic equations for dynamics of moving beams. *International Journal of Solids and Structures*, 26(11):1253–1273, 1990.

[65] D. H. Hodges, X. Shang, and C. E. S. Cesnik. Finite element solution of nonlinear intrinsic equations for curved composite beams. *Journal of the American helicopter society*, 41:313–321, 1996.

[66] C. E. S. Cesnik, S. Shin, and M. L. Wilbur. Dynamic response of active twist rotor blade. *Smart materials and structures*, 10:62–76, 2001.

[67] C. E. S. Cesnik and D. H. Hodges. Vabs: a new concept for composite rotor blade cross-section modeling. *Journal of the American helicopter society*, 42:27–38, 1997.

[68] M. Hirsch and S. Smale. *Differential equations, dynamical systems and linear algebra*. New York: Academic press, 1974.

ABSTRACT

NONLINEAR MODAL ANALYSIS BASED ON INVARIANT MANIFOLDS — APPLICATION TO ROTATING BLADE SYSTEMS

by

Dongying Jiang

Co-Chairs: Christophe Pierre, Steven W. Shaw

This research aims at the development and implementation of new model reduction methods for nonlinear structural systems, based on a nonlinear modal analysis methodology. Invariant manifolds in the system's phase space are used to define and construct nonlinear normal modes of motion for a wide class of nonlinear vibratory systems. A numerical Galerkin technique is utilized to solve for the invariant manifolds, which allows one to construct nonlinear normal modes and carry out nonlinear mode-based model reduction for motions in strongly nonlinear regions of the phase space. This method seamlessly interfaces with finite element models of engineering structures, and it allows the user to specify the vibration amplitude range and the accuracy of the model over that range. In this dissertation, the nonlinear modal analysis methodology is generalized to multi-nonlinear normal mode systems, including those with internal resonances. The approach is also successfully extended to systems with piecewise linear restoring forces, which model struc-

tural components with clearance, pre-load, or different elastic materials. Furthermore, nonlinear modal analysis is developed for systems that are subjected to periodic forces, thereby providing a useful tool for attacking the important problem of obtaining the frequency response of complex nonlinear structures. Finally, the invariant-manifold-based model reduction methodology is applied to a complex engineering structure, namely the model for a prototype of an active twist rotor blade. Rotorcraft blades feature significant nonlinear behavior, due to rotation, large deformation, and complex blade geometries and materials. While discretized blade models typically feature large numbers of degrees of freedom, the proposed approach is shown to yield an efficient reduced order model.